

Spatiotemporal Variations Of Saturn's Zonal Winds Based On
Cassini Long-term (2004-2017) Multi-Instrument Observations

by
Aaron Mark Studwell

A dissertation submitted to the Department of Earth & Atmospheric Sciences,
College of Natural Sciences and Mathematics
in partial fulfillment of the requirements for the degree of

DOCTOR OF PHILOSOPHY

in Atmospheric Sciences

Chair of Committee: Liming Li

Co-Chair of Committee: Xun Jiang

Committee Member: Yunsoo Choi

Committee Member: Yuxuan Wang

Committee Member: Lowell Wood

University of Houston

May 2020

ACKNOWLEDGEMENTS

I would like to acknowledge and greatly thank Dr. Xun Jiang and Dr. Liming Li for their patience, support, and faith in me through my studies and research in the Department of Earth and Atmospheric Sciences. Their experience and guidance in helping with all facets of the doctoral work – my research, writing, and navigating the doctoral process – was invaluable. Additionally, I must recognize the contributions that my committee has been made to me during my time at the University of Houston – Dr. Yunsoo Choi, Dr. Yuxuan Wang, Dr. Lowell Wood and the late Dr. Robert Talbot. All of you have been so supportive of my research and academic endeavors – I cannot ever begin to repay for you for believing in me, even during my hard times.

In actuality, my academic journey into the sciences really starts and ends with the love and support of my parents, my dad, the late Allan Studwell and my mom, Dorothea Studwell. My son, Alexander, has also given amazing support, as he pursues his own engineering degree.

This research could not have been completed without the coordination and support of the Imaging Science Subsystem groups at both the NASA-Goddard Space Flight Center and at Oxford University. Additional acknowledgements to Patrick Frye of the University of Wisconsin for conducting the initial processing of the Cassini data from the

Visible and Infrared Mapping Spectrometer. The NASA ROSES Cassini Data Analysis Program and the Planetary Data Archiving, Restoration, and Tools programs are also acknowledged for their support of this research, along with both of the Cassini VIMS and ISS teams.

Many thanks to the one person in my life who has never given up on me – Katherine Meehan. Every day, your guidance and who are you in my life are both needed and cherished.

The academic portion of my doctoral work literally could not have been completed without the support, understanding, and encouragement of my former co-workers and always friends at Wilkens Weather. Finally, thanks to the faculty and students of the Department of Meteorology at Eötvös Loránd University in Budapest, Hungary, particularly Dr. Mészáros and Dr. Pieczka. My time at Eötvös Loránd gave me the drive to finish this journey.

ABSTRACT

The observations of Saturn by the Cassini mission spanned thirteen years (2004-2017) and provided scientists data and images that will expand our knowledge for decades to come. This dissertation is divided into four tasks: 1) Develop and validate a more general form of thermal wind equation (TWE), which does not apply the assumptions used in the classical TWE; 2) Apply the new TWE to study the spatiotemporal patterns of the atmospheric winds above the visible cloud layer, ~ 1 to 500 mbar; 3) Develop a global profile of the atmospheric winds below the visible cloud layer, $\sim 1,000$ to 3,000 mbar; and 4) Utilize atmospheric winds to investigate Saturn's 2010 Great White Storm with particular attention to its asymmetric development.

The results from Tasks 1, 2 and 3 provides a relatively complete picture of the seasonal variations of Saturn's winds. Some important characteristics of Saturn's winds are revealed: (1) The global profile of zonal winds in the deep troposphere is generated for the first time; (2) In the polar region, the 2,000-mbar winds undergo temporal variation; (3) Within the visible cloud layer, the zonal winds did not significantly change between 2009 and 2015; and (4) The stratospheric equatorial zonal jets weakened from $\sim 500 \text{ m s}^{-1}$ in 2009 to 0 m s^{-1} in 2015. This is the first systematic analysis of the seasonal changes of Saturn's zonal winds across both the troposphere and stratosphere, expanding our

understanding of spatiotemporal variations of Saturn's atmosphere. In particular, the vertical structure and its changes over time yield new insight on the atmospheric dynamics (e.g., stability), which in turn aid in the development of new theories and models of the atmospheric systems of the giant planets.

In Task 4, the wind field and the associated vorticity field are used to investigate 2010 Great White Storm. Specifically, during the mature phase of this event, the associated bright clouds expanded significantly equatorward, but its poleward growth was limited. The analysis of the wind and vorticity fields suggest that large meridional gradients of quasi-geostrophic potential vorticity, acting as a barrier to cloud mixing, was a factor in the asymmetric expansion.

TABLE OF CONTENTS

ACKNOWLEDGEMENTS.....	ii
ABSTRACT	iv
LIST OF TABLES.....	ix
LIST OF FIGURES.....	x
Chapter 1: Introduction.....	1
1.1 Motivation.....	5
1.2 Dissertation Overview.....	6
Chapter 2: Atmospheric Structure of Saturn.....	9
2.1 Atmospheric Profile of Saturn.....	10
2.2. Uncertainty of Saturn’s Rotation Period.....	13
Chapter 3 (Task 1): Thermal Wind Equation	16
3.1. Previous Research.....	18
3.2. Forms of the Thermal Wind Equation	22
3.2.1. Standard Form of the Thermal Wind Equation.....	23
3.2.2. General Form of the Thermal Wind Equation.....	25
3.2.2.1 Derivation of the General Thermal Wind Equation.....	26
3.2.2.2. Physical Interpretation of the General Thermal Wind Equation	29
3.3. Comparison of the Thermal Wind Equations.....	33
3.4. Validation and Application of the Thermal Wind Equation	37

3.5. Conclusions.....	47
Chapter 4 (Task 2): Spatiotemporal Variations of Saturn’s Zonal Winds at & above the visible cloud level.....	49
4.1. Data and Processing Methodology – ISS Output.....	50
4.1.1. Data – ISS Images.....	51
4.1.2. Processing Methodology – ISS Images	54
4.1.2.1. Data Processing.....	54
4.1.2.2. Navigation and Fitting.....	56
4.1.2.3. Estimations and Errors of Zonal Winds	57
4.2. Previous Research – ISS	61
4.3. ISS Analysis: Zonal Winds at & above the Visible Cloud Level.....	73
4.4. Data and Processing Methodology – CIRS Output	76
4.4.1. Data – CIRS Radiance Measurements.....	79
4.4.2. Processing Methodology – CIRS Output.....	81
4.4.2.1. Data Processing.....	81
4.4.2.2. Estimations and Errors of Zonal Winds	83
4.5. Previous Research – CIRS.....	85
4.6. CIRS Analysis: Zonal Winds at & above the Visible Cloud Level.....	94
4.7. Conclusions.....	104

Chapter 5 (Task 3): Spatiotemporal Variations of Saturn’s Zonal Winds below the visible cloud level	108
5.1. Data and Processing Methodology – VIMS Output	109
5.1.1. Data – VIMS 5- μ m Images	109
5.1.2. Processing Methodology – VIMS 5- μ m Images	114
5.1.2.1. Data Processing	114
5.1.2.2. Navigation and Fitting	116
5.1.2.3. Estimations and Errors of Zonal Winds	117
5.2. Previous Research – VIMS	122
5.3. VIMS Analysis: Saturn’s zonal winds below the visible cloud level	127
5.4. Conclusions	142
Chapter 6 (Task 4): Analysis of Saturn’s Great White Storm of 2010	145
6.1. Previous Research – Great White Storms	148
6.2. Asymmetric Expansion in 2010 Great White Storm	170
6.2.1. Methodology – Asymmetric Expansion in 2010 GWS	172
6.2.2. Results – Asymmetric Expansion in 2010 GWS	177
6.3. Conclusions	182
Chapter 7. Conclusions	184
BIBLIOGRAPHY	189

LIST OF TABLES

4.1. Data collected through these ISS filters was used to track clouds and establish the associated zonal wind speed through the upper troposphere.....	52
4.2. Data collected through these CIRS focal planes was used to determine temperatures through the upper atmospheres and the associated thermal winds.....	80

LIST OF FIGURES

2.1. Cross-section of Saturn's atmosphere.....	11
3.1. Zonal-mean CIRS temperatures and the derived thermal winds.....	20
3.2. Schematic of the cylindrical routine for the general thermal wind equation.	34
3.3. Comparison between the observed and geostrophic zonal winds, calculated from the geopotential height field.	40
3.4. Comparison between the observed and derived zonal winds, using the standard form of the TWE.....	42
3.5. Comparison between the observed and derived zonal winds, using the general form of the TWE.....	43
3.6. Comparison between the standard and general forms of the TWE for the equatorial region.	44
3.7. Comparison between the observed and derived temperature, based on the inverse application of the standard form of the TWE.	46
4.1. Schematic illustrating the location of the narrow- and wide-angle cameras on the ISS.	51
4.2. Cross-section of Saturn's atmosphere, noted with pressure levels observed by the CIRS and ISS.	53
4.3. Zonal wind velocity and associated atmospheric parameters observed in vicinity of the hexagon polar jet from 2008-2009 and 2012 using Cassini ISS images.....	70
4.4. Comparison of the SH equatorial winds using the ISS MT3 and CB3 filters between 2004-2005 and 2008.	75
4.5. Comparison of the NH equatorial winds using the ISS CB3 filter between 2009 and 2015.....	76
4.6. CIRS conceptual layout.....	77

4.7. Cassini CIRS high spatial resolution zonal-mean temperatures across Saturn’s upper atmosphere in latitude-altitude cross section; Data processed by the GSFC Cassini CIRS group.....	97
4.8. Comparison of the thermal winds through Saturn’s upper atmosphere, derived through the standard and general forms of the TWE.....	98
4.9. Graphic representation of different integration routines used in standard and general forms of the TWE.	100
4.10. Comparison of the thermal winds of Saturn’s upper atmosphere, based under two independently-derived temperature profiles.	101
4.11. Comparison of atmospheric temperature profiles, ranging from 70°S to 70°N...103	
4.12. Comparison of the NH stratospheric equatorial jet (~0.1 mbar) between 2009 and 2015.....	104
5.1. VIMS conceptual layout.....	110
5.2. Cross-section of Saturn’s atmosphere, noted with pressure levels observed by the CIRS, ISS and VIMS.	111
5.3. Comparison of global zonal wind data, derived from both VIMS and ISS data, for two different rotational period estimates.....	122
5.4. Examples of 5- μ m VIMS cloud imagery.....	130
5.5. Global zonal wind data derived from both VIMS and ISS data.	132
5.6. Curvature, U_{yy} , of the zonal wind profiles, compared to β	134
5.7. Atmospheric parameters calculated from ISS and VIMS winds, primarily from 2015 through 2017.	137
5.8. Comparison of the VIMS 5- μ m zonal winds across Saturn’s polar regions, ranging from 2008 through 2017.....	141

6.1. First known drawing of 1876 Great White Storm by D.W. Edgecomb, Connecticut, USA on December 10, 1876, 6:30 PM local time.	149
6.2. Mean wind velocity at the head of the 2010 GWS.	166
6.3. Hovmöller diagram of the 2010 Great White Storm from December 2010 through August 2011.	171
6.4. Cassini measurements of the Northern Hemisphere temperature field of Saturn in 2011.....	176
6.5. Cassini measurements of the Northern Hemisphere zonal wind field of Saturn in 2011.....	179
6.6. Zonal-mean meridional gradient of the quasi-geostrophic potential vorticity, \bar{Q}_y	180

Chapter 1: Introduction

Within our solar system, Saturn is a unique planet with a series of challenges in data acquisition. While there have been a number of exploratory missions through our solar system, the Cassini mission was one of the longest; orbital insertion at Saturn occurred on June 30, 2004, and its curtain call, a planned plunge into Saturn's atmosphere, was on September 15, 2017. On its final dive, Cassini had its high-gain antenna aimed at Earth, collecting and sending data until its fiery demise.

The original mission specifications scheduled Cassini to end in May 2008; however, two extensions in funding — one in 2008 and the other in 2010 — allowed for continued operations through May 2017. As noted previously, the Grand Finale of the mission eventually occurred in September 2017.

In total, the Cassini Prime Mission (2004-2008), the Cassini Equinox Mission (2008-2010), the Cassini Solstice Mission (2010-2017), and the Grand Finale (2017) lasted 4,826 days. With a Saturnian year lasting 10,759 days, this allowed the Cassini mission to acquire data for a little under half (45%) of a Kronian year.

While previous fly-by exploratory missions—Pioneer 11 (1979) and Voyager I (1980) and II (1981) — observed Saturn, Cassini stands alone in the scope and volume of data collected on the entirety of Saturn and its moons. With almost half of a Kronian year of data available, the temporal extent of the atmospheric data collected allows for the examination of seasonal patterns, along with other phenomena, such as the hexagonal storm in the polar extent of the Northern Hemisphere, and the Great White Storm of 2010. The Cassini data has been compared with data collected by the Voyager missions (Desch & Kaiser, 1981; Porco et al., 2005; Read, Conrath, et al., 2009) and the Hubble Space Telescope (HST) (Sánchez-Lavega et al., 2003, 2004, 2006) to increase our knowledge of the seasonal patterns and to determine if there have been any large-scale atmospheric changes.

The axial inclination of Saturn is 27.9° — similar to Earth at 23.5° — which results in clearly defined seasonal cycles yielding large variations of incoming solar flux. Additional variations in the incoming solar flux are caused by Saturn's high orbital eccentricity, 0.0541, the highest of our solar system's gas giants, along with the presence of Saturn's ring system. The ring system is composed primarily of water ice and ranges from the inner edge of the D-ring (6,630 km from the equatorial surface of Saturn) to the outer edge of the E-ring (420,000 km), approximately eight times the diameter of this gas

giant (Williams, 2015). In most orientations, the rings effectively block the incoming sunlight in the equatorial regions, creating shadows across Saturn's surface. However, there are certain configurations that allow visible light to be reflected and scattered on Saturn's atmosphere (Mishchenko, 1993).

Each challenge is an opportunity to further our understanding of this gas giant. The rings of Saturn, first noted in the 17th century, create a shadow on the surface of the planet, which impedes atmospheric measurements. Cassini captured a multitude of data about the rings, which expanded our knowledge of their origin and composition, and showed structures that may only have been noted during an extended mission.

When Cassini entered orbit on June 30, 2004, it was the summer season for Saturn's Southern Hemisphere (SH). During the Southern Hemisphere summer, the rings' shadows fall across the Northern Hemisphere (NH), restricting atmospheric observations in the lower latitudes. Because of this configuration, the Prime Mission focused on the Southern Hemisphere. In August 2009, Saturn experienced the first equinox since Cassini's arrival. This allowed the shadows of the rings to shift to the Southern Hemisphere, yielding an unobscured view of the Northern Hemisphere. Not ironically, this transition occurred during the Cassini Equinox Mission.

The extension of Cassini's voyage with the Solstice Mission granted scientists another seven years of data. As Cassini transitioned from the Equinox Mission to the Solstice Mission, data acquisition focused on the transition from the start of Northern Hemisphere spring to the summer, extending a few months beyond the Northern Hemisphere solstice. The Solstice Mission allowed for an additional 155 orbits around Saturn, along with additional exploration of its rings and major satellites, Titan and Enceladus (Dunford et al., 2017).

At the end of the mission life cycle, the decision was made to plunge Cassini into Saturn's atmosphere. This Grand Finale was designed to prevent Cassini from contaminating the Saturnian moons with its hydrazine propellant. During the last five months of the mission, Cassini performed twenty-two more orbits between Saturn and its rings. Then, on September 15, 2017, Cassini was directed to enter Saturn's atmosphere, collecting and sending data until the very end ("Grand Finale – Cassini Bids Farewell", 2017).

During these final twenty-two fly-bys, the orbits were adjusted to pass 1,600 to 4,000 kilometers above the clouds to better observe their structure. During the last five orbits, Cassini passed through the outer layers of the atmosphere, which yielded unprecedented images and access to high-resolution data.

1.1 Motivation

The work presented here focuses on the results of the study of atmospheric data collected by Cassini during its primary and extended missions of Saturn. The results of this study yielded an increased understanding of the spatial and temporal patterns of Saturn's wind fields. Wind fields play an important role in the climatology and meteorology in the atmosphere of any celestial body, as they establish the basic environment for atmospheric dynamic processes. These processes occur on all four atmospheric scales, ranging from eddies and vortices in the microscale, to storms in both the mesoscale and synoptic scale, to global scale waves (e.g., Batchelor 1967, Holton & Hakim 2013, Pedlosky 1987). The wind fields of Saturn extend from the upper troposphere, across the tropopause, and outward into the stratosphere, which gives us the ability to map the atmosphere in a global three-dimensional view over seasonal time scales.

This research lays the foundation for understanding Saturn's atmospheric changes over time on a global scale and provides additional insight into atmospheric changes potentially driven by the eddy momentum fluxes, along with its seasons and the associated changes in incoming solar flux.

In order to better understand the concepts and physical laws that govern the universe, we, as a scientific community, need to study more than Earth. In our solar system, one tiny corner of the galaxy, there exists unique planets to study and learn from. With the recent burst of exoplanets being discovered, understanding what is in our own galactic backyard can help us begin to better comprehend what we are seeing across the light years.

1.2 Dissertation Overview

This dissertation research is comprised of four tasks. The first task (Chapter 3) offers an overview of the thermal wind equation (TWE), which provides a mathematical relationship between the vertical shear of the horizontal winds and the horizontal temperature gradient along isobaric surfaces. In its simpler “standard” form, the approximations that are associated with large-scale atmospheric motion – conditions of geostrophic and hydrostatic balance, are made in its derivation.

It is noted that these two assumptions are not always valid, particularly in the equatorial regions of the gas giants, where there are strong atmospheric jets and rapid rotational periods. To account for these variances, a more “general” form of the TWE will be derived; the validation of this new form will be conducted with NCEP2 reanalysis data.

This new form will be apposite to numerical evaluation and applicable across all regions of planetary atmospheres.

The second task (Chapter 4) is a direct extension of the derivation and validation work conducted in Chapter 3. Through the application of the forms of the TWE were developed in the previous chapter to upper atmospheric data, an increased understanding of Saturn's vertical structure of the zonal winds was attained. The analysis demonstrated the low-latitude jets of the NH weakened with altitude, similar to what previous research demonstrated in the SH. Additionally, research will also be focus on the strength and longevity of the stratospheric jets in the equatorial zone.

The third task (Chapter 5) generated the first global profile of the zonal winds within the deep troposphere, ~2,000-mb level. Comparisons of the deep winds were made to those of the upper troposphere, ~300- to 500-mbar level, with generally consistent results, but also notable differences. The two sets of zonal wind data were also analyzed to assess the stability within Saturn's troposphere. Finally, focus was shifted to both of the polar regions to examine their temporal variations of the deep tropospheric jets, over extended period and through seasonal changes.

The fourth and final task (Chapter 6) will present an overview and analysis of the Great White Storms of Saturn. Of particular note, the 2010 storm was examined with specific attention to its lopsided structure, particularly in the mature and dissipation phases. As a means to better comprehend its asymmetric structure, the zonal-mean quasi-geostrophic potential vorticity (QGPV) will be derived and used to understand if strong gradients on the zonal-mean QGPV would inhibit cloud mixing in the meridional direction.

While this work provides new insights and understandings into the spatiotemporal changes in the Saturnian atmosphere, I take pride in knowing that future researchers will be able to use our results for the extension of their scientific pursuits.

Chapter 2: Atmospheric Structure of Saturn

Since Galileo Galilei first observed Saturn through a telescope in 1610, scientists have been fascinated by the ringed planet. In 1655, Christiaan Huygens proposed that “handles” that had been noted by Galileo was actually a thin, flat ring. Earth-based observations of Saturn’s atmosphere for the purpose of studying its winds were less notable, since tropospheric haze obscures the troposphere’s cloud patterns.

In 1876, the first observation of the Great White Storm (GWS) was made by Asaph Hall, a professor at the United States Naval Observatory (USNO). He used these observations to establish Saturn’s period of rotation, which is a topic that has still not been well-defined to this date. The GWS was believed to be a semi-periodic event, occurring at ~28.5-year intervals. However, the GWS of 2010 was “early”, given that the previous one was in 1990. This event’s timeline and its unique development will be reviewed in Chapter 6.

The zonal winds of Saturn have been a topic of great interest since the Voyager missions in the early 1980s. While the research presented here specifically examines the images collected by Cassini, challenges have been encountered by all platforms that have collected atmospheric data from Saturn. The major challenges faced include the shadow

cast by the planet's rings and the cold temperatures that lead to multiple cloud layers through the troposphere.

The calculation of the zonal winds through the troposphere is dependent upon observations of clouds, which are used as passive tracers of atmospheric mass motion. A layer of haze in the tropopause obscures the clouds within the troposphere, reducing the tropospheric clouds. Moreover, the observations of these tropospheric cloud layers are compounded by a deep scale height in the upper troposphere on the order of 60 km (Li et al., 2008), which yields increased scattering of light.

The Cassini platform was designed to account for these challenges with the integration of the Composite Infrared Spectrometer (CIRS), Imaging Science Subsystem (ISS), and the Visible and Infrared Mapping Spectrometer (VIMS) platforms. The data collected by these systems will be used through the remainder of this dissertation.

2.1 Atmospheric Profile of Saturn

The atmospheric structure of Saturn is analogous to that of Earth with the troposphere, tropopause, and stratosphere being relevant to this research. Figure 2.1 shows a vertical

cross-section of Saturn's atmosphere with the known cloud levels represented, along with its thermal profile.

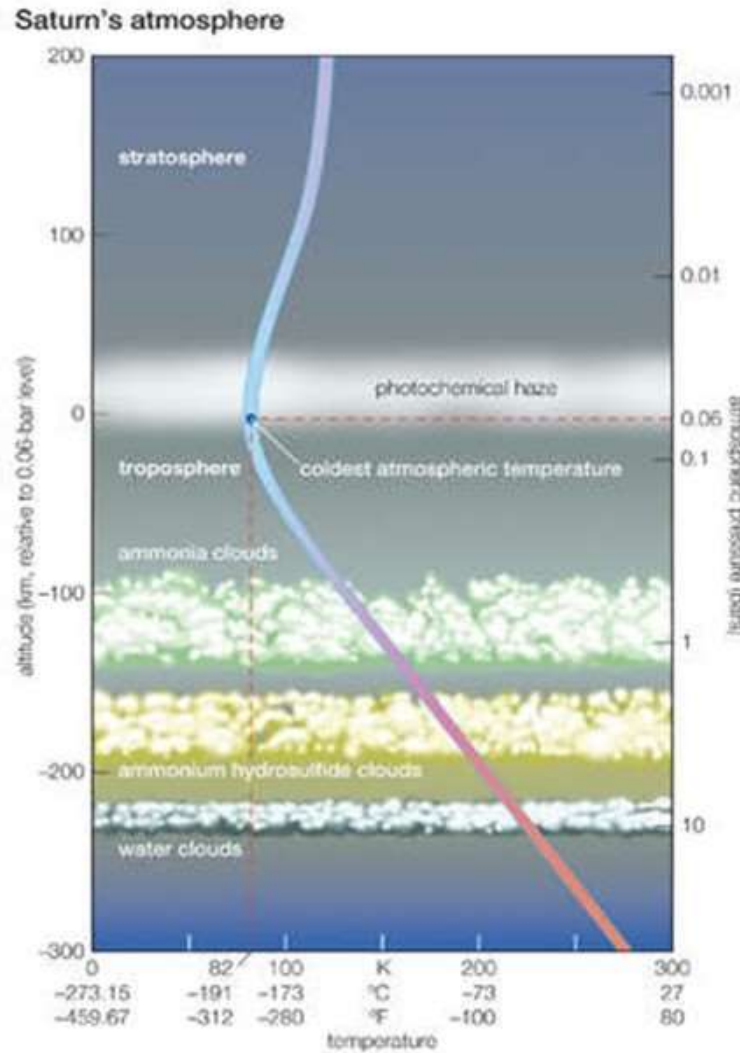


Figure 2.1. Cross-section of Saturn's atmosphere. This image shows the cloud layers that were observed by the ISS and VIMS during the Cassini mission, extending from the water clouds in the deep troposphere, ~10 bar, across the tropopause ~0.05 – 0.1 bar, and outward into the stratosphere, ~0.001 bar. A temperature profile is displayed across the same atmospheric expanse, ranging from ~270K (80°F/27°C) in the deep tropopause down to a minimum of 82K (-312°F/191°C). Similar to Earth's atmosphere, temperatures rise in the stratosphere to ~100K (-280°F/173°C) (Hubbard, Buratti, & Marley, 2020).

In order to expand our understanding of the vertical structure of Saturn's atmosphere, an analysis of Cassini ISS data was conducted. The atmospheric depths examined by the ISS included the photochemical haze observed across the tropopause (~10 to 60 mbar) with two methane band filters, MT2 and MT3 (Del Genio & Barbara, 2012; Dyudina et al., 2009; Li et al., 2011; Sánchez-Lavega et al., 2007).

Additionally, two continuum band filters, CB2 and CB3, of the ISS were used to examine the top of the ammonia clouds, which extend from about 500 to 1,000 mbar through the troposphere. It is estimated that the measured winds extend from approximately 300 to 700 mbar (Antuñano et al., 2018; Dyudina et al., 2008, 2009). It should be noted here the cloud heights were estimated via equilibrium chemical modeling and are believed to be variable, due to both seasonality and zonal location across Saturn (Merlet, 2011).

At the levels of interest for the VIMS data, two different cloud layers were examined, the aforementioned ammonia clouds and ammonium hydrosulfide clouds, which are located between the 3,000- and 5,000-mbar levels. Beyond that, a layer of water clouds resides at about the 10,000-mbar level; however, these were not observed during the Cassini mission.

In order to complete our understanding of the vertical structure of Saturn's atmosphere, an analysis of Cassini CIRS data was conducted. While the ISS and VIMS captured evidence of clouds from the tropopause inward through the troposphere to determine zonal wind speeds, the CIRS collected radiance data through portions of the stratosphere, across the tropopause, and into the upper extent of the troposphere.

The radiance data collected by the CIRS was manipulated and applied to a form of the thermal wind equation (TWE), which yield zonal wind output over a range of time. These results were examined, combined with analysis of ISS data, to establish the historical trends of Saturn's upper atmosphere. (The specifics of the TWE and the analysis of the upper-level winds will be presented in Chapters 3 and 4, respectively.)

2.2 Uncertainty of Saturn's Rotation Period

The rotation period of Saturn is an important factor in the determination of the zonal wind speeds when using ISS and VIMS data from the Cassini mission. While the details of the zonal wind calculations will be presented in Chapters 4 and 5, a short explanation is that amount of cloud motion over time is used to determine the wind speeds. The distance that the cloud transited must account for its own motion as it is advected by the zonal winds, along with accounting for the planet's rotation. In some cases, slight

differences in the rotational period, on the order of minutes, can produce the difference between easterly and westerly winds.

As noted earlier, Hall observed a great white storm in December 1876. Working with five other observatories across the eastern United States, which collected transit and timing data, he calculated a rotation period of $10\text{h } 14\text{m } 23.8\text{s} \pm 2.3\text{s}$ (Hall, 1877). He noted that only other derivation of Saturn's rotation period that he knew of was conducted by Sir William Herschel with data collected during late 1793 and into early 1794. Herschel (1794) calculated a rotation period of $10\text{h } 16\text{m } 0.4\text{s} \pm 2\text{m}$.

The rotation period estimates continued to evolve through the centuries with examinations of optical data, along with data from the Pioneer and Voyager missions. Kaiser et al. (1980) used Voyager Planetary Radio Astronomy data to estimate a period of $10\text{h } 39\text{m } 54\text{s} \pm 36\text{s}$. Derivation techniques continued to evolve and Desch and Kaiser (1981) established a rotation period of $10\text{h } 39\text{m } 24\text{s} \pm 7\text{s}$. This value has become the benchmark for much of the previous research conducted in the determination of Saturn's zonal winds. This higher value for the rotational period yielded lower easterly speeds. However, if the rotation period of $10\text{h } 33\text{m } 24\text{s}$ (Studwell et al., 2018) is used, which was based on more recent rotation period estimates using data from the Cassini mission, the

easterly jets will show a higher zonal velocity, which would subsequently impact other atmospheric variables, including momentum flux calculations.

Chapter 3 (Task 1): Thermal Wind Equation

The thermal wind equation provides a mathematical relationship between the vertical shear of the horizontal winds and the horizontal temperature gradient along isobaric surfaces. The formulation of the standard form of the TWE is a result of two atmospheric conditions: the geostrophic balance and the hydrostatic balance.

The assumption of geostrophic balance applies to large-scale fluid motions where the horizontal components of the Coriolis and pressure gradient forces are in equilibrium. The horizontal plane is often used as the reference frame for geostrophic balance; this is the place in which the horizontal components of the Coriolis and pressure-gradient forces are balanced along this axis. The hydrostatic balance is defined as a static equilibrium between the gravity force and vertical component of the pressure gradient force, i.e., buoyancy. Even when a fluid is in motion, this application of the Archimedes' principle is valid when vertical accelerations due to external forces, other than gravity and vertical pressure gradient, are negligible. Therefore, in most scenarios, the hydrostatic balance yields a good approximation for horizontal large-scale motion.

The physical representation of the TWE can be made as follows: The spatial distribution of temperatures produces the tilting of constant-pressure surfaces. The magnitude of the

tilting of a constant-pressure surface in the vertical is related to the magnitude of the horizontal temperature gradient, which yields the vertical shear of the geostrophic winds. Conversely, the temperature profile can be established by knowing the structure of the horizontal winds and the appropriate boundary conditions.

When examining large-scale motions within planetary atmospheres, which is the basis of this dissertation research, the TWE is a powerful tool. However, even a powerful tool has its operational limits.

In the equation's more common form, the "standard thermal wind equation", some assumptions, which will be reviewed in Section 3.2, are made in order to make its application more accessible. However, these assumptions render the equation inaccurate in some environments, particularly in equatorial regions with strong atmospheric jets and rapid rotation period, e.g., gas giants, such as Jupiter and Saturn (Li et al., 2007). A more generic form is offered in the "general thermal wind equation," whose derivation will be presented in Section 3.2 and its validation shown in Section 3.3.

3.1 Previous Research

The thermal wind equation is based on two principle meteorological concepts: geostrophic and hydrostatic balance. The concept of geostrophic balance, which is the balance between Coriolis and pressure gradient forces, was discovered early in the 19th century and is now considered to a foundational concept in both meteorology and oceanography (de Verdiere and Schoop, 1994). The history of the hydrostatic balance principle harkens back to the story of Archimedes shouting “Eureka!” and the quantification of these principles by Galileo Galilei in *La Bilancetta*, published in 1644. The first combination of these concepts was made by Vernon and Ashburn (1938) in an effort to overcome gaps in upper-air observations, which led to their derivation and validation of the standard TWE.

The standard TWE came under scrutiny with Phillips (1963) as it noted that there are two classes of geostrophic flow: 1) Case defined by a horizontal length scale, L , being smaller than the Earth’s radius, and 2) Case where L is comparable to the Earth’s radius. Extending on the work of Phillips (1963), where he noted “a consistent approximation procedure has not yet been developed for low latitudes”, de Verdiere and Schoop (1994) demonstrated that the standard TWE ceased to provide valid approximations in the

equatorial region and was bound by mathematical limitations. (Further discussion and analysis of these restrictions will be presented in Sections 3.2 and 3.3.)

A more general form of the TWE was developed in de Verdiere and Schoop (1994), stemming from a vorticity perspective. Based on infrared observations of Jupiter's upper troposphere, de Latorre Juárez et al. (2002) also presented a derivation of a more general form of the TWE based on the primitive equations and used a full Coriolis force. The work included both the horizontal and vertical projections of the planet's rotation vector, which is valid in both shallow and deep atmospheres, allows for its' spherical geometry and oblateness, does not yield a mathematical singularity at the equator, and also provides some information about localized vertical velocities. However, this research also examined the implications of the hydrostatic approximations and proposed an alternative approach. Finally, their new general form was applied to the Jovian upper tropospheric temperature data from its equatorial region, 15°N to 15°S, yielding new information on Jupiter's zonal jets.

While it had been well-established that the assumption of geostrophic balance becomes less valid as one approaches the equator, the horizontal plane is often used to be the reference frame for geostrophic balance; this is the place in which the horizontal

components of the Coriolis and pressure-gradient forces are balanced along this reference frame. Other physical factors can be emphasized regarding the shortcomings of the standard TWE, including substantial variations of the large-scale zonal winds, rapid rotation periods, and the larger radii noted in the gas giants of our solar system. These factors can yield atmospheric forces, while minimized in the standard equation with the assumptions of geostrophic and hydrostatic balance, are actually not negligible in the equatorial regions.

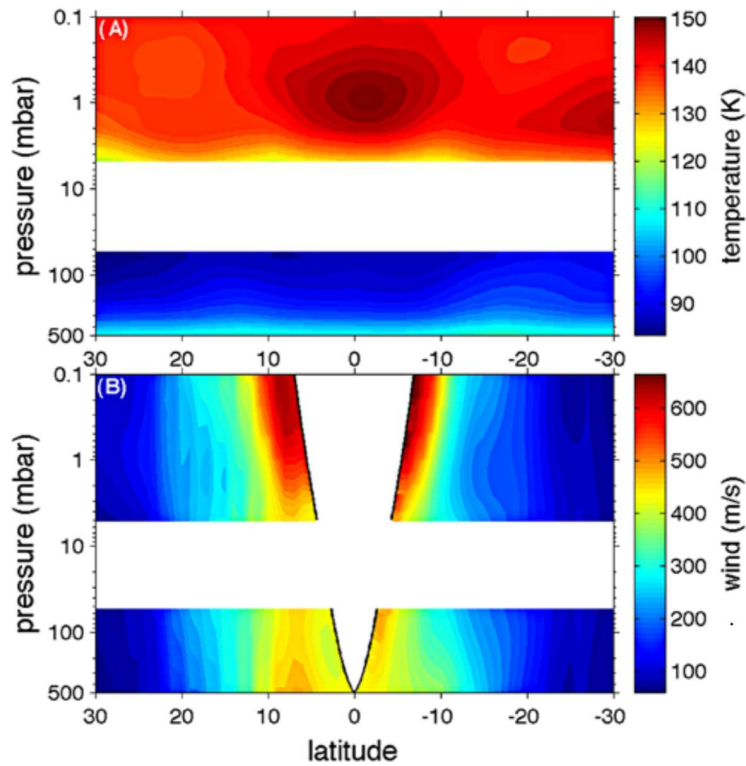


Figure 3.1. Zonal-mean CIRS temperatures and the derived thermal winds. Panel A shows the temperatures averaged over a ~ 4 -year period. Panel B shows thermal winds calculated by the modified TWE. The 500-mbar zonal winds collected by the Cassini ISS and Voyager are used for the boundary condition. The area inside the black lines is indicative of the area where the modified TWE still does not apply (Li et al., 2008).

Even with the implementation of the modified TWE, Li et al. (2008) shows the limitations of the methodology. Figure 3.1 shows a segment emanating from the 500-mbar level, which was used as the lower boundary condition with known zonal wind levels. The integration of the modified TWE was conducted along cylinders parallel to Saturn's rotation axis using CIRS high spatial resolution radiance maps. However, with this form of the TWE, it still does not work for the region inside the two-dimensional segment, equatorward and above the cylinders that were tangent to the equator at the 500-mbar level. Similar results were also noted in Li et al. (2011, 2016), which focused upon radiance output from the equatorial region. In both of these studies, the limitations due to the integration methods exhibited themselves in a two-dimensional segment in which the zonal wind output could not be derived.

Allen and Sherwood (2007) took an inverse approach to the application of the TWE. The core of their research was to examine the trends in tropospheric warming on Earth, specifically in the tropical region of the West Pacific Ocean. The analysis examined the radiosonde wind data and applied the TWE to establish long-term trends in upper-level temperatures in this region. The results demonstrated that radiosonde wind data offered guidance on the horizontal structure on monthly and seasonal-scale changes in tropospheric temperatures. However, the authors also made emphasized that the

equatorial limitations of the TWE remains, singling out the fact that the Coriolis force approaches zero in this region.

3.2 Forms of the Thermal Wind Equation

In the ideal case, the vertical wind shear is related to the horizontal temperature gradient along isobaric surfaces through the application of the TWE. Using this relationship, if the temperature distribution is known through a section of the atmosphere, the vertical structure of the winds can be derived, and vice versa.

Two versions of the TWE will be reviewed through the remainder of Chapter 3: The standard version of the equation, using the assumptions of geostrophic and hydrostatic balance will be presented in Section 3.2.1; the general form of the equation, which will discard the presumptions of geostrophic balance and the hydrostatic approximation will be shown in Section 3.2.2. It should be emphasized that these two forms are not mutually exclusive. Rather, a combination of the general and standard forms can be used to establish a global zonal wind profile of even gas giant planets with deep atmospheres.

To validate the general form of the TWE, it will be applied to a reanalysis data set from Earth (Section 3.3.1). Additionally, both forms of the TWE will be applied to CIRS data,

which was collected during the Cassini mission to Saturn, and the results compared in Section 3.3.2.

3.2.1 Standard Form of the Thermal Wind Equation

As mentioned earlier in Chapter 3, the standard form of the TWE is based upon two meteorological principles: geostrophic and hydrostatic balance. By mathematically combining these two principles with the concept of geostrophic winds to yield the standard form of the TWE, this provides a basis to relate vertical shear in the geostrophic winds with the horizontal temperature gradients along isobaric surfaces.

The derivation and use of either form of the TWE are based in spherical coordinates (λ , ϕ , r) fixed in the rotating planet, where λ is longitude, ϕ is latitude, and r is the radial distance from the planet's center. Similarly, both forms of the TWE are based upon the geostrophic winds, which for the zonal wind, u , is (Batchelor, 1967; Holton, 1979; Pedlosky, 1987)

$$fu = \frac{-1}{\rho r} \frac{\partial p}{\partial \phi}. \quad (1)$$

where f is the Coriolis parameter ($f = 2\Omega \sin \phi$, where Ω is the angular speed of the planet's rotation), ρ is the atmosphere's density, and p is the atmospheric pressure.

By differentiating (1) with respect to r , Equation 2 is obtained

$$f \frac{\partial u}{\partial r} = \frac{\partial}{\partial r} \left(\frac{-1}{\rho r} \frac{\partial p}{\partial \phi} \right) = \frac{1}{\rho r} \frac{\partial p}{\partial \phi} \left(\frac{1}{r} + \frac{1}{\rho} \frac{\partial \rho}{\partial r} \right) - \frac{1}{\rho r} \frac{\partial^2 p}{\partial \phi \partial r}. \quad (2)$$

The definition of the radial distance, r , is dependent upon the nature of the planet that is being studied. For Earth and other terrestrial planets and moons, it is defined as distance from the surface, r_s , to the top of the atmosphere. For gaseous planets, the radial distance is defined as the distance from the reference level, r_c , to the atmosphere's outer extent.

In most cases, the term $1/r$ is much smaller than $(1/\rho)(\partial p/\partial r)$, noted as the first term on the right side of (2), because r is much larger than the density scale height, $(-\rho)/(\partial \rho/\partial r)$, which are about 8 and 60 km on Earth and Saturn, respectively. (For the purpose of the scale analysis, the density scale height will be treated as having an order of magnitude of 10 km.)

By applying the principle of hydrostatic balance in the radial direction, $\partial p/\partial r = -\rho g$, where g is the planet's gravitational acceleration, (2) can be simplified as

$$f \frac{\partial u}{\partial r} = \frac{1}{\rho^2 r} \frac{\partial p}{\partial \phi} \frac{\partial \rho}{\partial r} + \frac{g}{\rho r} \frac{\partial \rho}{\partial \phi} = \frac{1}{\rho^2 r} \left(\frac{\partial p}{\partial \phi} \frac{\partial \rho}{\partial r} - \frac{\partial p}{\partial r} \frac{\partial \rho}{\partial \phi} \right)$$

$$f \frac{\partial u}{\partial r} = - \frac{1}{\rho^2 r} \frac{\partial p}{\partial r} \left(\frac{\partial \rho}{\partial \phi} - \frac{\partial p/\partial \phi}{\partial p/\partial r} \frac{\partial \rho}{\partial r} \right) = \frac{g}{\rho r} \left(\frac{\partial \rho}{\partial \phi} + \frac{\partial r}{\partial \phi} \Big|_p \frac{\partial \rho}{\partial r} \right). \quad (3)$$

Through the application of the ideal gas law, $p = \rho RT$, where R is the specific gas constant, which itself is the ratio of the universal gas constant, R^* , and the mean molecular weight of the atmosphere, and T is the temperature, (3) can be rewritten as

$$\frac{\partial u}{\partial r} = \frac{g}{f\rho r} \left(\frac{\partial \rho}{\partial \phi} + \frac{\partial r}{\partial \phi} \Big|_p \frac{\partial \rho}{\partial r} \right) = \frac{g}{f\rho r} \frac{\partial \rho}{\partial \phi} \Big|_p = \frac{-g}{fTr} \frac{\partial T}{\partial \phi} \Big|_p. \quad (4)$$

Similarly, the TWE for the meridional wind, v , is

$$\frac{\partial v}{\partial r} = \frac{g}{fTr \cos \phi} \frac{\partial T}{\partial \lambda} \Big|_p. \quad (5)$$

3.2.2 General Form of the Thermal Wind Equation

As noted previously, the assumption of geostrophic balance is not valid due to the negligible Coriolis force in equatorial regions. It is noted though that the calculation methods proposed in Marcus et al. (2019), though that also yielded theoretical errors of $\pm 10\%$ in the tropical regions of Jupiter, which could be smaller than generated through the use of the standard TWE.

Several additional factors noted in the Saturnian atmosphere, particularly in the equatorial region, render the assumptions behind the standard form of the TWE unusable. In addition to the Coriolis force weakening closer to the equator, substantial variations of the large-scale equatorial jets along with a rapid rotation period results in

the forces that are the hydrostatic and geostrophic balance terms are not negligible. The derivation of the general form of the TWE will be presented hereafter, along with a physical interpretation.

3.2.2.1 Derivation of the General Thermal Wind Equation

The complete form of the momentum equations in the meridional (ϕ) and radial (r) directions can be written as (Batchelor, 1967, Pedlosky, 1987, Holton & Hakim, 2013)

$$\frac{Dv}{Dt} - \frac{u^2 \tan \phi}{r} + \frac{vw}{r} = -\frac{1}{\rho r} \frac{\partial p}{\partial \phi} - 2\Omega u \sin \phi - \frac{1}{r} \frac{d\Phi}{d\phi} + F_\phi \quad (6)$$

$$\frac{Dw}{Dt} - \frac{u^2 + v^2}{r} = -\frac{1}{\rho r} \frac{\partial p}{\partial r} - 2\Omega u \cos \phi - \frac{d\Phi}{dr} + F_r. \quad (7)$$

where w is the velocity in the radial direction, Φ is the effective geopotential, defined as the sum of the geopotential due to the planet's gravity, $\Phi_1(\phi, r) = \int g(\phi, r) dr$ and due to the rotation of the planet, $\Phi_2(\phi, r) = -\Omega^2 r$. The terms, $\frac{1}{r} \frac{d\Phi}{d\phi}$ and $\frac{d\Phi}{dr}$, on the right-hand sides of (6) and (7), respectively, come from the planet's oblateness. The F_ϕ and F_r terms are frictions in the meridional and radial directions, respectively. The total derivative, D/Dt , can be expanded in a spherical coordinate system as:

$$\frac{D}{Dt} = \frac{\partial}{\partial t} + u \frac{\partial}{r \cos \phi \partial \lambda} + v \frac{\partial}{r \partial \phi} + w \frac{\partial}{\partial r}.$$

In conducting a scale analysis of the large-scale flow, it is noted that for almost all of the planets of our solar system the following relation of scale applies that: $U \gg V \gg W$, where

U , V , and W are the scales of the zonal wind u , meridional wind v , and the vertical wind w , respectively. Additionally, it is assumed that the time scale of the large-scale flow is L/U , where L is the length scale of the large-scale motion. Continuing with the scalar analysis, it can be presumed that the large-scale flow is steady, symmetrical around all three axes, and that friction can be neglected. This allows for (6) and (7) to be simplified

$$\frac{u^2 \tan \phi}{r} + \frac{1}{\rho r} \frac{\partial p}{\partial \phi} + 2\Omega u \sin \phi = -\frac{1}{r} \frac{d\Phi}{d\phi} \quad (8)$$

$$\frac{-u^2}{r} + \frac{1}{\rho} \frac{\partial p}{\partial r} - 2\Omega u \cos \phi = -\frac{d\Phi}{dr}. \quad (9)$$

Equation (9) is reached by taking $(\partial/\partial r)r$ on (8) and $(\partial/d\phi)$ on (9), then subtracting those results in order to cancel the geopotential term, Φ .

$$\left(\tan \phi \frac{\partial}{\partial r} + \frac{1}{r} \frac{\partial}{\partial \phi} \right) (u^2 + 2\Omega u r \cos \phi) + \frac{\partial}{\partial r} \left(\frac{1}{\rho} \right) \frac{\partial p}{\partial \phi} - \frac{\partial}{\partial \phi} \left(\frac{1}{\rho} \right) \frac{\partial p}{\partial r} = 0. \quad (10)$$

By defining \hat{z} as the unit vector along the planet's axis of rotation and $\hat{\lambda}$ as the unit vector in the longitudinal direction, (10) can be multiplied by $1/r$. The first term can be projected in \hat{z} direction, while the second and third terms can be projected in the $\hat{\lambda}$ direction, resulting in

$$\hat{z} \cdot \nabla \left(\frac{u^2 + 2\Omega u r_c}{r_c} \right) + \hat{\lambda} \left(\nabla \frac{1}{\rho} \times \nabla p \right) = 0. \quad (11)$$

where $r_c = r \cos \phi$, which is the cylindrical radius at latitude ϕ .

Through the application of the ideal gas law, the second term of (11) can be written as

$$\begin{aligned}\hat{\lambda} \left(\nabla \frac{1}{\rho} \times \nabla p \right) &= \frac{R}{pr} \left(\frac{\partial T}{\partial \phi} \frac{\partial p}{\partial r} - \frac{\partial T}{\partial r} \frac{\partial p}{\partial \phi} \right) = \frac{R}{pr} \frac{\partial p}{\partial r} \left(\frac{\partial T}{\partial \phi} - \frac{\partial p / d\phi}{\partial p / dr} \frac{\partial T}{\partial r} \right) \\ \hat{\lambda} \left(\nabla \frac{1}{\rho} \times \nabla p \right) &= \frac{R}{pr} \frac{\partial p}{\partial r} \left(\frac{\partial T}{\partial \phi} - \frac{\partial r}{\partial \phi} \Big|_p \frac{\partial T}{\partial r} \right).\end{aligned}\quad (12)$$

The application of the chain rule of partial derivatives to (12) yields

$$\hat{\lambda} \left(\nabla \frac{1}{\rho} \times \nabla p \right) = \frac{R}{pr} \frac{\partial p}{\partial r} \left(\frac{\partial T}{\partial \phi} - \frac{\partial r}{\partial \phi} \Big|_p \frac{\partial p}{\partial \phi} \right) = \frac{R}{pr} \frac{\partial p}{\partial r} \frac{\partial T}{\partial \phi} \Big|_p. \quad (13)$$

Combining (11) and (13) results in:

$$\frac{\partial}{\partial z} \Big|_{r_c} \left(\frac{u^2 + 2\Omega u r_c}{r_c} \right) = \frac{R}{pr} \frac{\partial p}{\partial r} \frac{\partial T}{\partial \phi} \Big|_p. \quad (14)$$

Equation (14) yield a form of the general TWE which provides a relationship between large-scale zonal winds and the horizontal temperature gradient. This version of general TWE is applicable across planetary atmospheres, including the equatorial region, and is also in a form suitable for numerical evaluation.

By applying the two assumptions used in the derivation of the standard TWE, i.e., hydrostatic balance, $dp/dr = -\rho g$, and geostrophic balance, which states $u \ll \Omega r_c$, except in the polar regions, (14) can be simplified to:

$$2\Omega \frac{\partial u}{\partial z} \Big|_{r_c} = \frac{-R\rho g}{pr} \frac{\partial T}{\partial \phi} \Big|_p = \frac{-g}{Tr} \frac{\partial T}{\partial \phi} \Big|_p. \quad (15)$$

In general, the standard TWE works well for large-scale motion in middle to high latitudes. This is confirmed in (15) with the application of the geostrophic and hydrostatic balance assumptions to (14). However, the general TWE cannot be transformed to the standard form for a “thick” atmosphere. An example of this is Saturn’s moon, Titan; the atmospheric thickness is on the same order of magnitude as the moon’s reference radius. In this case, the estimation of $\partial z = dr / \sin \phi$ cannot guarantee that the two integration methods applied, i.e., the radial direction with the standard TWE versus the cylindrical direction in general form, are roughly the same.

3.2.2.2 Physical Interpretation of the General Thermal Wind Equation

The general TWE provides a tool to diagnose atmospheric winds when a thermal profile is known and does not include the limitations that have been discussed with regards to the standard form. In examining (14), the right-hand side characterizes the change of centrifugal and Coriolis forces in the direction of the rotating axis, which is a result of the derivative of these forces in the meridional (ϕ) and radial (r) directions. Additionally, the left-hand side of (14) shows the temperature change along an isobaric surface, which can be altered to represent changes of the pressure gradient force in the meridional and radial directions. Therefore, (14) represents the balances between the variations of the forces in different directions rather than the balances of the forces themselves in the momentum

equations, (8) and (9). From this perspective, (14) is the same as (4), the standard form, which also represents a balance of the vertical variations between the pressure gradient and Coriolis forces.

Equation (11) also proposes a balance between the turning forces that represent the drives for the zonal component of vorticity behind the general form of the TWE (14). One of the forces is a consequence of the gradients of the Coriolis and centrifugal forces, while the other is the solenoidal term, arising from the baroclinicity of the atmosphere.

The atmosphere is unable to achieve balance at the equator because the Coriolis force is zero. Therefore, examination of (8) shows that the pressure gradient force is unable to balance in the meridional direction. Because of this inability, the centrifugal acceleration and the Coriolis force modify the pressure field in a manner that eliminates the meridional pressure gradient. This is accomplished through the modification of the effective gravity, which offsets the atmosphere's expansion or contraction that would be caused by temperature variations.

In general, the variations in the temperature field will yield the contraction or expansion of the atmosphere, subsequently resulting in the horizontal pressure gradient. To

demonstrate this point, consider a hypothetical cylinder positioned at the equator and extending horizontally. The distance between the two flat surfaces is defined as Δr with constant pressure on each end of p and $p + \delta p$. Applying the approximation, $\partial\Phi/\partial r \sim g$ to (9) yields

$$\Delta r = -\frac{\delta p}{\rho} \left(g - \frac{u^2}{r} - 2\Omega u \right)^{-1}. \quad (16)$$

The distance between the ends of the cylinder is dependent upon the temperature, through density, ρ , and also the zonal wind, u , through the deduction of the effective gravity by the centrifugal and Coriolis forces.

In order to remove the pressure gradient along the rotating axis, \hat{z} , which is the same as the meridional axis, $\hat{\phi}$, at the equator, the distance Δr between the two pressure surfaces must not change along the rotating axis, \hat{z} . Mathematically, this can be shown as

$$\frac{\partial(\Delta r)}{\partial z} = 0 \Rightarrow \frac{\partial}{\partial z} \left[\frac{\delta p}{\rho} \left(g - \frac{u^2}{r} - 2\Omega u \right)^{-1} \right] = 0. \quad (17)$$

By applying the ideal gas law to eliminate ρ and assuming that the centrifugal and Coriolis forces are much smaller than gravity at the equator, (17) can be rewritten as

$$\frac{\partial}{\partial z} \left(\frac{u^2}{r} + 2\Omega u \right) = -\frac{g}{T} \frac{\partial T}{\partial z} = \frac{R}{p} \frac{\partial p}{\partial r_c} \frac{\partial T}{\partial z}. \quad (18)$$

Equation (18) is the TWE in cylindrical coordinates, which is the same as (14) at the equator when $\cos \phi = 1$ and $\partial z = r \partial \phi$.

The two forms of the general forms of the TWE that were derived, (14) and (18), suggest that a unique balance exists at the equator in which the centrifugal and Coriolis forces modify the gravity field, such that the thickness of the atmosphere does not change between the two surfaces of constant pressure. The constant thickness of the atmosphere aids in the elimination of the pressure gradient force along the meridional axis.

This unique physical balance at the equator yields a different scale analysis for the relationship between temperature gradients and the thermal winds in the tropics, spanning from the mid-latitudes to the equatorial region. Within the mid-latitudes, we can use the following approximations, $(\partial p / \partial r) / p = -1/H$, where H is scale height, and $\partial z = H / \sin \phi$. Additionally, it can be assumed that $r \partial \phi = L$ in the meridional direction, the scaling relationship based on (14) is

$$\frac{\Delta U^2}{r} = -2\Omega \Delta U = \left(\frac{H}{L}\right) \frac{R\Delta T}{H}. \quad (19)$$

Within the equatorial region, (18) can be used to do a scale analysis,

$$\frac{\Delta U^2}{r} = -2\Omega \Delta U = \frac{R\Delta T}{H}. \quad (20)$$

The factor H/L exists the mid-latitudes and the equatorial region. In general, the horizontal length scale, L , is much larger than the scale height. Therefore, winds are much more sensitive to temperature variations in the equatorial region, compared to the mid-

latitudes. When there is a dynamic constraint on the wind's magnitudes, this implies only relatively small temperature constraints can exist near the equator. The implication contributes to the explanation of why some planets within our solar system have relatively small temperature gradients in their equatorial regions.

3.3 Comparison of the Thermal Wind Equations

The two forms of the TWE, the general and the standard, are both useful for deriving the VWS across a region with a known horizontal temperature gradient and vice versa. However, each form is unique and have their own advantages and differences.

The fundamental difference between the two equations is that general TWE does not include the assumption of geostrophic and hydrostatic balance, which is used for the standard TWE. In theory, the general form of the TWE provides a more exact relationship between the thermal fields and the large-scale atmospheric dynamics. With regards to this dissertation, the derivation of the general form of the TWE is directed at better understanding the spatiotemporal variations of the zonal winds across Saturn. The assumption of hydrostatic balance should be used with the awareness that the centrifugal force due to the relative motion, u^2/r , can be large in the strong equatorial jets noted on Saturn.

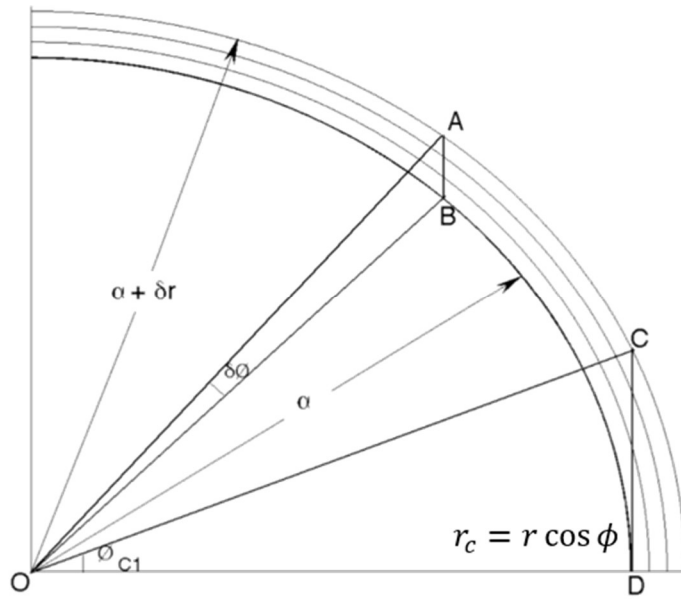


Figure 3.2. Schematic of the cylindrical routine for the general thermal wind equation. The latitude differential, $\partial\phi$, between the radial integration routine of the standard TWE and cylindrical integration routine of the general TWE is shown in this diagram. The critical latitude, ϕ_{c1} , in which the cylindrical path originating at top of the atmosphere will be tangential with the reference pressure level, which is used as the base boundary condition.

The other noteworthy difference between the two forms of the TWE is the use of different integration routines to estimate the zonal winds at different pressure levels with regards to a known wind at a fixed pressure level. For the standard TWE form, the integration is performed in the radial direction, ∂r , in order to obtain the zonal winds at different pressure levels. The division of ∂r by $\sin\phi$ yields an approximation of the cylindrical path length, ∂z , in (14). This approximation works at the mid- and high latitudes but breaks down close to the critical latitude, where the cylindrical path originating at the top

of the atmosphere becomes tangent to the equatorial surface. For a spherical body, the geometric construction shown in Figure 3.2 shows that the critical latitude, ϕ_{c1} , is given by

$$\cos \phi_{c1} = \frac{a}{a + \delta r} \Rightarrow \phi_{c1} = a \cos\left(\frac{a}{a + \delta r}\right), \quad (21)$$

where a is the reference radius of the planet and δr is the total thickness of the atmosphere being studied.

It is important to note that because the standard and general TWEs integrate along a different path, i.e., radial for the standard TWE versus cylindrical for the general form, the meridional temperature gradient, $\partial T / \partial \phi$. This gradient is different along the two paths and will lead to errors in the standard form. Figure 3.2 shows the angle $\delta \phi$ between the radial and cylindrical integration path. The error inherent in the standard TWE due to the different integration paths is increased as it moves into the equatorial region due to the increasing $\delta \phi$.

In order to derive the critical latitude at which the standard form of the TWE is unacceptable, an assumption about nature of the horizontal temperature gradient must be made – it can be assumed that the standard TWE is “sufficiently accurate”, as long as the horizontal excursion of the radial path of integration from the cylindrical integration

path is less than a specified amount, $(\delta\phi)_c$. Referencing Figure 3.2, the geometric solution yields the critical latitude of acceptability, ϕ_{c2} , which corresponds to the specified $(\delta\phi)_c$, as

$$a \delta\phi = \frac{\delta r}{\tan \phi} \Rightarrow \delta\phi = \frac{Hr}{a \tan \phi} < (\delta\phi)_c \Rightarrow |\phi_{c2}| > \tan^{-1} \left[\frac{\delta r}{a (\delta\phi)_c} \right]. \quad (22)$$

Equation (22) implies that the critical latitude of acceptability, ϕ_{c2} , is dependent upon the ratio of $\delta r/a$, the thickness of the atmosphere to the reference radius, and the specified $(\delta\phi)_c$. The error in the standard TWE becomes unacceptable at latitudes smaller than the critical latitude, ϕ_{c2} . With regards to (22), this equation only works for small values of $\delta\phi$, so that the approximation used in the equation applies.

For a thin atmosphere, the latitude excursion, $\delta\phi$, is not very small when approaching the equator. Therefore, a more precise expression, shown in (23), can be used to estimate $\delta\phi$ in the equatorial region.

$$\begin{aligned} (a + \delta r) \cos(\phi + \delta\phi) &= a \cos \phi \Rightarrow \frac{\cos(\phi + \delta\phi)}{\cos \phi} = \frac{a}{a + \delta r} \\ (a + \delta r) \cos(\phi + \delta\phi) &\Rightarrow \cos(\delta\phi) - \tan \phi \sin(\delta\phi) = \frac{a}{a + \delta r} \end{aligned} \quad (23)$$

However, the analytical solution of the excursion, $\delta\phi$, from (23) is not straightforward, but it is suitable for numerical evaluation of $\delta\phi$ with a known value of δr .

3.4 Validation and Application of the Thermal Wind Equations

After the derivation and comparison of the two forms of the TWE in Sections 3.2 and 3.3, respectively, the section will present their validation and application. The ability to validate both forms is courtesy of the plethora of Terrestrial data available for both large-scale wind and temperature fields on a global basis (Section 3.4.1). Their validation will set the stage for their continued use in atmospheric research on both Earth and other planets.

The application of the two forms of the TWE were also made to radiance data collected by the Composite Infrared Spectrometer (CIRS), which was aboard the Cassini mission to Saturn. The results from these two forms will be compared and discussed in Section 4.6.

Since Earth is our home planet, its atmosphere has been observed and studied in a most extensive manner, particularly when compared to other planets in our solar system and exoplanets. The scope and magnitude of these observations will allow for the opportunity to validate both forms of the TWE.

The validation of the TWEs will use daily-mean data from the reanalysis data set, NCEP2, having selected a random day, January 1, 2006. The NCEP2 data set has a spatial resolution of 2.5° , both in latitudinal and longitudinal direction, and was generated by the National Center for Environmental Protection – National Center for Atmospheric Research (NCEP-NCAR) (Kalnay et al., 1996, Kanamitsu et al., 2002). This meteorological data set is primarily generated using satellite-based observations.

For the validations of the two forms of the TWE, three variables, zonal wind, u , temperature, T , and geopotential height, Z , were used. These data are termed “type A variables”, which are considered to be of the highest data quality with the NCEP2 reanalysis data. The three-dimensional variables were zonally averaged and projected on to a latitude-altitude cross section for the two following reasons: 1) the analysis is examining large-scale motion, zonally averaging the data yields a good approximation of the large-scale processes, since it filters out the small-scale motions, and 2) in general, atmospheric scientists have a strong interest in the altitudinal and latitudinal variations.

The first step of the validation of the standard TWE will be the examination of the two assumptions that are the basis of this form. With regards to the hydrostatic balance approximation, the centrifugal force due to a parcel’s relative motion, u^2/r , is much

smaller than the effective gravity, $g_e = g + \Omega^2 r$. Additionally, the Coriolis force, $\Omega \times \mathbf{V}$, with the radial component in the same direction as gravity, can be shown through scalar analysis to be much smaller than the effective gravity. Since the additional forces that could make the hydrostatic balance assumption not applicable are of a small scale in comparison to the effective gravity, this allows for the use of hydrostatic balance in large-scale motions in the standard form of the TWE.

With regards to the assumption that there is geostrophic balance in the zonal winds, this requires that the pressure gradient and Coriolis forces are equal and opposite to each other. The zonal geostrophic wind (1) can be rewritten in the p coordinate system as

$$fu = \left(-\frac{g}{r}\right)\left(\frac{\partial Z}{\partial \phi}\right).$$

Therefore, the geopotential height, Z , to derive the geostrophic winds, which will then can be compared to the observed wind field from the NCEP2 data set.

Figure 3.3 shows the results from a comparison of the geostrophic wind calculations (upper frame) to the NCEP2 reanalysis zonally averaged winds (lower frame). This visualization shows positive agreement between these two factors, even across the equatorial zone. The scalar analysis of the large-scale motion implies that geostrophic balance only applies when the Rossby number, $R_o = U/fL$, is much smaller than 1. At a

latitude ϕ of 15° with the assumptions of $U = 10 \text{ m s}^{-1}$ and $L = 1000 \text{ km}$, $R_o = 0.3$. In this scenario, the Rossby number is not much less than 1, which suggests that the assumption that geostrophic balance does not hold in tropical regions, equatorward of 15° , from the traditional perspective of a small Rossby number. However, the results presented in Figure 3.3 shows that geostrophic balance assumption still applies when the Rossby number is not much smaller than 1, suggesting that either it is not a perfect criterion for the determination of geostrophic balance or the scales of the variables in the Rossby number should be re-evaluated.

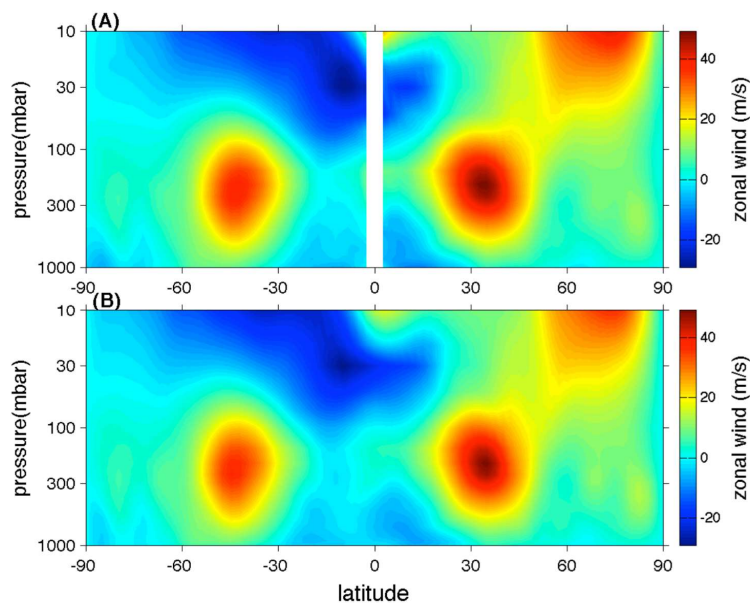


Figure 3.3. Comparison between the observed and geostrophic zonal winds, calculated from the geopotential height field. Panel A is the geostrophic zonal winds constructed from observed geopotential heights in the NCEP2 dataset. The gap in the equatorial zone in Panel A is due to the weakening of the geostrophic balance. Panel B shows the observed zonal winds from the NCEP2, contemporaneous to the geopotential heights of Panel A.

When applying the both forms of the TWE to planetary atmospheres, the derivation of conditions from the deep atmosphere occurs from above or the high-altitude conditions are derived from below. In order to test this methodology, integrations on the two forms were performed from the top and bottom of the atmosphere. Figure 3.4 shows the comparison between the observed wind field from the NCEP2 data set (Panel B), along with the results of the two integrations, based on the standard thermal wind equation. Panel A of Figure 3.4 was derived on the assumption that the zonal winds are known in the top layer of the atmosphere, while Panel C resulted from the bottom layer as the boundary condition.

This figure shows that there was good agreement between the standard TWE in the mid-to high latitudes, along with most of the equatorial region. These are on small areas of Figure 3.4 at the bottom of Panel A and the top of the Panel C, in the equatorial regions where there was more significant divergence between the observed and calculated zonal winds. These departures may have occurred because the errors associated with the approximation of the geostrophic balance around the equator accumulates along the integration routines.

Figure 3.5 is the same as Figure 3.4 except it compares observed zonal winds to the results from the integration of the general TWE. Figure 3.5 shows that the cylindrical integration associated with the general TWE performs well for the estimation of the zonal winds. Figure 3.6 presents a comparison of the general and standard forms of the TWE within the equatorial region. By contrasting these two forms of the TWE, it is noted that the general form of the TWE (Panels D, E, and F of Figure 3.6) outperforms the standard TWE (Panels A, B, and C of Figure 3.6).

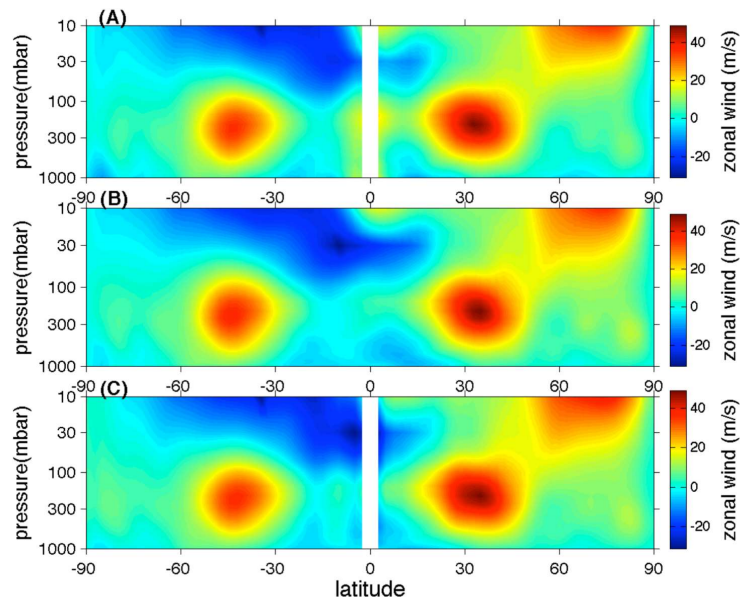


Figure 3.4. Comparison between the observed and derived zonal winds, using the standard form of the TWE. Panel B shows the observed zonal winds from the NCEP2 dataset. Panels A and C are derived zonal winds, which integrate the standard TWE from top and bottom atmospheric layers, respectively. The two integrations are based on NCEP2 temperature fields and the assumption of the zonal winds at the top and bottom layers are known and were based on the NCEP2 dataset.

Panel D of Figure 3.6 demonstrates that when integration of the general TWE is conducted from the top of the atmosphere that almost all of the equatorial region is included, which yields another advantage of this form. When the integration is performed from the bottom layer (Panel F of Figure 3.6), this shows that the latitude excursion between the two integration routines, i.e., radial with the standard TWE and cylindrical with the general TWE, is $\sim 5^\circ$ around the equator. This results in another reason that the general form of the TWE provides a better portrayal of the connection of the large-scale temperature and zonal wind fields.

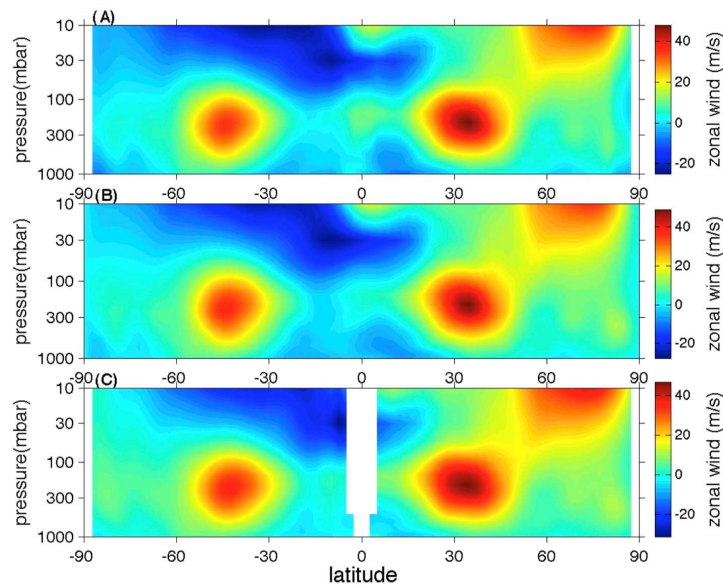


Figure 3.5. Comparison between the observed and derived zonal winds, using the general form of the TWE. Panel B shows the observed zonal winds from the NCEP2 dataset, same as Panel B in Figure 3.4. Panels A and C are derived zonal winds, based on the general TWE from top and bottom atmospheric layers, respectively. The integration from the top layer in Panel A covers almost all of the grid points in the equatorial region. The few missing points in Panel A are filled through a linear interpolation technique, using adjacent grid points. The integration from the bottom layer in Panel C has a latitude excursion $\sim 5^\circ$ when the integration reaches the top of the atmosphere.

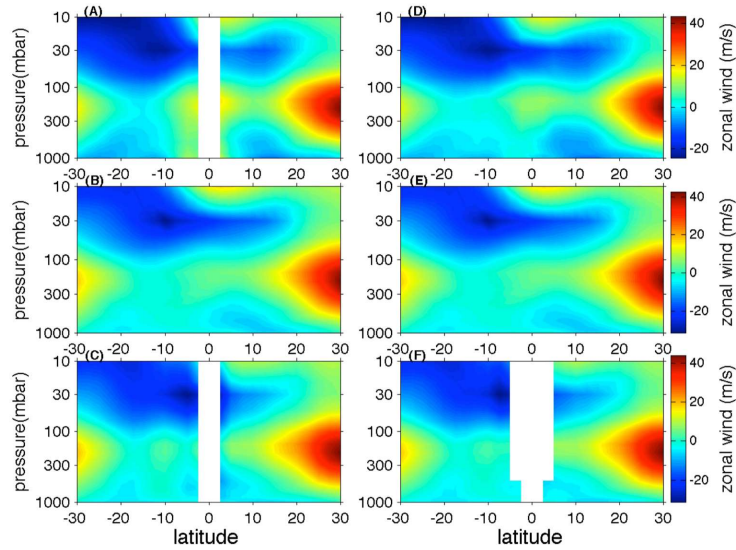


Figure 3.6. Comparison between the standard and general forms of the TWE for the equatorial region. The left column (Panels A, B, and C) is the same as Figure 3.4, while the right column (Panels D, E, and F) is the same as Figure 3.5; All six images are zoomed into the equatorial region.

It is noted that differences persist between the general form of the TWE and observed zonal winds suggesting that the general form is still an estimation of the relationship linking the temperature and zonal wind fields. This is potentially a result of the fact that the general form is based upon a simplified version of the primitive momentum equation. However, the general form still offers an improvement over the standard form, while it maintains most of the simplicity in the calculations.

Despite the general form of the TWE outperforming the standard form in the equatorial regions, this does not mean that the standard TWE will be replaced. For the mid- and

high latitudes, there are virtually no differences between the two forms because the geostrophic and hydrostatic approximations work so well in these regimes. Additionally, the latitude excursion between the cylindrical and radial integration routines is relatively small. In actuality, since the standard form is simpler than the general form and the radial integration routine is consistent with the observational grid, the standard TWE presents itself as a better choice. Additionally, the cylindrical integration scheme used in the general TWE does not work near the poles.

Given the known limitations of both forms, the analysis suggests that these two forms be used in tandem for the analysis of planetary atmospheres. The combination of the standard TWE in the mid- to high latitudes, along with the general form of the TWE in the equatorial regions is a recommended application of these equations.

This verification of the two forms of the TWE will also examine the inverse of what was just described in this section – the derivation of the temperature field from a known zonal wind field. (Only the standard form results are presented since the general form yielded almost the same results.) This analysis was based on the presumption that the vertical temperature structure is known at the equator and set as the boundary condition for the integration of the temperature fields. Figure 3.7 shows an alignment of the global-scale

temperature patterns with the observations from the NCEP2 data set (Panel A) when compared to the output from the integration of the thermal wind equation (Panel B). It is noted that Figure 3.7 does some discrepancies between the observations and derived values in the mid- to high latitudes, potentially resulting from the error associated with the thermal wind equation approximations and how they aggregate with the integration routines. Despite these errors, the general agreement shown in Figure 3.6 yields the suggestion that the derivation of the first-order estimation of the large-scale temperature field is possible based on the observed wind fields.

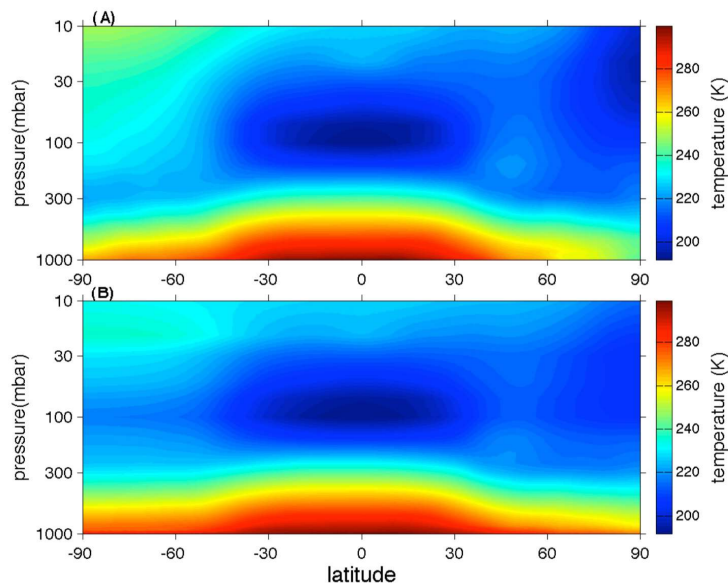


Figure 3.7. Comparison between the observed and derived temperature, based on the inverse application of the standard form of the TWE. Panel A shows the observed temperatures from the NCEP2 dataset. Panel B shows the results from the integration of the inverse application of the standard TWE by utilizing the zonal winds in the altitude-latitude cross-sections from the NCEP2 dataset with the vertical profile of the equatorial temperatures from the NCEP2 dataset used as a boundary condition.

3.5 Conclusions

This chapter revisited the assumptions and the subsequent derivation of the standard TWE. Additionally, the general TWE was derived using the simplified momentum equations, while placing an emphasis on this form's underlying physics. Both the standard and general forms of the TWE will be applied and verified with an NCEP2 reanalysis data set of Earth. The comparison of these results suggested that the general TWE, which does not include the approximations of geostrophic or hydrostatic balance, yields better results than the standard TWE in the equatorial region. It was also proposed that a combined application of the general TWE in the equatorial region, while the standard form is used elsewhere would provide a powerful tool for the exploration of planetary atmospheres. This new form of the TWE has previously been used in the examination of planetary atmospheres (e.g., Simon et al., 2015; Sánchez-Lavega et al., 2016; Fletcher et al., 2017).

The general TWE presents a constraint on the connection between the thermal and dynamical fields, along the cylindrical direction. Furthermore, this leads to further questions; primarily, can an independent constraint on this relationship between these two fields be obtained in a different direction? It would be possible to estimate the variations of the zonal winds in a direction, other than cylindrical, if such a constraint is

developed. From that derivation, a combination of thermal wind relationships in different directions would make it possible to estimate the entire zonal wind field in a latitude-altitude cross section from only one-point measurement of zonal winds. Further research into such a constraint of the relationship between the thermal and dynamical fields continues to be conducted.

Chapter 4 (Task 2): Spatiotemporal Variations of Saturn's Zonal winds at & above the visible cloud level

In order to expand our understanding of the vertical structure of Saturn's atmosphere, an analysis of Cassini CIRS and ISS data was conducted. By combining these two data sets and applying the forms of the thermal wind equation that were developed in Chapter 3, this will provide insight into the vertical structure of the atmosphere from the upper troposphere outward into the stratosphere.

In this chapter, the Imaging Science Subsystem (ISS) onboard the Cassini spacecraft and the requisite data processing methodology will be introduced. In previous research, the multi-filter (i.e., multi-wavelength) ISS images have been used to measure the zonal winds from the tropopause downward into the upper portions of the troposphere. In this analysis, one of the results was the determination of the zonal winds at the visible cloud level, ~300 to 500 mbar. This specific output is used as a boundary condition for the investigation of the thermal winds, which are based on the CIRS-retrieved temperatures and the general form of the TWE, developed in Chapter 3.

The next section in Chapter 4 will present information about the Composite Infrared Spectrometer (CIRS), which was used to collect radiance data during the Cassini mission.

This observed spectra data is used to determine atmospheric temperature fields above the visible cloud layer in the troposphere. The derived CIRS temperature data will be applied to the general TWE, developed in Chapter 3, and use the ISS-measured zonal winds as a boundary condition. The results of this endeavor is an improved understanding of the vertical structure of the zonal winds above the visible clouds.

4.1. Data and Processing Methodology – ISS Output

The Imaging Science Subsystem (ISS) consisted of two cameras, a narrow-angle camera (NAC) and a wide-angle camera (WAC), displayed in Figure 4.1. While the NAC yielded high-resolution images even at far distances, the WAC was designed to provide simultaneous global views, required for image navigation. In tandem, the ISS provided the ability to generate hemispheric mosaics, which could even extend to a near-global coverage (Del Genio & Barbara, 2012).

The NAC was a reflecting telescope with a 2-meter focal length and a square FOV 0.35° across. While the WAC was also a reflecting telescope, it has a 0.2-meter focal length, and the FOV is 3.5° across. Each camera used a charged couple device (CCD) detector consisting of a 1024-square array of pixels, each $12\ \mu\text{m}$ per side (Porco et al., 2004).

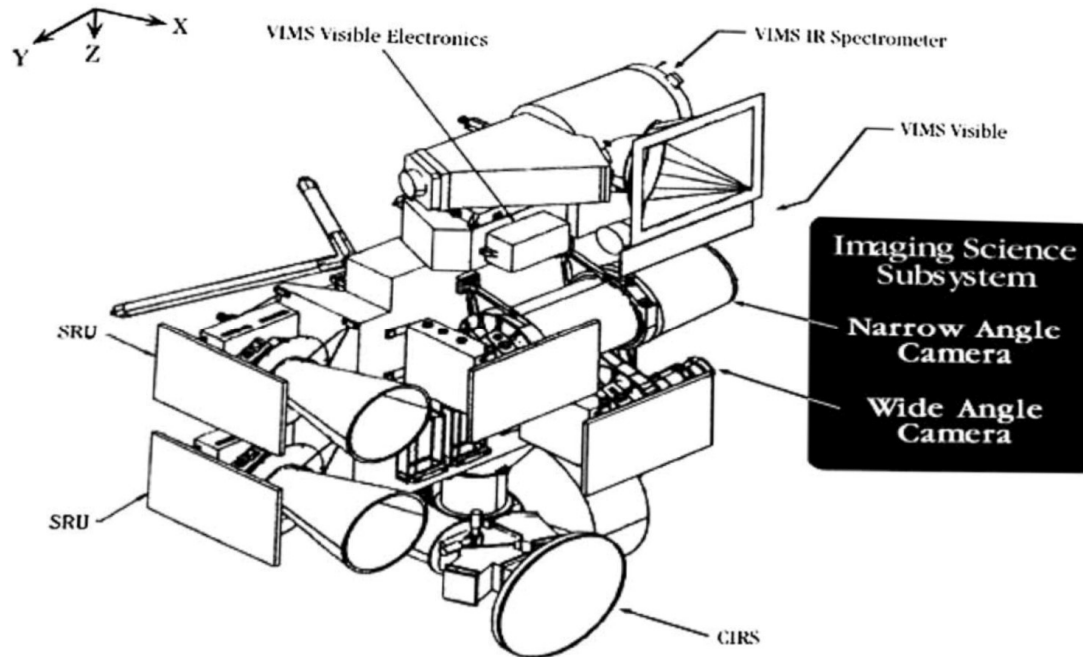


Figure 4.1. Schematic illustrating the location of the narrow- and wide-angle cameras on the ISS. The VIMS and CIRS are also shown on this diagram, along with the spacecraft coordinate system, in the upper left of the diagram (Porco et al., 2004).

4.1.1 Data – ISS Images

Both cameras are equipped with a series of narrow band filters. There are twenty-four filters on the NAC, while there were eighteen on the WAC. Of interest to this research were the bands listed in Table 4.1.

The selection of these particular wavelengths in both the design of the ISS along with the choice of data to analyze was based on its ability to provide insight into the vertical structure of Saturn and also to examine spatiotemporal trends in zonal flow at multiple

levels. Images developed from the ISS data are used to determine winds at different pressure levels by tracking visible clouds at each level.

In summary, the various ISS filters used in the collection of atmospheric data provide a vertical cross-section, represented in Figure 4.2. The combination of the ISS images with the CIRS images aided in furthering our understanding of the vertical structure of the Saturnian atmosphere.

Table 4.1. Data collected through these ISS filters was used to track clouds and establish the associated zonal wind speed through the upper troposphere. Sorted by depth examined in Saturn’s atmosphere from top to bottom (García-Melendo et al., 2011, Li et al. 2011).

	Wavelength	Depth examined
Methane band: MT3	889 nm – NAC 890 nm – WAC	50-60 mbar – Tropopause
Methane band: MT2	727 nm – NAC 728 nm – WAC	100 mbar – Lower tropopause
Continuum band: CB2	750 nm – NAC 752 nm – WAC	300-500 mbar – Upper troposphere
Continuum band: CB3	938 nm – NAC 939 nm – WAC	300-500 mbar – Upper troposphere

From the collection of the raw sensor data by Cassini’s ISS to the determination of the zonal winds, there are several steps of data processing and analysis that must be completed. The techniques of data processing (Del Genio et al., 2007; Porco et al., 2004; Sayanagi et al., 2013; Vasavada et al., 2006), navigation and fitting (Del Genio et al., 2007; Antuñano et al., 2015), the methods for estimating the zonal winds (Antuñano et al., 2015;

Choi et al., 2009; Del Genio et al., 2007; Del Genio and Barbara, 2012; Li et al., 2011, 2016; Limaye, 1986; Salyk et al., 2006) and the subsequent uncertainty estimates (Antuñano et al., 2015, 2018; Del Genio and Barbara, 2012; Del Genio et al., 2007; Li et al., 2011; Sánchez-Lavega, et al., 2014) were used as the baseline for this analysis.

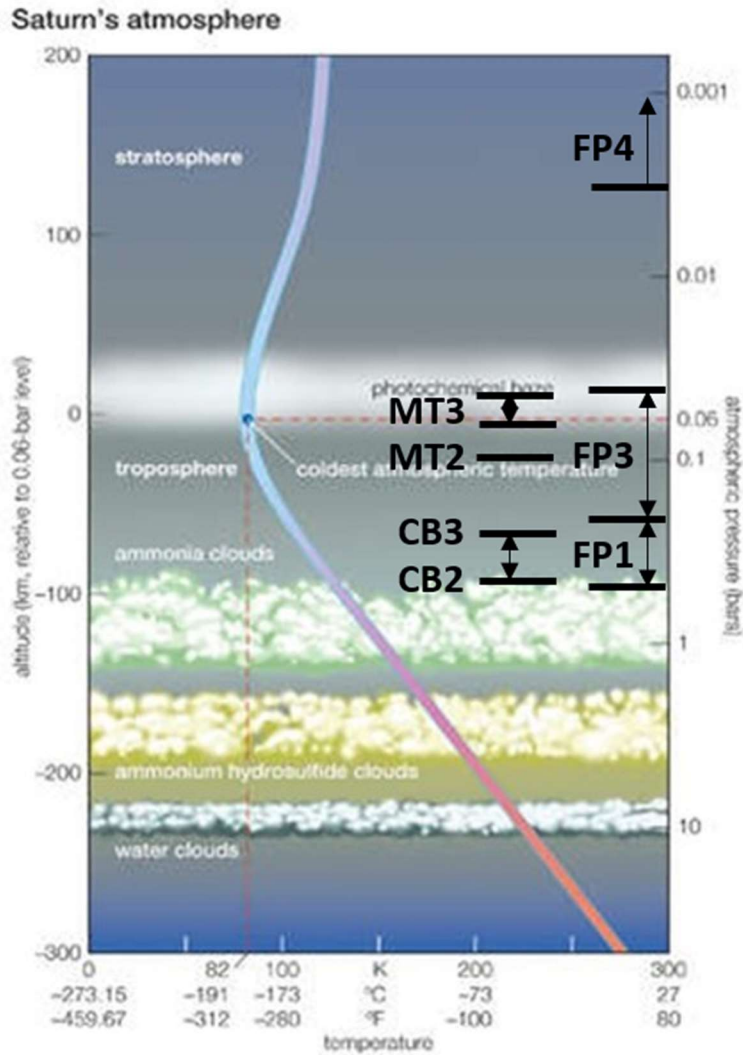


Figure 4.2. Cross-section of Saturn's atmosphere, noted with pressure levels observed by the CIRS and ISS. Specific observation pressure levels are listed in Tables 4.1 and 4.2 (Adapted from Hubbard, Buratti, & Marley, 2020).

4.1.2 Processing Methodology – ISS Images

4.1.2.1 Data Processing

ISS data cubes were accessed from the NASA Planetary Data System (PDS) Imaging Node and similar to the VIMS data processing (Section 5.1.2), the analysis was limited to data that either (1) attempted feature tracking by repeatedly scanning the same absolute frame, relative to the System III longitude, or (2) gathered a full-disk mosaic which observed the overall status of the Saturn's atmosphere over a full Saturnian day.

The image processing required for the ISS data, i.e., calibration and removal of solar illumination is described in detail in Del Genio et al. (2007); Porco et al. (2004), and Vasavada et al. (2006). A summary of these steps is provided forthwith.

The ISS images were processed into maps prior to analysis using the camera geometric model and the photometric calibration software, Cassini ISS CALibration, (CISSCAL), Version 3.8 (Del Genio et al., 2007; Porco et al., 2004). This program ingests the raw images, subtracts the dark current, i.e., the electrical current generated in the detector when no photons are entering the detector, along with the bias. CISSCAL then divides by a flat field, which is a standard procedure used to account for variations in the pixel-to-pixel sensitivity of the sensor, as well as correcting for non-linearity and for the

existence of a haze on the narrow FOV camera. The program finally converts this data to I/F , the calibrated reflectance of the surface (Cheng & Domingue, 2000), where:

I – Light intensity scattered into a particular observing direction ($\text{erg cm}^{-2} \text{s}^{-1} \text{sr}^{-1}$),

πF – Incident flux on the surface ($\text{erg cm}^{-2} \text{s}^{-1}$).

The removal of the solar illumination was required because scattering yielded by stratospheric haze causes residual large-scale variations in the output (Sayanagi et al., 2013). The removal of this dynamic range allows for emphasis of contrasts within cloud features (Vasavada et al., 2006).

There are two techniques possible for the removal of solar illumination: use of the Minnaert function (Minnaert, 1941) or the use of a high-pass filter, which was proposed in Vasavada et al. (2006). This photometric correction is designed to remove the dynamic range that occurs due to illumination variations. This technique is applied to emphasize the contrasts between clouds. Individual cloud features on Saturn may have a lower intrinsic contrast, due to haze through upper levels of the atmosphere. Therefore, these clouds require highly accurate illumination corrections, so as to more accurately track them during the zonal wind estimation process. Rather than using the Minnaert function,

which does not properly account for solar illumination that is scattered by Saturn's rings, the analysis applied the high-pass filter methodology (Vasavada et al., 2006).

4.1.2.2 Navigation and Fitting

The navigation and fitting of the ISS data was critical for the calculation of zonal winds through the troposphere and across the tropopause, as they are directly impacted by the correct positioning and time tagging of the individual image frames.

The high-resolution images collected by the NAC were navigated using the Modular Image and Navigation Software (MINAS), as originally described in Del Genio et al. (2007). The program reads the CISSCAL output, which was detailed in Section 4.1.2.1, and also uses near-simultaneous WAC images, which is scanned to locate the limb with sub-pixel precision. Predicted pointing, which is extracted from the binary C-kernels in the PDS data set, is matched with a linear least-squares regression to the scanned curve. The last step for the navigation and fitting processing is the application of a small boresight correction, which accounts for a known offset between the NAC and the WAC.

Similar to the VIMS images, the frames were projected into a simple cylindrical projection when equatorward of latitude 60° (Del Genio et al., 2007). When poleward of latitude 60° ,

a polar projection scheme using an azimuthal equidistant projection (Antuñano et al., 2015).

4.1.2.3 Estimations and Errors of Zonal Winds

The focus of this dissertation is to provide an increased understanding of Saturn's tropospheric wind field, along with those of the tropopause, over the duration of the Cassini mission. Given a lack of *in situ* measurements, the ISS sensor data was used to observe cloud fields across the tropopause and into the upper troposphere. This data was analyzed through the technique outlined below in a matter to extract planetary-scale zonal winds.

The examination of the ISS data extended the work started by Del Genio et al. (2007) to now include data collected during the balances of Cassini's Prime Mission (after April 1, 2007) and through the entirety of the Equinox and Solstice Missions, along with the Grand Finale.

Cloud tracking analysis was performed with a methodology similar to Del Genio et al. (2007), Limaye (1986), and Salyk et al. (2006). The supposition was made that clouds can be treated as passive tracers of atmospheric mass motion. This tracking analysis was

handled with two techniques: automated and manual tracking. The majority of the zonal wind speed measurements were conducted with automated tracking technique, which utilizes algorithms to track the cloud features over a series of images (Limaye, 1986). Using MATLAB code developed within our research group, along with work performed in conjunction with the Space Science and Engineering Center of the University of Wisconsin, the data sets were searched to determine the maximum cross-correlation between the images. By determining the longitudinal displacement of the pixels and the time elapsed between the images, the zonal wind speeds were derived. In some cases, manual cloud tracking is required to be implemented. This process was based on visually identifying a cloud feature and then tracking the feature in different images at different times. By determining the distance traveled and the time between the images, the zonal wind speed at that particular latitude can be determined.

Typically, these two methods are used in tandem to determine Saturn's zonal winds. Del Genio et al. (2007) discussed that the advantage of the automated tracking method was that it allowed for an efficient survey of observations and that the features can be objectively selected. These factors provide higher sample sizes that would be possible via manual tracking. Conversely, areas with linear albedo patterns highlight the weakness of an automated tracking methodology in it is susceptible to spurious pattern matching.

Based on the analysis presented in Del Genio and Barbara (2012), when the maximum correlation coefficient was less than 0.5, the wind vectors were rejected. Similarly, wind vectors which exceeded the one standard deviation of the mean at that specific latitude were excluded from the analysis. These criteria eliminated spurious vectors that could be associated with changes in the cloud morphology and any brightness gradients that were not removed via the image processing.

For the ISS data, the primary sources of uncertainty in the zonal wind speed estimates were navigation error, changes in the shape of the clouds, uncertainty in Saturn's rotation period (as detailed in Sections 2.2.2.3 and 3.1), and pixel resolution (Del Genio et al., 2007). Navigation error can result from uncertainty in the geographical location of the cloud features and the absolute location of the spacecraft (Choi et al., 2009, Li et al., 2011). While the errors of the absolute location can be on the order of ~100-200 km, the relative uncertainty in location between pixels is small, but nonzero. Therefore, the derived measurements of lengths and velocities used in this research will not significantly degrade the accuracy of this analysis.

Li et al. (2011) provided a detailed analysis of the uncertainty of zonal wind speed estimates, based on pixel resolution issues. This study examined the contributions of three

sources: 1) the standard deviation of multiple wind measurements within a 1° latitude bin, 2) uncertainty associated with the ISS WAC and NAC, and 3) uncertainty related to the locating of the cloud/haze features in the images.

Item 1 is on the order of a few meters per second, while the uncertainty associated with Items 2 and 3 were 3.8 m s⁻¹ and 5.2 m s⁻¹ for the NAC and WAC, respectively (Li et al., 2011). Estimates detailed in Antuñaño et al. (2015) used a similar technique to Li et al. (2011) placed errors in the 5 to 10 m s⁻¹ range.

For the polar regions, the methodologies described in Sánchez-Lavega et al. (2014) and Antuñaño et al. (2015) were applied: Cloud tracking with image pairs that are separated by one planetary rotation (~10.5 hours) and two-dimensional correlation analysis using polar projected images. The correlation algorithm allows for the manual validation of the identifications, which becomes important in polar regions since cloud morphology can undergo rapid changes (Antuñaño et al., 2018). Rarely, the manual cloud technique described above can be applied; generally when there were only a few wind vectors in each images (Antuñaño et al., 2015).

4.2 Previous Research – ISS

Historically, a more thorough examination of the ISS data has been conducted than previously applied to the VIMS data from aboard the Cassini. This is due to the fact that the altitudes at which the ISS observes produce higher resolution images within the troposphere and across the tropopause. Therefore, any studies conducted with ISS data, e.g., cloud morphologies, synoptic-scale storm patterns, or the topic germane to this dissertation, zonal wind speeds, would yield better defined cloud images along with a lower level of measurement uncertainty.

The continuum band images recorded by Cassini's ISS CB3 have been used to explore tropospheric zonal winds at 300 to 500 mbar, which is the level of the top visible clouds, also referred to as ammonia clouds (Figures 2.1 and 4.2). Additionally, the methane band images gathered by the ISS are used to examine the zonal wind speeds across the tropopause (~10 to 60 mbar) and into the upper troposphere (~100 mbar), (e.g., Baines et al., 2005; Del Genio & Barbara, 2012; Dyudina et al., 2008, 2009; García-Melendo et al., 2007, 2010, 2011, 2013; Li et al., 2011; Porco et al., 2005; Sánchez-Lavega et al., 2007, 2011, 2014, 2016; Sanz-Requena et al., 2018; and Sayanagi et al., 2013, 2017).

Porco et al. (2005) was the first publication to review data from the ISS, which was collected during Cassini's final approach to Saturn, from February through May 2004. Additionally, the ISS imagery collected during Cassini's first orbit of Saturn during September 2004 was reviewed. During the period of this study, it was summer in the Southern Hemisphere; this allowed for complete observations of the Southern Hemisphere, while the Northern Hemisphere was partially obscured by the ring's shadows.

The results established in Porco et al. (2005), which examined data collected through both methane and continuum band filters, compared favorably to measurements collected during the Voyager missions along with data collected by the HST. It was noted that the Southern Hemisphere zonal winds, poleward of 15°S, were similar in magnitude to previous measurements and favorably aligned in the location of the local maxima and minima. Additionally, this analysis confirmed the Cassini ISS data was in line with the HST and Voyager-era data in concluding that equatorial zonal winds were subjected to VWS and also confirmed that the vertical shear subsided deeper into the troposphere.

Sánchez-Lavega et al. (2007) used ISS data from all four filters, CB2, CB3, MT2, and MT3, to examine the upper levels of the troposphere, extending from 8°N to 20°S. This research

examined zonal wind speeds through the depth of the atmosphere in the equatorial region from May 2004 into February 2005. Additionally, radiative transfer modeling concluded that there are two detached aerosol layers in the tropical region. The uppermost layer of haze lies in the tropopause, between ~20 to 40 mbar, while the other layer ranges from just below the tropopause (~50 mbar) to much deeper in the troposphere (~1000 to 1400 mbar), at the base of the ammonia cloud layer.

For the examination of the zonal winds, Sánchez-Lavega et al. (2007) studied the individual clouds, extending from about the 50-mbar level down to 700 mbar. During the period of the study, the 50-mbar zonal winds were 265 m s^{-1} and were stronger at the 700-mbar level, 365 m s^{-1} . It was noted that these measurements were less than similar values by the Voyager missions (1980–1981). These results pointed to two different possibilities: The Voyager missions examined even deeper into the troposphere than originally thought or that the zonal winds slowed during this 24-year period.

Dyudina et al. (2008) used ISS data to provide insight into the dynamics of Saturn's south polar vortex (SPV). While the SPV is similar to others seen in the solar system, it is also distinct. The visualization from the ISS data showed it to be similar to the eye of a tropical cyclone on Earth. There was a double eye wall and a shadow cast by the eye wall,

extending across the eye. The clouds within the eye were in the upper troposphere at the 300- to 500-mbar level, while the upper troposphere (~100 mbar) was nearly cloud-free. The height of the outer eye wall was estimated at 40 ± 20 km, while the inner eye wall height was estimated at 70 ± 30 km. Through the individual cloud elements, the peak zonal velocity was estimated to be 150 ± 20 m s⁻¹.

Dyudina et al. (2009) extended the work published in Dyudina et al. (2008) by adding in data from both the CIRS and VIMS. The results published in this article as related to the VIMS are given in Section 2.2. The ISS data showed that the 300- to 500-mbar zonal wind speeds within the SPV, near 87°S, were consistent with those from the VIMS images deeper in the troposphere. This result implies that there is minimal VWS within the vortex structure, which is in line with Baines et al. (2005).

Additionally, the eye wall clouds were noted at the same locations on both the ISS and VIMS data. The conclusion reached in Dyudina et al. (2009) was that the VIMS and ISS were either detecting at the same altitude, which is a low probability outcome, or that the clouds extended vertically. This latter conclusion correlates with the previously stated inference there is negligible VWS within the tropospheric levels of the SPV.

García-Melendo et al. (2010) examined the three-dimensional nature of a strong and narrow jet, which lies embedded within a broader equatorial jet, using a non-homogeneous sampling of ISS data from September 2004 through January 2009. The results showed the narrow jet extended from the upper levels of the troposphere (~500 mbar) with zonal wind speeds of 390 m s^{-1} , through the tropopause (~50 mbar) where zonal wind speed increased to 430 m s^{-1} . From the tropopause, the jet oscillates through the vertical and into the stratosphere; at 10 mbar, winds were 330 m s^{-1} , while at the 1-mbar level, the zonal wind speed increased, at 500 m s^{-1} . The mapping of this narrow jet was the first research to indicate the presence of a stratospheric jet. It should be noted that the additional research has shown the seasonal variations that were suggested in their conclusions.

García-Melendo et al. (2011) examined the entirety of Cassini ISS data from September 2004 through June 2009 using the four primary filters, CB2, CB3, MT2, and MT3. The data set compiled by the ISS using these filters yielded zonal winds extending from the tropopause (~50 mbar) into the troposphere (~500 mbar). This research showed in the higher latitudes, higher than 40°N/S , the intensity and location of jet wind structure generally remained unchanged through the period of the data review. Coupled with data from Voyager and the HST, this represents a full Saturnian year with general continuity

in these higher latitude jets. The implication of this result is that despite the eccentricity of the orbit and the seasonal changes, the solar insolation cycle does not impact tropospheric winds.

While the equatorial jet, defined in this research (García-Melendo et al., 2011) as ranging from 35° N to 35° S, is a permanent feature of the planet's circulation pattern, it did exhibit high levels of temporal variability during the period of study. The temporal variations shown in zonal winds and the VWS through the upper levels of the troposphere and into the tropopause were consistent with an estimation of the thermal wind effect, along with radiative transfer modeling.

Additionally, García-Melendo et al. (2011) noted that within the equatorial jet, there were two regions with a "velocity inversion" that was a persistent feature through the examined Cassini data. Specifically, the winds near the tropopause (~50 to 100 mbar) were $\sim 30 \text{ m s}^{-1}$ greater than the winds deeper in the troposphere (~350 to 500 mbar). At the time of this research's publication, there were uncertainties as to whether variations in the seasonal insolation cycle would impact this phenomenon. It is a goal of this dissertation to establish if there are any long-term impacts of this pattern, or the strong and narrow equatorial jet that was discussed in García-Melendo et al. (2010).

Li et al. (2011) conducted analysis of the ISS and CIRS data sets from 2004 through 2008 to search for the occurrence of the Quasi-Quadrennial Oscillation (QOO) on Saturn. This research showed that the 500-mbar winds (ISS CB3 data) remained fairly consistent through the five-year cycle. However, the 60-mbar winds (ISS MT3 data), which tracked a hydrocarbon haze in the tropopause, showed an increase in the zonal wind speeds during this period of study. In combination with the CIRS data examined in this research, since the acceleration in the stratosphere was greater than that noted at the tropopause, the authors concluded that a semi-annual equatorial oscillation, the QOO, is dampened as it progresses downward.

The analysis conducted in Del Genio and Barbara (2012) showed the upper tropospheric winds (~350 to 500 mbar) demonstrated little change between 2005 and 2007 in the Southern Hemisphere. This research placed more emphasis on the zonal winds in the lower sections of the tropopause, particularly the equatorial region of the Northern Hemisphere. For the easterly jet cores, the 100-mbar winds were $\sim 10 \text{ m s}^{-1}$ lower than the upper tropospheric zonal winds. However, on the flanks of these cores, where they slow to transition to a westerly jet, the 100-mbar winds were ~ 5 to 8 m s^{-1} stronger than the upper tropospheric zonal winds along the same latitude. These results were consistent

with previous research, as presented in Porco et al. (2005) and García-Melendo et al. (2011).

While convective storms are noted on terrestrial planets, they have also been observed on the gas giants. Sayanagi et al. (2013) documented the first storms to be captured by Cassini, an episode that started in December 2010, continuing into August 2011. This research examined images captured with ISS's wide-angle camera using the continuum band filter, CB2 (750 nm), along with the methane filters, MT2 (727 nm) and MT3 (889 nm). The research provided an overview of the storm's genesis and evolution over time and culminated in its dissipation. Additionally, the analysis presented a comparison of the zonal wind profiles from the data captured by the CB2 filter, i.e., clouds at the top of the tropospheric cloud deck. Additional details on this specific research will be shared in Chapter 6.

Sánchez-Lavega, et al. (2014) examined ISS data from the CB2 filter from three different periods, November – December 2008, January 2009, along with November 2012. The earliest two sets were gathered during the Equinox Mission, though August 2009 equinox has not occurred yet. The 2012 data set was collected during the Solstice Mission, as Saturn was moving towards NH summer.

These three data sets were used to determine the wind profile within the NH eastward polar jet, which is collocated with the circumpolar hexagonal pattern near 75°N. With the CB2 data, the wind measurements are approximated to be in the upper troposphere, near 300 to 500 mbar (Sánchez-Lavega, et al., 2014). These heights are consistent with the pressure levels examined from Voyager data (García-Melendo et al., 2011).

Similarly, the results presented in Sánchez-Lavega et al. (2014) were consistent with previous work that demonstrated the North Pole's hexagonal storm encompasses a narrow and intense easterly jet. Figure 4.3 shows the comparison from the analysis the 2008 through 2012 data, compared to the Voyager data from 1980 – 1981. The comparison of the data sets, despite being over 25 years apart, indicate that there was no substantial change of the jet's intensity, shape, or associated atmospheric parameters, despite variation in incoming insolation at these high latitudes. The consistency in strength and structure of the NH polar jet and the surrounding hexagon over a Kronian year, despite the seasonal changes, suggests that the driving mechanism for this atmospheric structure is deep in the atmosphere. This theory is consistent with other research conducted on Saturn's tropospheric jet structure (García-Melendo et al., 2007, 2013; Sánchez-Lavega et al., 2011). Further analysis of this NH hexagonal storm and associated polar jet will be presented in Chapter 5.

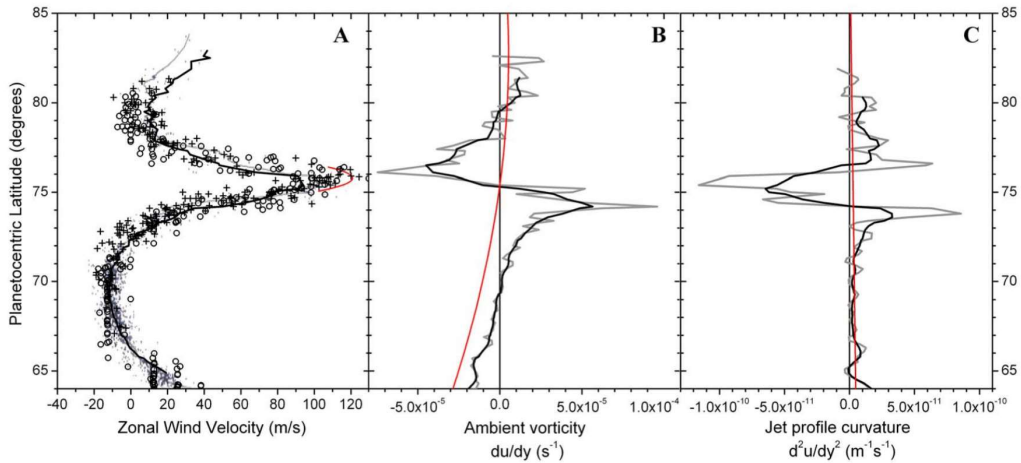


Figure 4.3 Zonal wind velocity and associated atmospheric parameters observed in vicinity of the hexagon polar jet from 2008-2009 and 2012 using Cassini ISS images. Panel A is the zonal wind profile, extending from $\sim 65^{\circ}\text{N}$ to $\sim 83^{\circ}\text{N}$. The dark continuous line was obtained from a 1-D correlation methodology with data ranging from November 29 to December 1, 2008. The crosses were derived from the cloud tracking technique with data from January 2-3, 2009. The circles were attained through a 2-D correlation scheme with data from November 28, 2012. The gray lines and small dots are from the Voyager 1 and 2 missions, respectively (Godfrey, 1988). The red parabolic curve represents the peak jet intensity, obtained from individual cloud track. Panel B shows the ambient vorticity profile as the light gray line, while the dark gray represents the profile smoothed with 2° resolution. The planetary vorticity, βy , is shown as the red line. Panel C displays the profile of the jet's curvature with the same smoothing and coloration as used on Panel B. Similarly, the planetary vorticity gradient, β , is represented by the red line (Sánchez-Lavega et al., 2014).

Sánchez-Lavega et al. (2016) examined zonal wind data collected by the HST in 2014 and 2015, along with wind speeds observed by the ISS during April, September, and October 2014. In addition, this research included previously published ISS and VIMS results, ranging from 2004 through 2009. Through the inclusion of this additional data, their research sought to establish spatiotemporal zonal wind trends through the troposphere.

The results presented in Sánchez-Lavega et al. (2016) showed that the central equatorial jet not only persisted, but also experienced meridional broadening during the period of 2004-2009 and again in the 2014-2015 time frame.

Sayanagi et al. (2017) examined ISS imagery from 2012, focusing on the polar vortices. In August 2009, Saturn's North Pole was illuminated by sunlight for the first time since 1994, nearly ten years before Cassini's arrival. However, since Cassini was in an equatorial orbit, the viewing geometry was poor until late 2012. The research presented the results of zonal wind measurements detected within the north polar vortex (NPV) with the CB2 filter, which detects to the ~300- to 500-mbar levels. Additionally, this analysis compared the NPV to the SPV results, which were prepared in association with this report.

In the course of completing their analysis, Sayanagi et al. (2017) examined 274,822 wind vectors, covering a zonal extent from 88.5° N to 90° N. The results showed the zonal wind speeds slowly declined between 88.5° N (~160-165 m s⁻¹) to 89.3° N (~120-125 m s⁻¹). Poleward of 89.3° N, the wind speeds declined more rapidly and approached zero at the North Pole. Additionally, this analysis calculated the relative vorticity within the NPV. The relative vorticity was shown to be entirely cyclonic, which is consistent with the zonal

wind speed structure. The relative vorticity peaked around the North Pole at $\sim 6 \times 10^{-4} \text{ s}^{-1}$, which is approximately twice the planetary vorticity.

In comparing their results to the SPV observations, Sayanagi et al. (2017) scrutinized the cloud morphology and motions within the double-wall structure around the “eye” of the SPV using both the continuum and methane band filters. Similar to the NPV, the relative vorticity was estimated to be $\sim 2.8 \times 10^{-4} \text{ s}^{-1}$, which is relatively close to the planetary vorticity.

Sanz-Requena et al. (2018) examined the hexagon wave and found that just equatorward of the region, the base of the tropospheric haze was at $900 \pm 200 \text{ mbar}$, which is the lowest level found in non-polar regions. Within the wave, the base was estimated to be $800 \pm 200 \text{ mbar}$, while in the polar vortex, the pressure altitude was lower, reaching $1000 \pm 300 \text{ mbar}$. These findings were consistent with the findings of Sánchez-Lavega et al. (2016), which posited that the area within the polar vortex is a region of subsidence, containing deeper clouds and fewer particles. While not specifically noted in Sanz-Requena et al. (2018), these findings also indicate upwelling within the hexagon wave. Additionally, consistent with the findings above, the research indicated that the hexagon wave, along

with its embedded jet stream, is a boundary between the inner and outer regions with different aerosol properties noted in the two areas.

Similar to Sanz-Requena et al. (2018), the work presented in Antuñano et al. (2018) compared zonal wind speeds across the NPV, including the hexagon wave. This aspect of their work was completed in the context of comparing cloud morphology variability to possible changes in the zonal wind speeds within the NPV. In comparing results from Antuñano et al. (2015), Sanz-Requena et al. (2018) noted that while there were changes in the cloud morphology, both the zonal and meridional winds in the polar region ($\sim 88.5^\circ$ N) were unchanged, with the zonal winds estimated to be $145 \pm 18 \text{ m s}^{-1}$. Additionally, these comparisons examined the relative vorticity, which did not significantly change, while the divergence within the NPV was essentially zero.

4.3 ISS Analysis: Zonal Winds at & above the Visible Cloud Level

Since this dissertation work highlights the spatiotemporal variation of Saturn's atmosphere, an examination of Northern Hemisphere upper tropospheric winds from 2004 through 2015 using data acquired with the ISS CB3 and MT3 filters was conducted. The CB3 filter is used for upper tropospheric winds at the ~ 300 - to 500-mbar level, while the MT3 filter examines zonal winds across the lower part of the tropopause, ~ 50 mbar.

During the early portions of the Cassini mission, from 2004 into 2008, it was the middle to latter part of the SH summer and the ISS data was used to examine its equatorial region, as the ring's shadow obscured NH observations. Three techniques were used to establish the zonal winds through this period: for the 2004, both manual and automated tracking methods were used with the ISS data; for 2005, the thermal wind equation was applied to CIRS data – a technique that is elaborated on later in Chapter 4; and finally, in 2008, all three procedures were used in a combined ISS and CIRS dataset.

For this five-year period, the zonal winds through the lower extent of the tropopause, ~50 mbar, increased ~30 m s⁻¹ between 2004 and 2008 (Figure 4.4, Panel A). With the increase in the zonal wind velocity shown to be greater than the error bars, this demonstrates that this intensification was indeed relevant and could not be relegated to noise. Additionally, the location of peak velocity shifted equatorward from ~13°S to ~10°S.

Panel B of Figure 4.4 shows that the deeper tropospheric winds remained relatively unchanged through this five-year time span. This pattern aligns with earlier research (Del Genio and Barbara, 2012; García-Melendo et al., 2010, 2011; Li et al., 2011), where the deeper troposphere is less susceptible to spatiotemporal variations occurring through the same season.

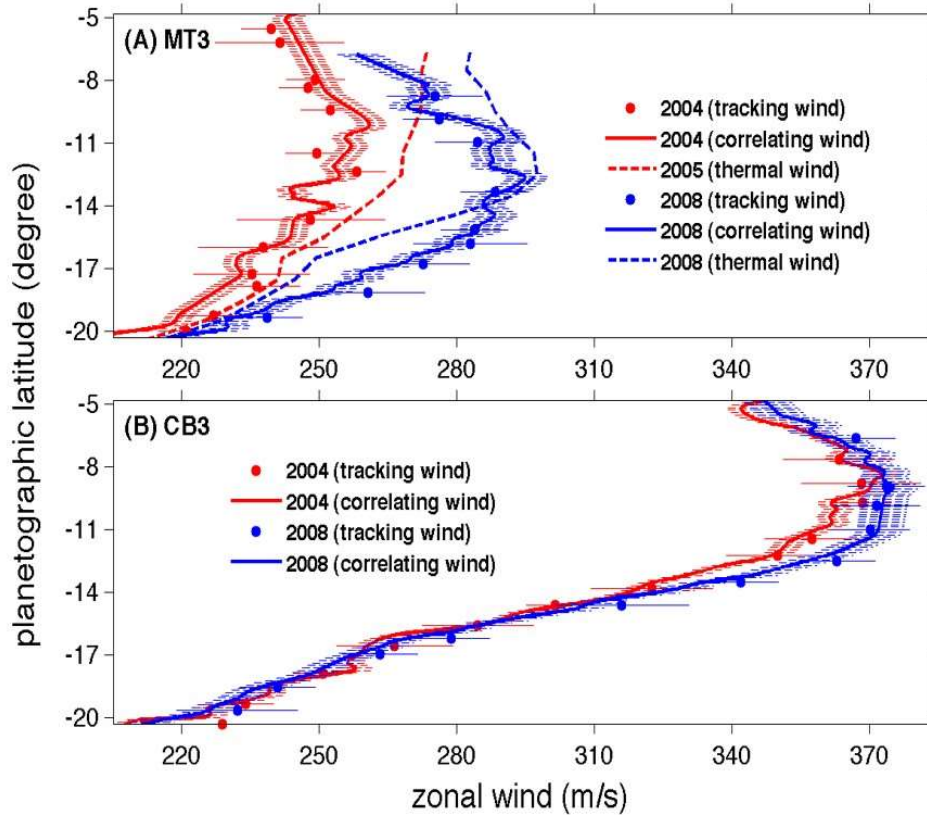


Figure 4.4. Comparison of the SH equatorial winds using the ISS MT3 and CB3 filters between 2004-2005 and 2008. Panel A illustrated data collected by the MT3 filter, which are from the lower part of the tropopause, ~50 mbar. These data were derived using three different techniques to calculate the zonal winds: cloud tracking (dots), 1-D correlation (solid lines), and thermal wind calculations using CIRS data (dashed lines). This data shows that between 2004-2005 and 2008 that the zonal winds in the lower tropopause increased, while the SH was in its summer season. Panel B shows zonal wind data collected by the CB3 filter, which are from the upper troposphere (~300 to 500 mbar), using the same display scheme as Panel A. These data show that the deeper winds remained relatively steady over time, to within calculated error bands.

Additionally, the ISS CB3 observations from 2009 through 2015 were examined; however, this data was for the equatorial region of the Northern Hemisphere, extending poleward to 30°N. The analysis of data collected by the continuum-band filter showed an acceleration during this time in the equatorial region, south of 10°N (Figure 4.5), in the

deeper troposphere, i.e. ~300 to 500 mbar. These increases, $\sim 50 \text{ m s}^{-1}$, were posited to be associated with the seasonal change for the equatorial region, as the tropics emerge from the ring's shadow and are exposed to increasing solar insolation.

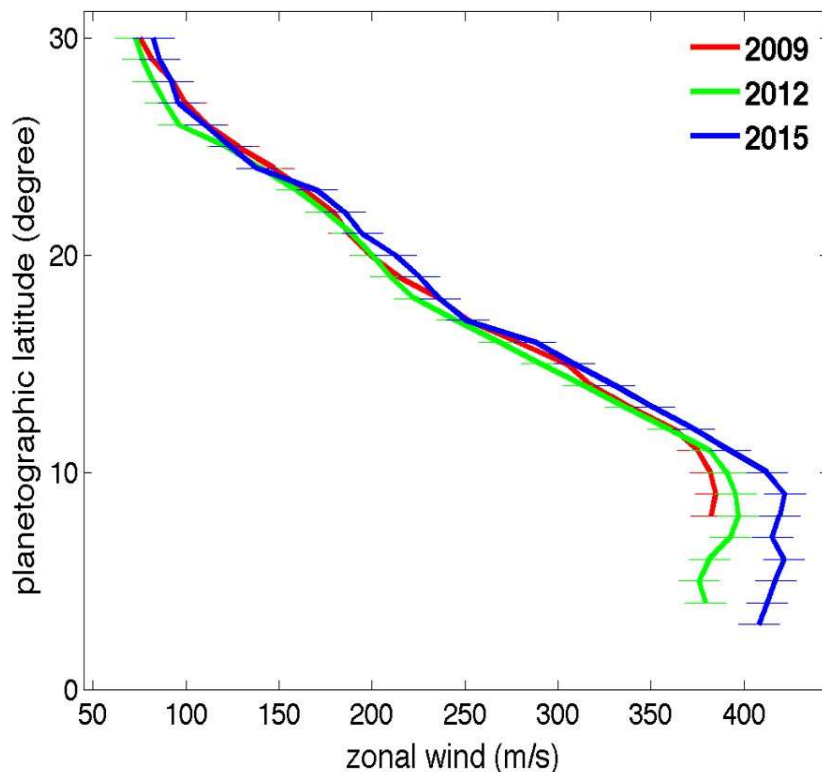


Figure 4.5. Comparison of the NH equatorial winds using the ISS CB3 filter between 2009 and 2015. Poleward of $\sim 12^\circ\text{N}$, these upper troposphere winds remained relatively consistent, to within their calculated error bands. Conversely, south of $\sim 12^\circ\text{N}$, these winds increased through this six-year period as this region moved out of the shadow of the rings and entered the NH spring season.

4.4. Data and Processing Methodology – CIRS Output

The Composite Infrared Spectrometer (CIRS) is a dual Fourier transform spectrometer, which measured spectra in both the far- and mid-infrared (Flasar et al., 2004). Figure 4.6

illustrates how the interferometers were positioned opposite each other, across the central axis of the CIRS and shared the received incoming radiation from a shared 50-cm diameter telescope, which was positioned in front of the instrument housing (Irwin et al., 2004, Fletcher et al., 2016).

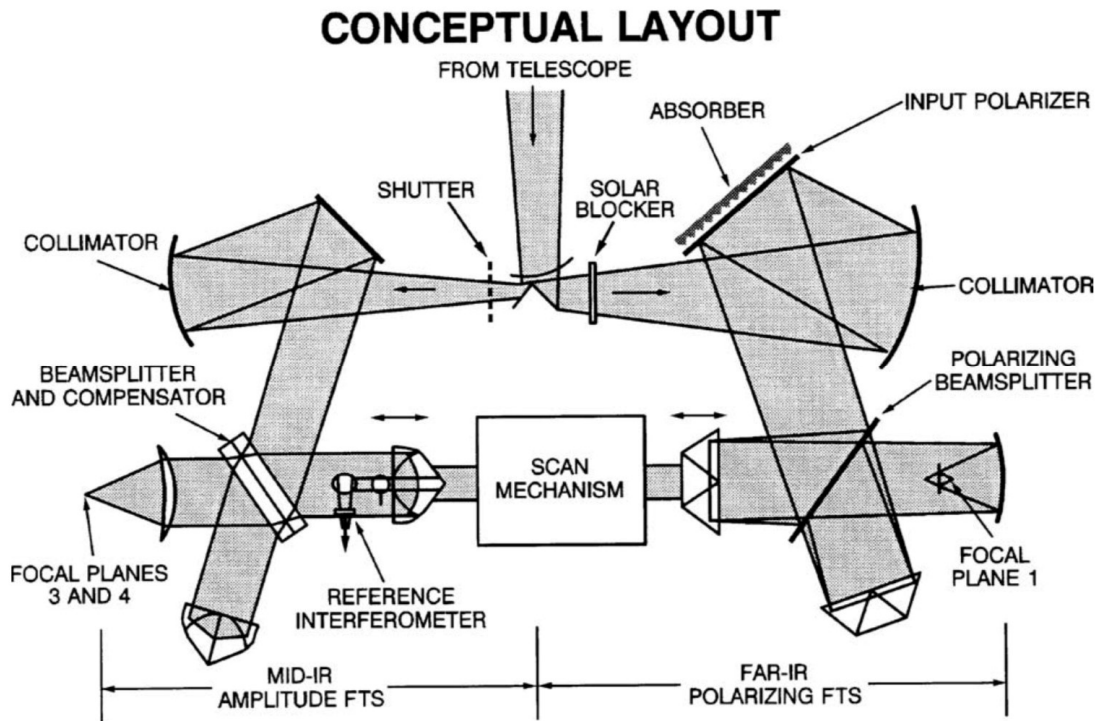


Figure 4.6. CIRS conceptual layout. Observed radiation is gathered by the telescope and then field-split between the mid-IR and far-IR interferometers. The moving retroreflectors both use the same drive mechanism (Flasar et al. 2004).

For the far-infrared measurements (wavenumber $10\text{-}600\text{ cm}^{-1}$, wavelength $17\text{ }\mu\text{m}$ to 1 mm), a polarizing interferometer, referred to as Focal Plane 1 (FP 1) was used with two thermopile detectors, sharing a common 3.9-mrad circular field of view (FOV). A Michelson interferometer provided the mid-IR spectra consisting of two focal planes, FP

3 and FP 4, which combined had a wavenumber range of 600 to 1400 cm^{-1} , equivalent to a wavelength of 7 to 17 μm (Flasar et al., 2004). This instrument consisted of an array of twenty detectors with a smaller FOV, 0.273 mrad, than the far-IR device, thereby increasing the spatial resolution for mid-IR data (Fletcher et al., 2007, Guerlet et al., 2018). The CIRS measured the thermal emissions with a spectral resolution that ranged from 0.5 to 15.5 cm^{-1} (Flasar et al., 2004) and a spatial resolution of 1-2° of latitude (Fletcher et al., 2007). The tropospheric temperatures were retrieved from spectra captured by the CIRS within the broad, collision-induced S(0) and S(1) hydrogen absorption lines, centered at 350 and 600 cm^{-1} , respectively. The temperature data was derived using mathematical fits to the ν_4 CH_4 band and H_2 -He collision-induced continuum at 15.0 cm^{-1} spectral resolution (Dyudina et al., 2009). Stratospheric temperatures, ranging from 0.5 to 5 mbar, were captured with the CH_4 emission band ($\sim 1300 \text{ cm}^{-1}$) (Li et al., 2008).

The CIRS also had the ability to perform both limb and nadir viewing. One use of the limb view was to observe the atmospheric cross-section, which yielded accurate and highly resolves vertical profiles of both temperatures and composition (Flasar et al., 2004). Limb viewing yielded a vertical resolution on ~ 1.5 times the scale height, $\sim 75 \text{ km}$ and also provided the opportunity to examine higher into the stratosphere (Fouchet et al., 2008).

Previous research has shown that radiance decreases with an increasing emission angle (Fletcher et al., 2010). Focal Plane (FP) 1 observed the upper troposphere and probed higher altitudes at higher emission angles in the far infrared (10-600 cm^{-1}). In the upper troposphere, the temperature decreases with altitude. Therefore, radiance recorded at high emission angles by FP1 will be from the relatively high, i.e., cold, troposphere, and will be smaller than the radiance measured at low emission angles, which originate from lower altitudes, where temperatures are warmer.

Radiance measurements from FP3 (600-1050 cm^{-1}) and FP4 (1050-1400 cm^{-1}) were primarily focused on the stratospheric emissions. Similar to the Earth's stratosphere, the temperature increases with height in Saturn's atmosphere. Therefore, the higher levels of radiance were recorded by these two FPs at high emission angles, since they originate from higher levels in the stratosphere. Conversely, lower levels of radiance were noted at low emission angles, which are from the lower stratosphere.

4.4.1 Data – CIRS Radiance Measurements

Radiance measurements were collected by three focal planes, FP1, FP3, and FP4, which used two FOV systems. The specifications for these systems are summarized in Table 4.2. The radiance data is then converted to atmospheric temperature data (Li et al., 2011). This

temperature data was then used to determine wind speeds through various levels of the upper troposphere (500 mbar) and into the stratosphere (0.1 mbar) (Li et al., 2016). Previous research has demonstrated the use of the TWE to derive wind speeds, though not without some accommodations in the equatorial regions. These specific modifications were reviewed in Chapter 3.

Table 4.2. Data collected through these CIRS focal planes was used to determine temperatures through the upper atmospheres and the associated thermal winds. Sorted by depth examined in Saturn’s atmosphere from top to bottom (Li et al. 2011).

	Wavenumber	Depth examined
Focal Plane 1	10-600 cm ⁻¹	300-500 mbar – Upper troposphere
Focal Plane 3	600-1050 cm ⁻¹	50-300 mbar – Upper troposphere & tropopause
Focal Plane 4	1050 -1400 cm ⁻¹	0.1 - 5 mbar – Stratosphere

From the collection of the raw sensor data by Cassini’s ISS to the determination of the zonal winds, there are several steps of data processing and analysis that must be completed. The techniques of data processing (Conrath & Gautier, 1980; Conrath et al., 1998; Flasar et al., 2004; Fletcher et al., 2010, Li et al., 2008, 2011), an overview of the TWE forms used for estimating the zonal winds, and the subsequent uncertainty estimates (Fletcher et al., 2016; Li et al., 2008, 2011) will be presented and were used as the baseline for this analysis.

4.4.2 Processing Methodology – CIRS Output

4.4.2.1 Data Processing

Similar to the ISS and VIMS data, the raw CIRS data cubes were accessed from the NASA PDS. However, that is where the similarity of the CIRS to these other two data archives ends. Where the ISS and VIMS data was examined the movement of clouds as proxies for the determination of the zonal winds, the CIRS data consists of thermal infrared emission measurements. The radiance data is used to derive the temperatures at various levels from the upper troposphere, outward into the stratosphere. The variance of radiance with emission angle is directly related to the vertical thermal structure of Saturn's atmosphere.

For a given spectral region, the thermal infrared emissions are dependent upon the atmospheric temperature and the concentration of optically active constituents in the observed region (Flasar et al., 2004). From the radiance data collected by the CIRS, the first step in the determination of the zonal wind patterns is establishing the temperatures through the observed extent of the upper atmosphere. The majority of the CIRS observations that were used in this analysis were nadir, i.e., the sensor detected the radiance as it looked directly below Cassini and perpendicular to the surface. The nadir observations have a higher horizontal spatial resolution, yielding improved temperature, and subsequent zonal wind estimates, along with measurements and enhanced

visualization of atmospheric wave patterns (Li et al., 2008). The use of multiple viewing geometries allowed for the extension of the pressure ranges along with the inclusion of the mid-IR results in a high spatial resolution (Fletcher et al., 2007)

The retrieval procedures for deriving the atmospheric temperature from the CIRS spectra is described in detail in Conrath and Gautier, 1980, Conrath et al., 1998, and Fletcher et al., 2010. The methodologies have been used in a multitude of previous studies including Li et al. (2008, 2011).

The derived temperatures are partitioned into three layers; unfortunately, this left a gap from 5 to 50 mbar, i.e., across the tropopause and the lower stratosphere. Therefore, this region was removed during the calculation of the thermal winds (Li et al., 2011).

The radiance data was organized into four-dimensional matrices, i.e., latitude, longitude, emission angle, and wavenumber, which are then categorized by Earth year and spectral resolution. These 4-D matrices were zonally averaged into three-dimensional matrices: latitude, emission angle, and wavenumber. Finally, these 3-D matrices were integrated over the three wavenumber ranges, as listed in Table 4-1. This final step yielded two-

dimensional matrices—latitude and emission angle—for specific time period and across varying spectral resolutions.

4.4.2.2 Estimations and Errors of Zonal Winds

In order to examine the zonal winds derived from the CIRS data, a different form of display and interpretation is required than the methodologies used with the ISS and VIMS output. This is because the CIRS data is infrared radiance collected at a multitude of levels through the atmosphere, which were then converted to temperature fields, per Section 4.4.2.1. The application of the general and standard forms of the TWE to temperature data to derive zonal wind profiles was discussed in Chapter 3. Section 4.6 will apply the newly-developed general form to 500-mbar zonal winds, which were retrieved from the ISS data and uses it as a boundary condition, along with radiance data collected by the CIRS, which was collected from within the troposphere out to about 0.1 mbar in the stratosphere

In the ideal case, the VWS is related to the horizontal temperature gradient along isobaric surfaces through the application of the TWE (Li et al., 2008). However, several factors found in the Saturnian atmosphere, particularly in the equatorial region, render the assumptions behind the standard TWE unusable. In the equatorial region, the

assumption of geostrophic balance is no longer valid due to the negligible Coriolis force. Additionally, substantial variations of the large-scale equatorial jets along with a rapid rotation period results in the forces that are the hydrostatic and geostrophic balance terms are not negligible.

While the ISS and VIMS data were of a different nature than the CIRS, the cloud-tracked zonal winds did play a role in the CIRS wind output. Combined with upper tropospheric and stratospheric temperatures derived from the CIRS radiance data, cloud-tracked winds were used as a lower boundary condition in the estimation of the stratospheric winds (Li et al., 2008).

There are both mathematical and physical limitations for where the zonal winds can be calculated. Between the 5- and 50-mbar pressure levels, there is no spectral sensitivity for CIRS nadir observations, so no radiance measurements can be made. Therefore, there was no data by which to calculate the temperatures or the subsequent thermal winds. Additionally, there is still a restriction of this modified TWE in the equatorial region; however, this one is driven by mathematics. In a procedure similar to Li et al. (2008) and Fletcher et al. (2016), the standard TWE was integrated along cylinder parallel to Saturn's rotation axis with CIRS thermal maps and the known 500-mbar winds. However, the

equation does not work in the area above and equatorward of the cylinders that are tangent to the equator at 500 mbar.

There are uncertainties with the zonal wind output from the CIRS data; however, these occur for different reasons than noted with the ISS and VIMS measurements. The uncertainties in the thermal wind calculations are dependent upon the uncertainties in CIRS-retrieved temperatures, which is ~ 1 K, and the associated meridional gradient (Li et al., 2008, 2011).

4.5 Previous Research – CIRS

Consistent with the previous ISS research presented in Section 4.3, a more thorough examination of the CIRS data has been conducted than previously applied to the VIMS data, which will be reviewed in Section 5.2. This is due to the fact that the CIRS output yields more complete, though derived, cross-sectional view of the zonal mean winds for a large vertical extent of the atmosphere. The CIRS output also does not have any dependency upon Saturn's rotation period, which factors into uncertainties in the wind fields calculated from the ISS and VIMS images.

Previous research conducted with CIRS examined spatiotemporal wind patterns on a global basis, including the examination of changes in tropospheric zonal wind over time, variability in the tropopause's height, and seasonal oscillations in the stratospheric jet structure. (Flasar et al., 2005; Fletcher et al., 2007, 2015, 2016; Guerlet et al., 2011, 2018; Li et al., 2008, 2011).

The first use of CIRS data to examine the zonal wind structure was published in Flasar et al. (2005). As Cassini was on its approach of Saturn, CIRS mapped temperatures across SH from the equatorial region ($\sim 8^\circ\text{S}$), poleward to the polar region ($\sim 78^\circ\text{S}$). The vertical extent ranged from the upper troposphere (~ 900 mbar) to the stratosphere (~ 0.1 mbar). By using the TWE, which relates the vertical shear in the zonal winds with temperature variations with latitude, Flasar et al. (2005) showed that tropospheric winds decreased by ~ 100 m s⁻¹ from the tops of the ammonia clouds (~ 500 mbar) extending up to the 1-mbar level.

Fletcher et al. (2007) examined eighteen months of CIRS data, which was collected from Saturn's Northern and Southern Hemisphere. At the time of the data collection, which ranged from October 2004 through March 2006, it was winter in the NH and summer in the SH. This gave the research team the opportunity to examine seasonal variations of the

atmosphere's structure, particularly, the tropopause, along with the variability of the pressure altitude of the radiative-convective boundary (350-500 mbar).

The examination of the meridional temperature structure conducted in Fletcher et al. (2007) yielded a better understanding of the asymmetries across hemispheres, along with the small-scale structures present with the warm belts and cold zones. Any maxima in meridional temperature gradient, dT/dy , is associated with a maxima in the thermal wind shear, du/dz , where u is the velocity of the easterly (prograde) zonal wind, while z is altitude. It was proposed that if the thermal wind shear yields a weakening of the zonal jet system with altitude, producing a uniform easterly jet, it can be presumed that in the SH, easterly zonal jets correlate with negative dT/dy , while westerly (retrograde) jets are associated with positive dT/dy , which yields positive thermal wind shear. (The specifics of the TWE and specifically, its application to Saturn's atmosphere were developed in Chapter 3 and will be applied in Section 4.6)

Fletcher et al. (2007) also examined the hemispheric difference in the pressure altitude of the radiative-convective boundary, which is delineated by a change in Γ . During summer months, which was the SH during the period of this research, the boundary is at deeper in the atmosphere, which is consistent with the hypothesis that the incoming solar

radiation penetrates further into the atmosphere during the summer, pushing the boundary downward.

Similar to the radiative-convective boundary, Fletcher et al. (2007) examined the hemispheric differences of the tropopause. This research posits that the tropopause height is the result of interaction between incoming solar radiation and atmospheric dynamics. Since these two factors experience seasonal variability, the tropopause would also share this variability, which is borne out by the results.

Li et al. (2008) extended the work of Fletcher et al. (2007) by examining CIRS data, which was collected between October 2004 and March 2008. The findings reinforced earlier research that suggested that the zonal-mean temperature of Saturn's equatorial region was relatively stable during this 3.5-year period, which coincided with the NH winter. Similarly, Li et al. (2008) showed the structure of the equatorial jet was consistent with the results presented in Flasar et al. (2005). Specifically, these results showed that the tropospheric jet structure in equatorial region on the SH, from 7°S poleward to 20°S, weakened as it extended outward from tropospheric cloud deck (~500 mbar) to the middle of the stratosphere (~1 mbar). Further out in the stratosphere, a strong jet was exhibited with maximum velocity of ~600 m s⁻¹ outward from the 1-mbar level, near 10°S.

While the stratospheric analysis was limited in the equatorial region due to the contemporaneous state of the research with regards to the TWE, CIRS limb observations in the equatorial region showed a cold center near the 10-mbar level at the equator. This cold core was estimated to yield a reduction of the zonal winds of $\sim 100 \text{ m s}^{-1}$. Even with this implied decrease, the stratospheric equatorial jet would have had a magnitude of $\sim 500 \text{ m s}^{-1}$, the strongest atmospheric jet discovered in our Solar System.

Guerlet et al. (2011) analyzed CIRS radiance data, subsequently deriving zonal winds using the modified TWE in cylindrical coordinates, a methodology initially demonstrated in Flasar et al. (2005). Through the comparison of the 2005-2006 and 2010 zonal wind data, it was noted that the alternating easterly and westerly jet structure extending through the stratosphere had shifted downwards, towards the tropopause, during this four- to five-year period. This pattern, termed Saturn's Equatorial Oscillation (SEO), is similar to Earth's quasi-biennial oscillation (QBO).

Through the analysis of both the vertical motion of the jets, along with the changes in magnitude, the period of the complete SEO cycle is approximately 14.9 years (Guerlet et al., 2011). The period is approximately half of a Kronian year; however, this research did

not finalize any conclusions as to whether this was fortunate happenstance or associated with a physical mechanism associated with seasonal changes.

Li et al. (2011) examined the long-term (2004-2008) variations in the zonal wind patterns using both ISS and CIRS data. In addition, the research specifically sought out data from both sensors that were in similar time frames. This was achieved for data acquired in April-May 2005 and December 2008. The ISS data revealed that between 2004 and 2008 that tropospheric zonal winds (~ 500 mbar) only increased a few m s^{-1} during this time period; however, winds near the tropopause (~ 60 mbar) increased $\sim 20 \text{ m s}^{-1}$, which was larger than the uncertainty. The analysis of the CIRS data showed a significant warming trend around the tropopause during the 2005-2008 time period. This warming trend can work as a relevant proxy for the zonal winds, as established through the thermal wind relationship. Conversely, Li et al. (2011) posited that the small change in the deeper tropospheric winds was probably related to the radiative adjustment at the level requiring a longer timescale.

The analysis presented in Fletcher et al. (2015) examined CIRS data extending from 2004 to 2014 across both the north and south polar regions. This research examined changes in the upper atmosphere, ranging from 0.5 to 110 mbar, of both the atmospheric motion and

structure. Consistent with Li et al. (2011), this research showed that the winds in the upper troposphere (~110 mbar) were relatively stable in both polar regions. The vertical structure in the SH was consistent with the results presented in Baines et al. (2009), where the areas of maximum wind shear aligned with the jet locations. However, Fletcher et al. (2015) noted that NH atmospheric structure was not as orderly as the SH.

In the NH, Fletcher et al. (2015) showed that the peak 100-mbar jet was located 1° latitude south of the jet's center at the top of the ammonia clouds, ~500 mbar (Baines et al., 2009). Within the NH's upper troposphere, a greater level of variability was noted over this extended study, particularly with two of the jets switching from retrograde to prograde motion, and the jets shifting further north between 2004 and 2011.

Within the stratosphere, similar to what was posited in Li et al. (2011), Fletcher et al. (2015) noted that the vertical temperature structure ($\partial T/\partial y$) changes significantly as the Kronian seasons progressed. These changes would yield positive VWS in the winter hemisphere, while the summer hemisphere would experience negative VWS. This hypothesis is supported through observations of time of zonal jets at the 1-mbar level, located at 74°S and 78°N. At the beginning of the observation period (2004 for the SH, 2006 for the NH), both of these jets were retrograde. Over the period of study, both jets

weakened and reverted to prograde flow through the Kronian seasons. For the SH jet, the transition occurred during the 2012 - 2013 time frame, while it occurred during 2007 - 2008 in the NH.

Finally, Fletcher et al. (2015) noted that, as expected, the zonal wind field and resultant VWS remained in balance with the temperature contrasts through the seasonal changes. Additionally, the wind field of the middle atmosphere, upper troposphere and into the tropopause, may also be vary seasonally. The vertical profile of the zonal winds, as they extend from the upper troposphere and into the lower stratosphere, is important to further our understanding of vertically propagating waves, along with the atmosphere's evolving ability to vertically trap these waves, which influences tropospheric dynamics.

The research presented in Fletcher et al. (2016) included examinations of the changes in temperature structure and by extension, the zonal winds, within the upper troposphere from 2004 through 2014. The investigation of the CIRS data showed that, at most latitudes, the zonal winds across the upper troposphere exhibited minimal fluctuations over the period of study.

However, significant variations were noted in Saturn's NH, specifically in the broad westerly (retrograde) jets as the NH emerged from its winter (Fletcher et al., 2016). Poleward of 45°N, the westerly jets at the 100-mbar level have become more easterly over the ten-year period examined, which corresponds to an increasing positive (easterly) VWS. It was noted that while that this change was less than the level of uncertainty defined in the research, the trend was continuous over time and did not exhibit any randomness. A notable exception in the NH was the retrograde jet located near 39°N, which was associated with the Great White Storm of 2010, which will be elaborated on in Chapter 6. This jet increased its westerly velocity over time, which was attributed to increasing negative VWS. For the SH, some changes in tropospheric jet structure were noted with increasing easterly shear on the broad westerly jets, as the SH progresses from summer into autumn.

Guerlet et al. (2018) studied CIRS data that was gathered in the limb-viewing geometry between 2005 and 2015 to examine the vertical structure and evolution of the SEO. This research was an extension of Guerlet et al. (2011) and focused on stratospheric thermal readings, as the deepest extent of the readings was 20 mbar because of viewing geometry constraints through the ten-year period. The wind speed analysis in Guerlet et al. (2018) showed that a new easterly wind speed maximum developed high in the stratosphere,

i.e., 0.03 mbar. The authors posited that the local maximum resulted from upwardly propagating waves depositing their eastward momentum at this pressure level, if this development was analogous to the Earth's QBO.

Another potential reason for localized stratospheric jet would be radiative damping of the waves. Over the ten-year period, it was noted that two of the wind speed extrema had continued to drop towards the tropopause, which was consistent with analysis presented in Guerlet et al. (2011), which examined CIRS data from 2005 through 2010. Along with its descent, it was observed that the maxima had not only weakened, but also narrowed. These impacts of its downward motion are consistent with the idea that the SEO would be dampened in the lower stratosphere. The dampening accelerates as the SEO moved into the lower temperatures and higher pressures, closer to the tropopause. Finally, Guerlet et al. (2018) proposed that eddy dissipation would also impact the descending and weakening SEO.

4.6 CIRS Analysis: Zonal Winds at & above the Visible Cloud Level

The validation of the two forms of the TWE with Terran data (Section 3.4.1) was critical for the ability to proceed with using the general form in future planetary atmospheric research. With the focus of this dissertation work being the spatiotemporal variation of

Saturn's atmosphere, the two TWE forms were applied to data collected by the CIRS and ISS instruments. These results and their implications will be presented within this section. Similar to the validation of the TWE forms presented in Section 3.4.1, the two assumptions made for the standard form, geostrophic and hydrostatic balance, will be reviewed through scalar analysis. The largest centrifugal force due to relative motion on Saturn is estimated to be $V^2/a \approx 400^2/6 \times 10^7 \approx 2.7 \times 10^{-1} \text{ m s}^{-2}$, which is much smaller than its effective gravity, $g_e = g - \Omega^2 a \approx 10.4 - (1.7 \times 10^{-4})^2 \times (6 \times 10^7) \approx 8.7 \text{ m s}^{-2}$. The largest Coriolis force on Saturn, $\Omega \times V \approx 1.7 \times 10^{-4} \times 400 \approx 6.8 \times 10^{-2} \text{ m s}^{-2}$, is also much smaller than the effective gravity. Therefore, the hydrostatic approximation is valid for this scenario.

For additional consideration in the scalar analysis, analysis of the banding phenomenon noted on Saturn (Ingersoll, 1990; Gierasch, 1996) along with the planetary waves (Achterberg & Flasar, 1996) showed that the length-scale of the large-scale motion is likely on the order of 10^4 km . Examination of the Rossby number at a latitude of 30° yields $R_o = U/fL \approx 400/(2\Omega \sin 30^\circ \times 10^7) \approx 0.2$, which is not much smaller than 1. This result implies that the geostrophic balance is not valid in the equatorial regions.

For further investigation in the application of the TWE with regards to Saturn, data that was collected by the Voyager missions, along with the Cassini mission will be examined.

Flasar et al. (2005) applied that standard TWE in the low to mid-latitudes, i.e., 8-30°S, using data collected during the 1980-1981 Voyager missions. Specifically, temperature maps with a resolution of 8°, along with smoothed zonal winds based on a cloud tracking methodology, will be used as the bottom layer, ~500 mbar, in the integration scheme. A gap in the Voyager measurement ranging from 1°S to 27°S was filled by Cassini ISS observations (Porco et al., 2005). Additionally, radiance data collected by the CIRS was converted to temperature fields through a process described in Section 4.4.2. Figure 4.7 shows a zonal-mean temperature map as a latitude-altitude cross-section of data collected from 2004 through 2006, which was constructed by the CIRS group at the National Aeronautics and Space Administration (NASA) - Goddard Space Flight Center (GSFC). It is noted that due to the lack of instrument sensitivity for an atmospheric layer from 5 to 50 mbar, the temperature data was interpolated and brings a level of uncertainty to the derived zonal winds.

It is also noted in Figure 4.8 that there is a pair of stratospheric equatorial jets, above the ~1-mbar level. The interpolated temperature data between the 5-mbar and 50-mbar levels does not appear to impact the representation of these jets. This is because the large temperature gradients in the equatorial region above the ~5-mbar level yields the strong VWS, which in turn support this jet structure. This also implies that this jet structure is

not very sensitive to the temperature and zonal wind structure across this portion of the tropopause, i.e., ~5 to ~50 mbar, unless the winds in this layer were strong and in the opposite direction. These results reinforce findings that there are stratospheric jets on Jupiter (Flasar et al., 2004), as well as Saturn.

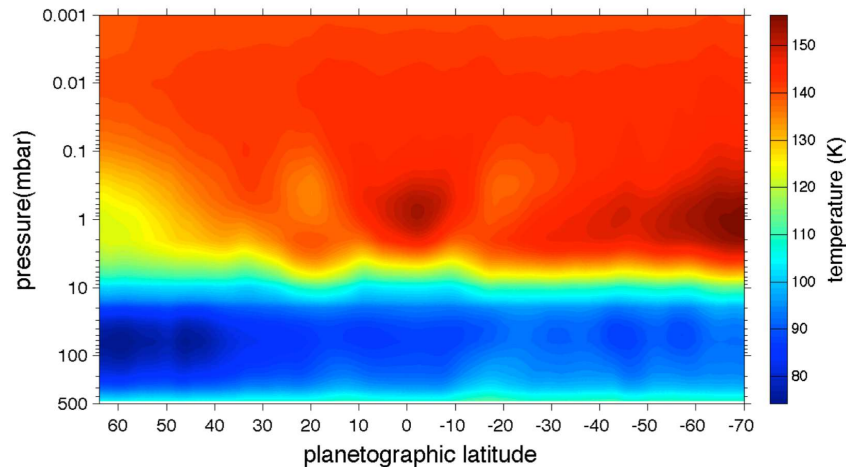


Figure 4.7. Cassini CIRS high spatial resolution zonal-mean temperatures across Saturn's upper atmosphere in latitude-altitude cross section; Data processed by the GSFC Cassini CIRS group. The temperatures between the 5- and 50-mbar levels are relatively uniform, as they are interpolated values, resulting from the lack of instrument sensitivity across the tropopause.

Figure 4.8 shows the derived zonal wind values from both forms of the TWE with the boundary conditions set at the 500-mbar level, collected by the ISS in late 2004, and using the 2004-2006 high-resolution temperature data collected by the CIRS. Panels A and B of Figure 4.8 show the zonal wind outputs from the standard and general forms, respectively. These results from both of the TWE integrations represented in Figure 4.8 are generally consistent with previous analysis in both the high-latitude region (Fletcher

et al., 2007), along with the equatorial region of the SH (Flasar et al., 2005). The analysis shows low-latitude jets positioned at $\sim 15^\circ\text{N}$ and $\sim 15^\circ\text{S}$, which both weaken to about 0 m s^{-1} at $\sim 1\text{-mbar}$ level. The decay of these stratospheric jets with altitude is stronger than observed in previous research (Flasar et al., 2005). This trend is potentially because the temperature data had a higher spatial resolution and better resolved the vertical shear in the zonal winds.

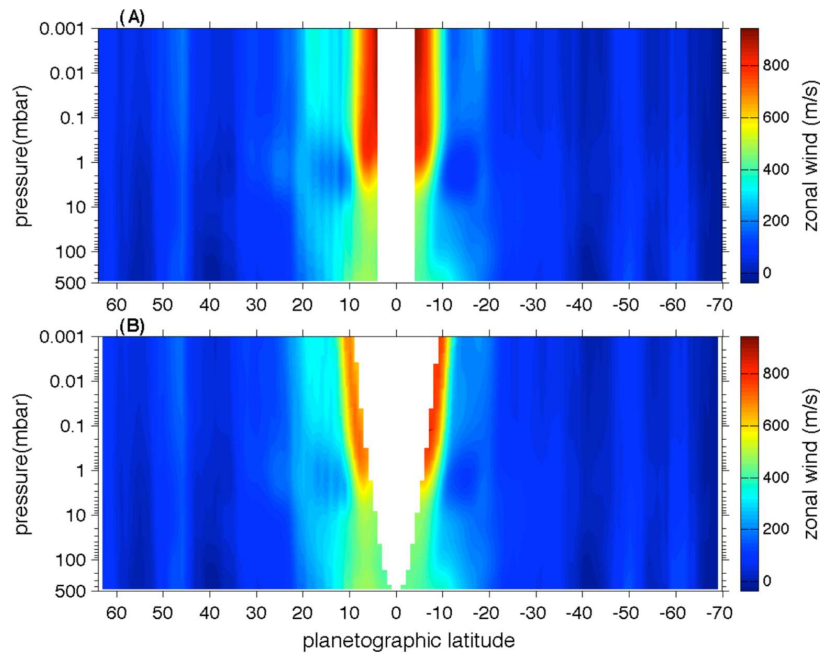


Figure 4.8. Comparison of the thermal winds through Saturn's upper atmosphere, derived through the standard and general forms of the TWE. These calculations were based upon the high spatial resolution (1°) temperatures, generated by the GSFC Cassini CIRS group. Panel A presents the derived zonal winds, based on the standard TWE. The equatorial region between 4°S and 4°N are neglected because the assumption of geostrophic balance, which is used in the standard TWE, does not work well in the equatorial region. Panel B illustrates the calculated zonal winds, based on the general TWE. The latitude excursion is $\sim 9^\circ$, when reaching the top of the integrated atmosphere in the equatorial zone.

It is also noted in Figure 4.8 that there is a pair of stratospheric equatorial jets, above the ~1-mbar level. The interpolated temperature data between the 5-mbar and 50-mbar levels does not appear to impact the representation of these jets. This is because the large temperature gradients in the equatorial region above the ~5-mbar level yields the strong VWS, which in turn support this jet structure. This also implies that this jet structure is not very sensitive to the temperature and zonal wind structure across this portion of the tropopause, i.e., ~5 to ~50 mbar, unless the winds in this layer were strong and in the opposite direction. These results reinforce other findings that there are stratospheric jets on Jupiter (Flasar et al., 2004), as well as Saturn, among the four gas giant planets of our solar system.

The two forms of the TWE applied to yield Figure 4.8 also highlight some obvious discrepancies in Saturn's equatorial region. It has been shown that the assumption of geostrophic balance is not applicable in the low-latitude regions. Additionally, the use of the cylindrical and radial integration routines in the TWE yield these differences. Figure 4.9 shows the temperature gradient corresponding to the temperature fields in Figure 4.7 and is also overlaid with a visual representation of the two integration routines for the same location, 10°N, between 0,001 and 500 mbar, ~600 km. This schematic shows the latitude excursion between the standard and general forms of the TWE and illustrates

that each integration routine passes through a different temperature-gradient region, so that two forms yield different solutions.

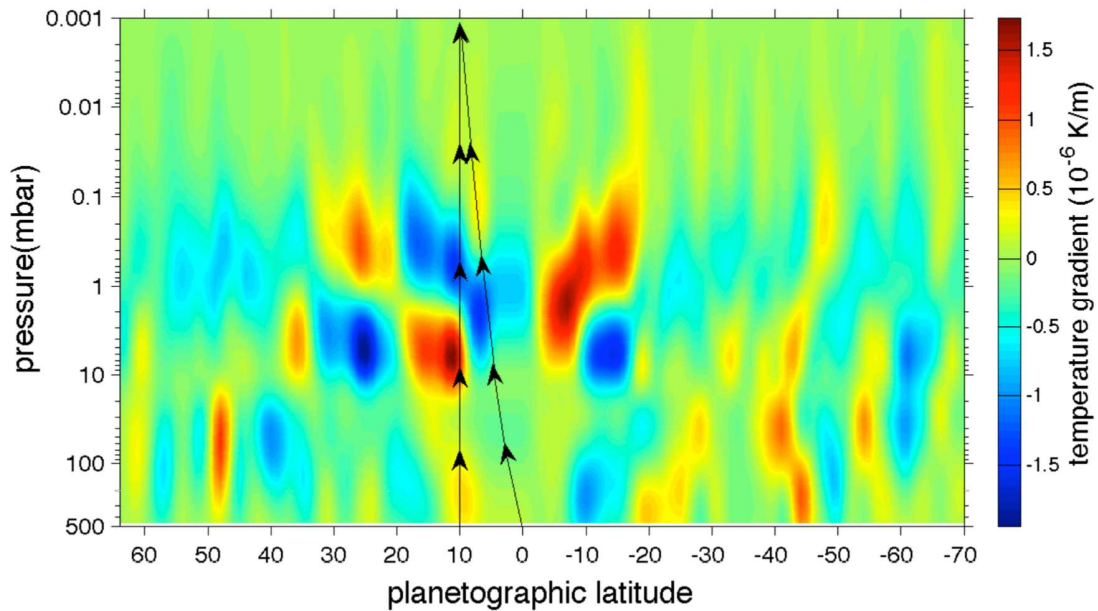


Figure 4.9. Graphic representation of different integration routines used in standard and general forms of the TWE. Meridional temperature gradients, based on derived temperatures from the CIRS (Figure 4.7), are also plotted. The straight (vertical) arrow is the integration routine of the standard TWE, while the curved arrow is that of the general TWE.

This research team utilized a data from the same time period, 2004 through 2006, but with a different data processing methodology, to compare to these two results. Figure 4.10 shows a comparison of the zonal wind outputs from the NASA-GSFC (Panel A) and the Oxford (Panel B) groups. The figure demonstrates that the stratospheric jets (above ~1 mbar) exist in both analyses, suggesting that these jets are stable, at least in short time scales.

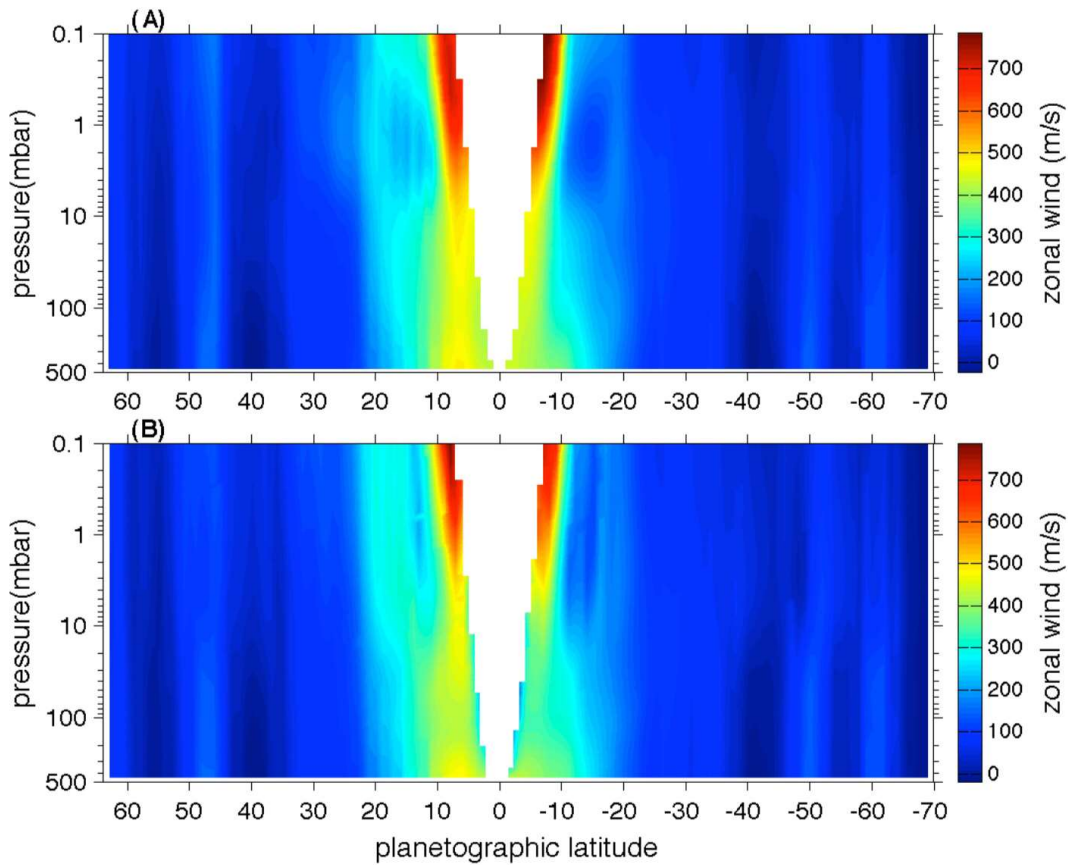


Figure 4.10. Comparison of the thermal winds of Saturn's upper atmosphere, based under two independently-derived temperature profiles. The zonal winds in Panel A were derived using temperatures from the GSFC Cassini CIRS group, which are the same results as Panel B of Figure 4.14. Panel B shows the zonal winds that were calculated, based upon the temperature data retrieved by Oxford University. The lower portion of Panel B was terminated at the 500-mbar level to be consistent with the GSFC data.

In order to achieve a broader perspective, the seasonal variations from the stratosphere, across the tropopause, and into troposphere were also examined. It should be noted that this research used the 360-mbar zonal winds from ISS analysis as the boundary condition for the determination of the CIRS winds through the integration of the TWE. However,

given the additional depth of the CIRS available, the thermal wind equation was also integrated downward, further into troposphere, reaching the 750-mbar level. The CIRS dataset extended from 2009, when the NH was transitioning into the spring season, through 2015, when NH reached its summer solstice.

Figure 4.11 shows three atmospheric temperature profiles, ranging from 70°S to 70°N. In 2009, the SH transitioned from summer to fall in August of that year, the stratosphere was warm with temperatures in excess of 140 K. With the seasonal transition underway, there warmer temperatures extended north into the NH, as far as ~45°N. Additionally, the NH troposphere was notably cold, as it was its winter, with temperatures at the ~100-mbar level of less than 80 K. By 2012, significant warming occurred in the Northern Hemisphere's stratosphere, while temperatures cooled in the Southern Hemisphere's counterpart. As the seasonal transition continued into 2015, notable stratospheric cooling occurred across the SH, while NH temperatures moderated.

In addition, the dashed circle noted in all three panels of Figure 4.11, bringing focus to the equatorial temperatures in lower portions of the stratosphere, particularly at 5-mbar level. In 2009, this region is notably warm-core with temperatures in excess of 140 K. With the seasonal transition underway in 2012, cooling is observed through the CIRS data

across the entire area. By 2015, temperatures continued to drop in this equatorial region and became a cold-core region. As the temperatures dropped over this seven-year period, the temperature gradient changed, yielding a change in the thermal winds.

Through the application of the general form of the TWE, this analysis illustrates how the the stratospheric equatorial jet had weakened from $\sim 500 \text{ m s}^{-1}$ in 2009 to $\sim 0 \text{ m s}^{-1}$ in 2015 (Figure 4.12). From these results, it can be posited that the sharp decrease in the strength of the jet was related to changes in the stratospheric temperatures over this seven-year time frame.

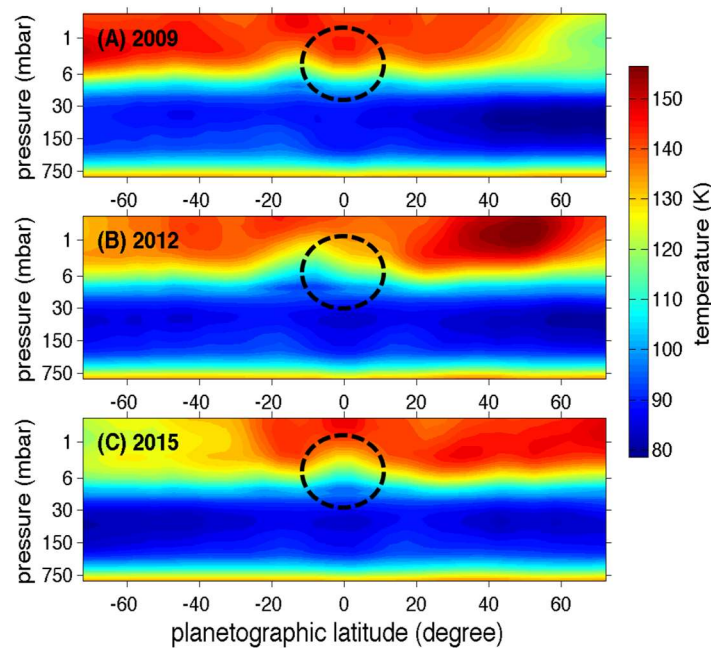


Figure 4.11. Comparison of atmospheric temperature profiles, ranging from 70°S to 70°N . Panels A, B, and C shows the derived temperatures (K) in a latitude-altitude cross-sectional plot from 2009, 2012, and 2015. As Saturn transitioned to NH summer, the dashed circle in all three plots shows that in the equatorial zone that went from being a warm-core to cold-core region.

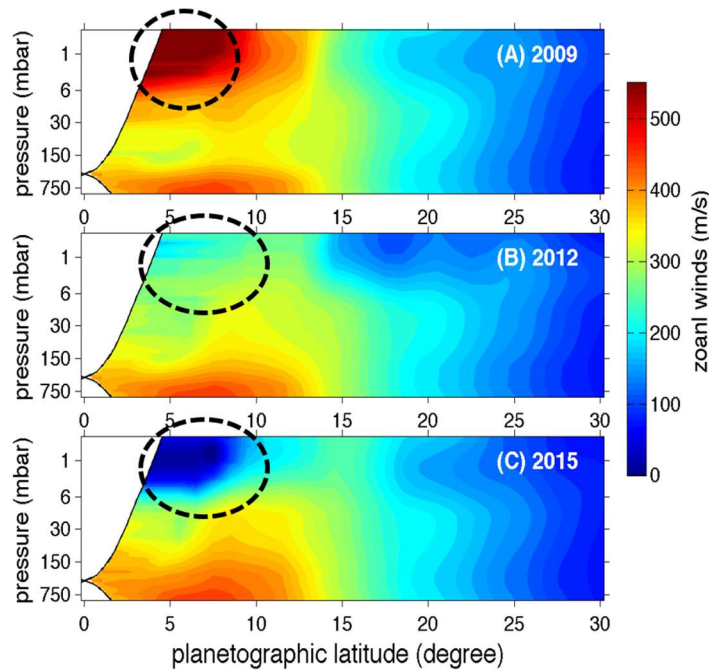


Figure 4.12. Comparison of the NH stratospheric equatorial jet (~ 0.1 mbar) between 2009 and 2015. Using CIRS temperature data (shown in Figure 4.11), Panels A, B, and C shows the zonal winds in a latitude-altitude cross-sectional plot from 2009, 2012, and 2015. As Saturn transitioned to NH summer, the stratospheric jet decelerated from over 500 m s^{-1} in 2009 to $\sim 0 \text{ m s}^{-1}$ in 2015. This deceleration was directly related to stratospheric cooling during the seasonal changes.

4.7 Conclusions

This chapter reviewed the technical specifications and applications of the ISS and CIRS from the Cassini mission. Additionally, an overview of past research and the progression of the planetary science and specifically, our understanding of the Kronian atmosphere, was presented. Additionally, an analysis of both CIRS and ISS data was provided to yield further insight into the spatiotemporal variations from Saturn's troposphere, across the tropopause, and out into the stratosphere. Moreover, coupled with the results of Chapter

3, a new general form of the TWE, time-averaged CIRS data were paired with 500-mbar winds, which were estimated from ISS data to provide a long-term view of the equatorial stratospheric jet structure.

With the regards to the analysis of the ISS data, during the SH summer period (2004 – 2008), the tropospheric winds, ~300 to 500-mb level, remained steady through this five-period. However, the 50-mb winds within the tropopause accelerated through this time period by about $\sim 30 \text{ m s}^{-1}$. This acceleration may be related to continued summer levels of solar insolation and more rapid response to this pattern in the higher levels of the atmosphere.

Further studies were conducted on ISS CB3 data for the equatorial region of the NH, extending poleward to 30°N for the 2009 through 2015 period. This time frame spanned the very end of NH winter and into most of its spring. With this seasonal change, as well as emerging from the shadow of the ring, the NH was exposed to increasing levels of solar insolation. This pattern led to an increase of the zonal wind speeds, $\sim 50 \text{ m s}^{-1}$, across the equatorial region in the upper portion of the troposphere. Conversely, poleward of 12°N , there were negligible changes in the zonal wind pattern through this seven-year period.

Applying the research presented in Chapter 3, the application of the general form of the TWE to the data collected by Cassini while observing Saturn allowed for the opportunity to examine the upper-level zonal winds. By using the high spatial resolution temperature data from the CIRS and an appropriate boundary condition, established by ISS data, a global perspective of the zonal winds extending from the troposphere, across the tropopause, and into the stratosphere was presented. These global estimates implied that the decay of the low-latitude jets with height is also demonstrated in the NH, similar to the research conducted in Flasar et al. (2005) and had focused on the Southern Hemisphere.

A notable result showed that through the use of the new form of the general TWE with independently-derived temperature data from different time periods, there are very strong, $\sim 800 \text{ m s}^{-1}$, stratospheric jets within the equatorial zone. Previous research conducted by Fletcher et al. (2007) and Li et al. (2008) had estimated the velocity of the equatorial stratospheric jets to be $\sim 500 \text{ m s}^{-1}$. The stronger upper-level jets are also remarkable in that they are stable features, at least in the short-term.

However, while these equatorial stratospheric jets persist through at least the short-term, a long-term perspective shows a pattern of weakening aligned with seasonal changes. As

the meridional temperature gradients varied over time, the thermal winds also changed. The oscillating pattern shown in these results is in agreement with previous research conducted into Saturn's spatiotemporal variations in atmospheric patterns, including the QGO and SEO (Fouchet et al., 2008, Guerlet et al., 2011, 2018; and Li et al., 2008, 2011).

Chapter 5 (Task 3): Spatiotemporal Variations of Saturn's Zonal Winds below the visible cloud level

Research originally published in: Studwell, A., Li, L., Jiang, X., Baines, K. H., Fry, P. M., Momary, T. W., & Dyudina, U. A. (2018). Saturn's Global Zonal Winds Explored by Cassini/VIMS 5- μm Images. *Geophysical research letters*, 45(14), 6823-6831.

To complete our view inside of Saturn's atmosphere from what was completed in Chapter 4, this task will examine the global extent and the historical trends of Saturn's tropospheric zonal winds using data from the Cassini Visual and Infrared Mapping Spectrometer (VIMS; Brown et al., 2004). By comparing the deeper zonal winds captured by the VIMS with the 300- to 500-mbar level winds acquired by the ISS and derived from the CIRS data, an improved understanding of the vertical wind structure on a global scale can be attained. Additionally, knowledge about the spatiotemporal variations of the zonal winds in the deeper troposphere, $\sim 2,000$ mbar, will be increased as a result of this research. The combination of these results with those achieved in Chapter 4 both provides important information about the large-scale dynamics of Saturn, but also helps the scientific community develop new theories and models of the general circulation for giant planets, both within the Solar System and of exoplanets.

The VIMS images recorded by Cassini are in the 5- μm range; this range is sensitive to pressure levels around 2,000 mbar (Baines et al., 2005, 2009; Momary et al., 2006). At the

levels of interest for the VIMS data, it examines a layer of ammonium hydrosulfide clouds, which extends between the 3,000 and 5,000 mbar (Additional information on the operations of the VIMS will be provided in Section 5.1). Through the Cassini mission and in the years since, these 5- μm VIMS images have been used to examine zonal winds within the relatively deep troposphere (Baines et al., 2005, 2009, 2018; Choi et al., 2009; Dyudina et al., 2009; Li et al., 2016; and Studwell et al., 2018).

5.1 Data and Processing Methodology – VIMS Output

The Visual and Infrared Mapping Spectrometer (VIMS) instrument (Figure 5.1) was a 64 x 64-pixel spectrograph, which produced near-simultaneous observations in 352 different wavelengths, ranging from ~ 0.3 to ~ 5 - μm range (Brown et al., 2004). By definition, the VIMS was a hybrid instrument, composed of a slit-scanning visible spectrometer (Capaccioni et al., 1998) along with a spot-scanning near-infrared spectrometer (Brown et al., 2004).

5.1.1 Data – VIMS 5- μm Images

For this research, the data of primary interest was in the near-infrared band, specifically in the 5- μm range, with the intent of analyzing deeper layers in the atmosphere. The near-infrared channel mapped from 0.85 to 5.1 μm with 256 contiguous bandpasses and the

spectral sampling interval was $0.006 \mu\text{m}$. For the examination of the near-infrared channel, a single-element, 256-channel spectrometer was used, which then maps spatially in two dimensions upon an orthogonally-directed mirrors (Baines et al., 2005).

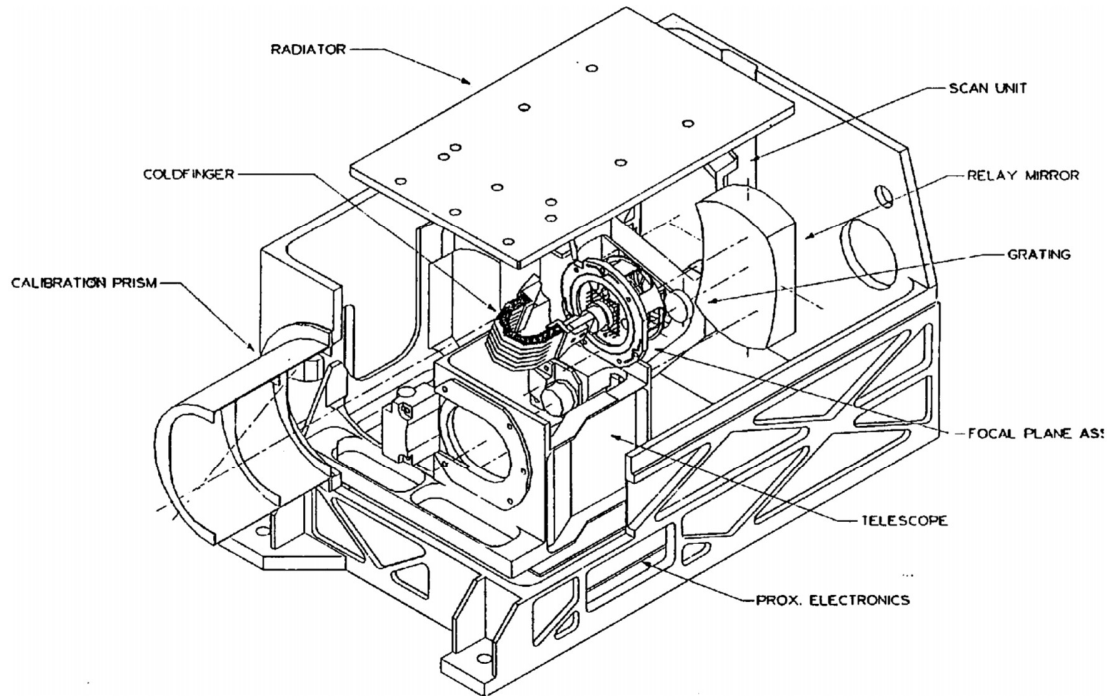


Figure 5.1. VIMS conceptual layout. The specific location of the VIMS within the Cassini spacecraft is shown on Figure 4.1 (Brown et al., 2004).

The $5\text{-}\mu\text{m}$ band, ranging from 4.6 to $5.1 \mu\text{m}$, directly observed Saturn's thermal emissions with cloud features being backlit against the infrared emissions. In this band, collision-induced opacity due to $\text{H}_2\text{-He}$ is at a minimum and there is an absence of strong CH_4 absorption. The combination of traits found in this spectral window allowed Cassini to examine further into the troposphere (Fletcher et al., 2011). Specifically, this wavelength provided data from the 1,000- to 3,000-mbar level, observing the troposphere (Figure 5.2).

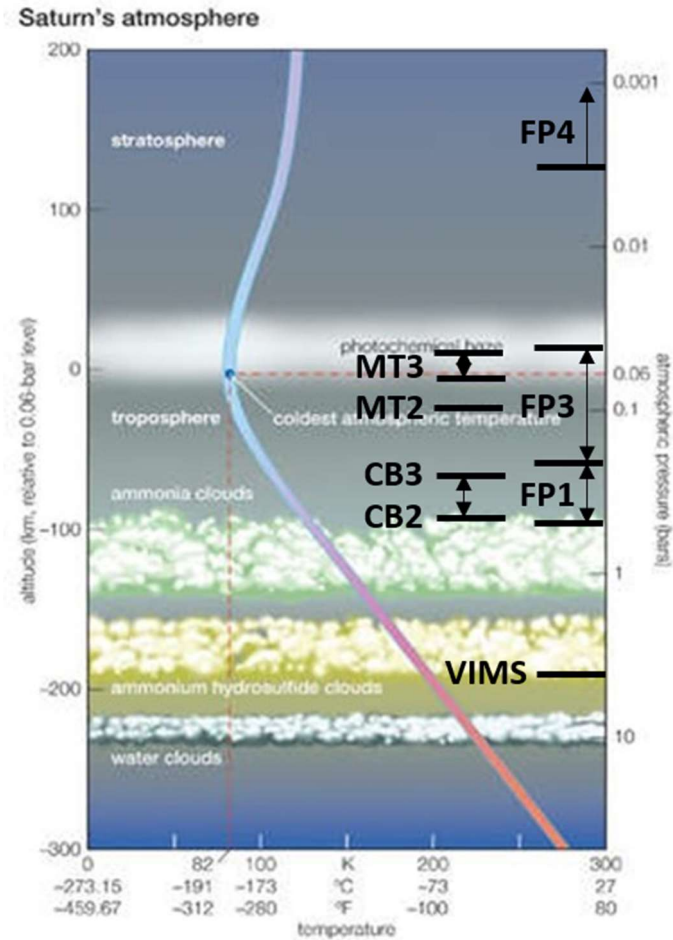


Figure 5.2. Cross-section of Saturn's atmosphere, noted with pressure levels observed by the CIRS, ISS and VIMS. Specific observation pressure levels for the CIRS and ISS are listed in Tables 4.1 and 4.2. For the VIMS, the 5- μ m band observed thermal emissions from ~5,000-mbar level, which backlights the ammonia and ammonium hydrosulfide cloud layers (Adapted from Hubbard, Buratti, & Marley, 2020).

By selecting the 5- μ m band, it was inferred that the observed cloud structures are located between the top of the atmosphere and the 5- μ m emission level (Choi et al., 2009). The 5- μ m emission layer is estimated to be close to 5,000 mbar, which is below the estimated altitude (1,000 – 3,000 mbar) for the bases of the ammonia clouds. These ammonia clouds are the uppermost cloud layer within the troposphere and are also visualized in the ISS

images, which are produced from the solar radiation reflected off the top of the ammonia clouds (Bjoraker et al., 2007).

Research presented in Dyudina et al., (2009) compared cloud features within the south polar vortex that were observed in VIMS imagery. The analysis compared the cloud structure that was presented by both reflected sunlight, which was captured in the visible spectrum, and through the thermal emissions, which used the infrared portion of the VIMS sensors¹.

A conclusion from Dyudina et al., (2009) posited that the ammonia clouds extend across the ~1,000 to 2,500-mbar region of the troposphere. This range was based on spectral analysis of images captured on the night side of Saturn, which indicated that the clouds, on average, are at the ~2,000-mbar level. This analysis was based on the assumption that phosphine concentration is relatively constant across the hemisphere.

While the VIMS had a native imaging resolution of about $0.25^\circ \text{ pixel}^{-1}$, the observed resolution varied, based on Cassini's distance from the observation location and with

¹ It is key to note here that when examining the thermal emissions data from the 5- μm band, that the clouds are silhouetted against the outgoing thermal emissions from the ~5,000-mbar level. Consequently, the clouds show up as dark spots on the imagery.

emission angle. On average, Cassini made observations from a distance of approximately 900,000 km, resulting in 1° being ~ 1000 km; therefore, the native resolution equaled 250 km (Choi et al., 2009). It is noteworthy that research presented in Baines et al. (2009) was able to examine mosaics where a resolution of 122 km was achieved in the VIMS' instantaneous field of view (FOV), as Cassini was passed between 224,000 and 442,000 km above the clouds, while observing the Northern Hemisphere during June 2008.

During Cassini's first Grand Finale pass in April 2017, a mere four weeks prior to optimal lighting conditions for polar observations of the NH, the VIMS collected a pair of spectral images from the pole equatorward to approximately 87°N (Baines et al., 2018). The orbital geometry of Cassini's first pass yielded a closest approach of $\sim 111,000$ km above the cloud tops, which provided a spatial sampling of 35 km per pixel; this is in contrast to the aforementioned Baines et al. (2009), where a resolution of 122 km was achieved in the VIMS' instantaneous FOV.

Within an hour of the first pass, Cassini made a second flyby of the NH polar region at an altitude of $\sim 69,000$ km (Baines et al., 2018). Due to the spacecraft being at a lower altitude, the pole was observed more obliquely. This restricted both the longitudinal extent of the observations and provided a slight degradation of the spatial sampling to

45 km per pixel. These noted observational improvements allowed for this research to detect local ammonia clouds in the NH polar vortex, where it was otherwise notably absent of observable aerosols.

5.1.2 Processing Methodology – VIMS 5- μ m Images

From the collection of the raw sensor data by Cassini's VIMS to the determination of the zonal winds, there are several steps of data processing and analysis that must be completed. The techniques of data processing (Barnes et al., 2007; Choi et al. 2009; Gaddis et al., 1997; McCord et al., 2004), navigation and fitting (Acton, 1996; Antuñano et al., 2015; Choi et al. 2009; Sánchez-Lavega et al., 2007; and Sromovsky et al., 2018), the methods for estimating the zonal winds and the subsequent uncertainty estimates (Choi et al., 2009; Del Genio et al., 2007; Limaye, 1986; Salyk et al., 2006, and Studwell et al., 2018) will be reviewed and used as the baseline for this dissertation's analysis.

5.1.2.1 Data Processing

VIMS data cubes, i.e., multidimensional arrays, were accessed from the NASA Planetary Data System (PDS) Imaging Node and similar to Choi et al. (2009), the analysis was limited to data that either (1) attempted feature tracking by repeatedly scanning the same absolute frame, relative to the System III longitude, or (2) gathered a full-disk mosaic

which observed the overall status of the Saturn's atmosphere over a full Saturnian day. (System III longitude refers to a Saturn-centric planetocentric spherical references which uses magnetic field vectors, B_r , B_θ , B_ϕ , as the reference frame (Desch & Kaiser, 1981).)

The standard VIMS data pipeline was performed on the data set using software provided by the VIMS team (Choi et al., 2009). The complete pipeline description is provided in Barnes et al. (2007). In summary, raw data is stored in data cubes, i.e., multidimensional arrays, and retrieved from the Planetary Data Systems (PDS), NASA's long-term archive of planetary mission data. The Integrated Software for Imagers and Spectrometers (ISIS) software suite for data reduction and processing was applied to the data retrieved from the PDS. The ISIS suite includes the following steps: offset and gain corrections, dark-current subtraction, readout correction, flat-field corrections, subpixel-level co-registration, projection to Sinusoidal Equal-Area, photometric normalization (to standard viewing angles with phase = 30°, e = 0°, and i = 30°) and automated mosaicking (Gaddis et al., 1997, McCord et al., 2004). The data were converted to calibrated reflectance (I/F), as a function of wavelength, where:

I – Light intensity scattered into a particular observing direction ($\text{erg cm}^{-2} \text{s}^{-1} \text{sr}^{-1}$),

πF – Incident flux on the surface ($\text{erg cm}^{-2} \text{s}^{-1}$).

This last step of data processing enhances the ability to identify discrete clouds (Barnes et al., 2007).

5.1.2.2 Navigation and Fitting

The navigation and fitting process must be completed in an accurate fashion so that the cloud velocities can be correctly calculated, as derived wind speeds are directly impacted by the correct positioning and time tagging of the individual frames.

For the absolute image navigation and orientation, kernals – a set of elemental data files provided by the Navigational and Ancillary Information Facility (NAIF) at the Jet Propulsion Laboratory (Acton, 1996), were used to associate coordinates with each pixel of an image (Antuñano et al., 2015 , Choi et al., 2009). The navigation portion of the data processing determines the planet coordinates and illumination levels for each pixel of the VIMS cube (Sánchez-Lavega et al., 2007; Sromovsky et al., 2018). The reprojected images that were used for feature tracking and mosaic construction were oversampled at 0.1° pixel⁻¹ by using an ISIS-supplied bicubic interpolation scheme.

Using the ISIS software suite, the frames were projected into rectangular (simple cylindrical) projection when equatorward of latitude 60° . When poleward of latitude 60° ,

a polar projection scheme using an azimuthal equidistant projection, similar to technique used in Antuñano et al. (2015) was applied.

5.1.2.3 Estimations and Errors of Zonal Winds

The crux of this dissertation is to yield an increased understanding of the spatial and temporal patterns of Saturn's tropospheric wind field, along with those of the tropopause. Since there is a lack of *in situ* measurements, the data captured by the VIMS sensor was used to observe tropospheric cloud fields. These data were analyzed through the technique outlined below in a manner to extract zonal winds on a global basis.

By the strictest definition, zonal winds, or more specifically what is being sought, a zonal mean wind suggests a planet-wide longitudinal average of the winds measured at uniformly spaced intervals of time and space (Limaye, 1986). However, given the nature of the Cassini observations, the term "zonal mean" will be loosely interpreted as a result of a non-uniform sampling on both spatial and temporal time scales.

The examination of the VIMS data extended the work started by Choi et al. (2009) to now include data collected during the balances of Cassini's Prime Mission (after April 1, 2007)

and through the entirety of the Equinox and Solstice Missions, along with the Grand Finale.

Preliminary analysis of the polar regions, particularly of the Northern Hemisphere polar region, including the Hexagonal storm, was conducted by Studwell et al. (2018) and recorded for publication.

Cloud tracking analysis was conducted in a manner similar to Limaye (1986), Salyk et al. (2006), and Studwell et al. (2018). The presumption was made that the clouds can be treated as passive tracers of atmospheric mass motion. This tracking analysis can occur in two forms: manual and automated tracking. Manual cloud tracking is based on visually identifying a cloud feature and then tracking the feature in different images at different times. By determining the distance traveled and the time between the images, the zonal wind speed at that particulate latitude can be determined. The automated tracking technique works in a similar manner, but in this case, algorithms are used to track the cloud features (Limaye, 1986). Using MATLAB code previously developed within our research group, along with coordination with staff at the Space Science and Engineering Center of the University of Wisconsin, the data sets were searched to find

maximum cross-correlation between the images. Based on the longitudinal displacement of the pixels and the time elapsed between the images, the wind vectors were derived.

In general, the two aforementioned methods are used in tandem to examine Saturn's zonal winds. Del Genio et al. (2007) proposed that advantages of the automated track were that features were selected objectively and that it allowed for an efficient survey of a large number of observations. This yields a higher sample size than would be possible through manual tracking. Conversely, the weakness of an automated tracking methodology is that in areas with linear albedo patterns, it is susceptible to spurious pattern matching.

The maximal cross-correlation coefficient between the VIMS 5- μm image pairs, used in the automated tracking, generally must be greater than 0.5. In general, the automated track results performed better than the manual track because the spatial resolution for the manual tracking is limited due to the size of cloud features to be tracked. Therefore, the automated track results will be presented for most latitudes. However, the manual tracking also played a role in the analysis in that it was used to (1) validate the results of the automated tracking, and (2) fill the gaps in the zonal wind profile in locations when the cross-correlation is less than 0.5.

A source of variability in the research came from errors in the pointing knowledge of Cassini, primarily from uncertainty in the absolute location of the spacecraft and the geographical location of the cloud features (Choi et al., 2009). An error of 1-2° is approximated in the absolute location of the cloud features. While the errors of the absolute location can be on the order of ~1,000-2,000 km, the relative uncertainty in location between pixels is much smaller—small, but nonzero, absolute uncertainty. Therefore, the proposed measurements of lengths and velocities derived and used in this dissertation research will not significantly degrade in quality.

Choi et al. (2009) also noted that the feature tracker used in their analysis attempted to measure both zonal (wind component, along the local parallel of latitude) and meridional (wind component along the local line of longitude) velocities. However, this research found no evidence of meridional motions, either synoptic or regional-scale was detected. Additionally, given the resolution limits of the VIMS, this sensor was incapable of tracking local meridional motions. Therefore, Choi et al. (2009) will be used as a guideline in that this dissertation research only focused on zonal motion.

Additional uncertainty that was accounted for in the analysis was the rotation period of Saturn. This was a key factor in the determination of the atmospheric zonal wind

velocities since the period is used to establish the motion of a reference frame. While measurements from the Voyager mission suggested a rotation period of 10h 39m 24s (Desch & Kaiser, 1981), data collected during the Cassini mission pointed to a more rapid rotation period.

Observations presented in Anderson and Schubert (2007) showed a rotation period of 10h 32m 35s, while work conducted by Read, Conrath, et al. (2009) yielded a period of 10h 34m 13s. For this research, the approach established in Studwell et al. (2018) of averaging the two periods generated through the Cassini research will be used for the determination of wind profiles, 10h 33m 24s.

Figure 5.3 shows a comparison of a global zonal wind profiles using both VIMS and ISS data for the Desch and Kaiser (1981) rotation period compared with the value that was established in Studwell et al. (2018). A key point is the lack of easterly jets using the Desch and Kaiser (1981) period of rotation. In this case, there are implications regarding the both large-scale mechanics of the zonal jets and their maintenance, while there would also be mesoscale implications regarding energy transfer and dissipation, along with eddy maintenance.

5.2 Previous Research – VIMS

The ISS and CIRS data collected from Saturn's upper troposphere, tropopause, and into the stratosphere has been examined in depth with regards to zonal wind patterns. However, a global overview of VIMS data has not been conducted as thoroughly; such an analysis requires pole-to-pole observations using high spatial resolution data.

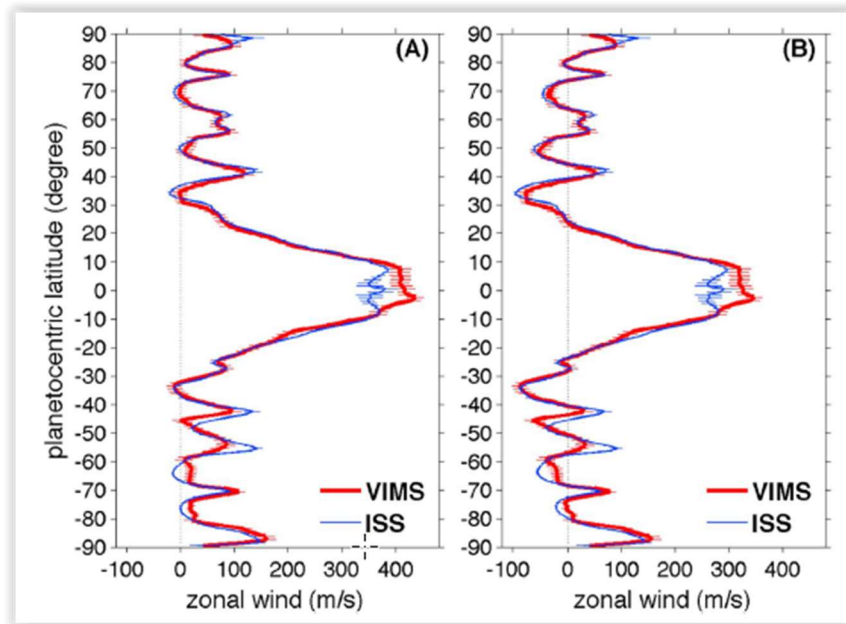


Figure 5.3. Comparison of global zonal wind data, derived from both VIMS and ISS data, for two different rotational period estimates. Image (A) shows the calculated zonal wind speeds, based upon Desch and Kaiser (1981) rotation period estimate. Image (B) shows calculated zonal wind speeds, based upon Studwell et al. (2018) rotation period methodology. The horizontal lines represent error bars. The global profile of the VIMS 5- μm zonal winds is largely based upon 2015-2017 observations (Studwell et al., 2018). The data poleward of $\sim 89^\circ\text{S}$, were specifically from 2016 (Dyudina et al., 2019). The global profile of the ISS zonal winds is primarily based up 2004-2008 data (García-Melendo et al., 2011). The data poleward of 83°N (Antuñano et al., 2015) were from 2013 (Studwell et al., 2018).

Similarly, a comprehensive review of temporal patterns of the mid-tropospheric winds using the VIMS data has not been pursued either, as long-term data sets are not available. While previous VIMS research was conducted in a disjointed fashion, early indications of seasonal patterns of the deep tropospheric winds emerged from these studies (e.g., Baines et al., 2005, 2009; Choi et al., 2009; Dyudina et al., 2009; Li et al., 2016).

The first published results on the examination of the VIMS data as applied to tropospheric zonal winds was Baines et al. (2005). This research broadly focused on both Saturn and Titan, examining the atmospheric structure and the dynamical processes in the atmosphere. This leading-edge work noted the advantages of using the VIMS data to observe clouds backlit by the infrared radiation being emitted from the 5,000-mbar level. These advantages include: backlit clouds are of a discrete nature and can be differentiated for wind speed calculation; identification of backlit clouds can occur in both day and nighttime images; and that backlit clouds persist for many days, allowing for several sets of zonal wind calculations to be carried out.

Baines et al. (2005) yielded results of $\sim 390 \pm 50 \text{ m s}^{-1}$ for the zonal tropospheric winds within the Southern Hemisphere's equatorial jet. This intensity compared favorably with the Voyager measurements (Smith et al., 1981, Ingersoll et al., 1984), but were

approximately 120 m s^{-1} less than the values reported in Sánchez-Lavega et al. (1999), which used both ground-based telescopes and HST data in their research. Baines et al. (2005) acknowledged an uncertainty regarding what cloud height levels were being examined in the Voyager data. Despite the uncertainty of the cloud heights in the earlier research referenced by Baines et al. (2005), variations in zonal wind measurements at different cloud levels through the troposphere provided the required data for the determination of zonal wind shear.

Baines et al. (2009) examined polar cyclones and the hexagonal storm using the VIMS data. The investigation of the polar cyclones in the tropospheric levels of the Northern and Southern Hemispheres showed that cyclonic vortices were present with winds in excess of 135 m s^{-1} in the NH, while the SH jet was ~ 155 to 195 m s^{-1} . The large range of uncertainty for the SH jet was due to the sparsity of data. However, the higher SH zonal wind speed values were consistent with other research conducted with data from the ISS (Dyudina et al., 2009) and the CIRS (Fletcher et al., 2007).

Additionally, Baines et al. (2009) examined tropospheric zonal winds within the hexagon centered at approximated 76° N . The results were consistent with the idea that the hexagon remains nearly stationary and is a westward-propagating Rossby wave with a

maximum wave speed $\sim 125 \text{ m s}^{-1}$ in the lower troposphere. Comparisons to Voyager data from over thirty years' prior indicated the 2008 zonal wind speeds were $\sim 25 \text{ m s}^{-1}$ stronger, implying there is temporal variability. Finally, Baines et al. (2009) showed clouds evident in visible images at the 300- to 500-mbar level were well-correlated with clouds represented in the 5- μm data (1,000- to 3,000-mbar level), leading to the theory there is little VWS within the hexagonal structure through the troposphere.

Choi et al. (2009) examined VIMS 5- μm data, which encompassed the time frame from Cassini's arrival in July 2004 through March 2007. This research focused on cloud features and their morphologies, in addition to examining trends in the atmospheric zonal jet structure and their changes over time. The results indicated the shape of the zonal wind profiles remained broadly consistent between the Voyager-era measurements and into the early years of the Cassini mission.

This research also focused upon specific features in the equatorial region, and compared favorably with results in Baines et al. (2005). A broad equatorial jet was noted in these results from Choi et al. (2009), along with comparable zonal wind shear values. However, two issues mentioned in this research offer a need for caution in their interpretation. First, there are uncertainties about which pressure level the Voyager data was observing.

Additionally, wind speeds were estimated to be in excess of 500 m s^{-1} ; however, these were generated from the manual cloud tracking of a small set of clouds. The movement of this cloud cluster may represent localized flow and not the zonally-averaged mean. Despite these ambiguities, Choi et al. (2009) posited with a level of confidence that the VIMS data indicated that zonal winds exceeded ~ 400 to 450 m s^{-1} within the equatorial jet.

Dyudina et al. (2009) examined the polar vortex over the Southern Hemisphere using VIMS data along with ISS and CIRS images. Consistent with Baines et al. (2005), this research shows the peak tropospheric zonal wind speeds from the 1,000- to 3,000-mbar level within the south polar vortex (SPV) at about 87°S , was about $170 \pm 20 \text{ m s}^{-1}$. Additional conclusions from this research are presented in Section 3.4 in association with a review of the ISS data used in this research.

Li et al. (2016) compared the deep tropospheric zonal winds measured by VIMS in 2015 for the Northern Hemisphere's tropics region north into the mid-latitudes (0° N to 30° N) to the 2004 through 2007 results in Choi et al. (2009). From approximately 8°N and extending poleward, the zonal wind measurements were relatively close, though the 2015 measurements were greater than the earlier values. However, in the equatorial region,

the 2015 winds were significantly lower than the 2004 through 2007 values with the largest departure of $\sim 170 \text{ m s}^{-1}$ seen at about 3° N . It must be noted these results were offered as preliminary, and it is one of the goals of my research to resolve this issue.

5.3 VIMS Analysis: Zonal winds below the visible cloud level

Given the study's focus on the spatiotemporal variation of Saturn's atmosphere, this section will examine VIMS data, searching for trends in zonal wind patterns through the deeper troposphere. Additionally, the task will compare the two sets of tropospheric winds, collected by both the ISS and VIMS, to review the changes in their vertical profile. Finally, the task will examine the atmospheric structure in and around the North Pole's hexagonal storm.

Figure 5.3 shows a comparison of the VIMS $5\text{-}\mu\text{m}$ data, which captures the zonal winds at the 2,000-mbar level, to the ISS continuum band data, which shows the 300- to 500-mbar winds. It should be noted that the VIMS (2015-2016) and ISS (2004-2008) data are from different time periods. However, previous analysis (e.g., García-Melendo et al., 2011; Li et al., 2011; Sánchez-Lavega et al., 2016) indicated that the zonal winds recorded by the ISS did not change significantly during the Cassini era. As noted previously, studies on the temporal variations of the VIMS zonal winds are incomplete. Therefore,

the possibility that the difference between the VIMS and ISS zonal wind profiles is due to their evolution over time cannot be excluded; however, it is more likely that these differences are due to VWS within the Saturn's troposphere.

A global-scale constancy is noted in Figure 5.5 between the VIMS and ISS wind profiles, implying that the 2,000-mbar zonal winds have a similar structure to those at the 300- to 500-mbar level. Conversely, at some latitudes, there are significant differences with variances greater than the uncertainty levels, signifying that they are meaningful from a statistical standpoint. In the equatorial region, ranging from 5°N to 5°S, the VIMS winds are estimated to be stronger than the ISS winds by $\sim 50 \text{ m s}^{-1}$. Earlier VIMS measurements in this region from 2004-2008 (Choi et al., 2009), which are roughly from the same time period with the ISS wind profile in Figure 5.3, suggest that the VIMS-level winds could have been even stronger during this earlier time frame. Therefore, it is proposed that in equatorial region, the 2,000-mbar level zonal winds are at least 50 m s^{-1} greater than those at the 300- to 500-mbar levels, which is consistent with previous research (Sánchez-Lavega et al., 2016).

As noted above, the VIMS observations point to an atmospheric structure where the equatorial zonal winds increase when descending from the 300- to 500-mbar level, deeper

into the troposphere. Given this information, the variation of the VWS between these two levels was of interest and examined. Previous studies examined vertical temperatures derived from radiance data collected by the CIRS (e.g., Flasar et al., 2005; Li et al., 2008), ranging from the 300- to 500-mbar level, associated with the visible clouds, outward to the tropopause, ~50 mbar. These analyses indicated that the equatorial zonal winds weaken as they progress outward in the upper troposphere, towards the tropopause. This conclusion was also supported by Li et al. (2011), which examined data collected by the ISS with its MT3 filter.

By compositing this set of analyses together, it can be demonstrated the equatorial zonal winds increasing as one descends from the tropopause and deeper into the troposphere to the 2,000-mbar pressure level. This tropospheric vertical wind structure is qualitatively similar to the equatorial structure of Jupiter, which was measured by both the Galileo probe (Atkinson, 2001; Atkinson et al., 1996, 1997, 1998) and the Cassini mission (Flasar et al., 2004; Li et al., 2006; Simon-Miller et al., 2006). Jupiter's zonal wind structure in the equatorial region also increased as one transits downward into the troposphere, increasing from the tropopause at ~100 mbar to the ~5,000 mbar pressure level.

Examination of the VIMS profile in Figure 5.5 also shows an asymmetric configuration in Saturn's equatorial winds, along the north-south axis. This pattern is similar to the equatorial zonal winds in Jupiter's troposphere, at the visible cloud level, which may yield Rossby wave activity in Jupiter's NH that in turn causes plumes in this region (e.g., Allison et al., 1995; García-Melendo et al., 2011). A pair of VIMS maps, shown in Figure 5.4, illustrates a semiregular spacing of longitudinal features, between the equator and $\sim 10^\circ\text{N}$. These features may possibly be responsible for the latitudinal asymmetries noted in the VIMS NH equatorial winds, though further analysis is required.

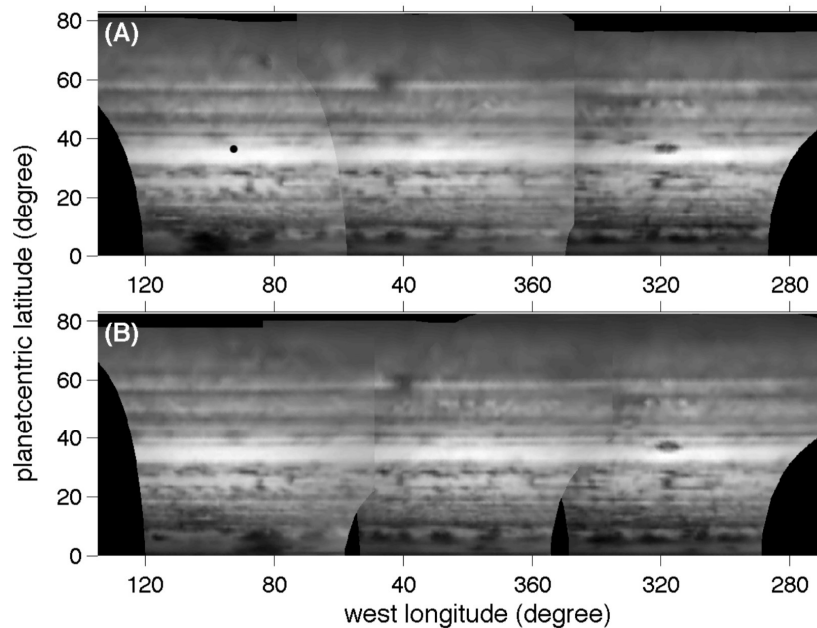


Figure 5.4. Examples of 5- μm VIMS cloud imagery. These raw images were taken in 2015 with spatial resolution of $450 \text{ km pixel}^{-1}$. These two images (Panels A and B) were taken ~ 10 hours apart; therefore, they are suitable for the determination of zonal wind speed measurements (Studwell et al., 2018).

Figure 5.5 also demonstrates that the VIMS and ISS zonal winds are essentially consistent in a range extending from 40°S to 25°N, except for in the equatorial region from 5°S to 5°N. This analysis used the rotational period derived in Studwell et al. (2018) and shows that in the mid- and high latitudes that the magnitude of the VIMS zonal winds are generally smaller than those measured by the ISS in both the easterly (e.g., 77°S, 61-64°S, 34°S, 50°N, and 69°N) and westerly jets (e.g., 55°S, 43°S, 42°N, 61°N, and 87-89°N). Conversely, the easterly jet centered from 44-48°N is stronger at the 2,000-mbar level and weakens as it extends upwards to the 300- to 500-mbar level. Finally, the westerly jets located near 86°S, 70°S, and 76°N and the easterly jet around 79°N have roughly the same magnitude at both the VIMS and ISS-detected levels. The consistent westerly jet noted near 76°N has roughly the same position with the polar hexagon, which implies that it is a propagating Rossby wave (Allison et al., 1990; Baines et al., 2009).

A review of Figure 5.5 also illustrates that the majority of the zonal jet located in the mid- to high latitudes are stronger at the 300- to 500-mbar level, weakening as one descends deeper into the troposphere, reaching the 2,000-mbar level. This resultant VWS in the mid- to high latitudes is oriented opposite than the VWS observed in the equatorial region (5°S to 5°N), where the deep tropospheric zonal winds are stronger than those noted at

the visible cloud level, ranging from 300 to 500 mbar. While it is possible that these differences in the zonal winds between the two pressure levels in the mid- to high latitudes may be a result of temporal variations, previous research of the ISS winds (García-Melendo et al., 2011; Li et al., 2011 and; Sánchez-Lavega et al., 2016), along with our examination for any changes in the VIMS zonal winds through most of the Cassini era (Figure 5.5) suggest that both the ISS and VIMS zonal winds are probably consistent over time at most latitudes.

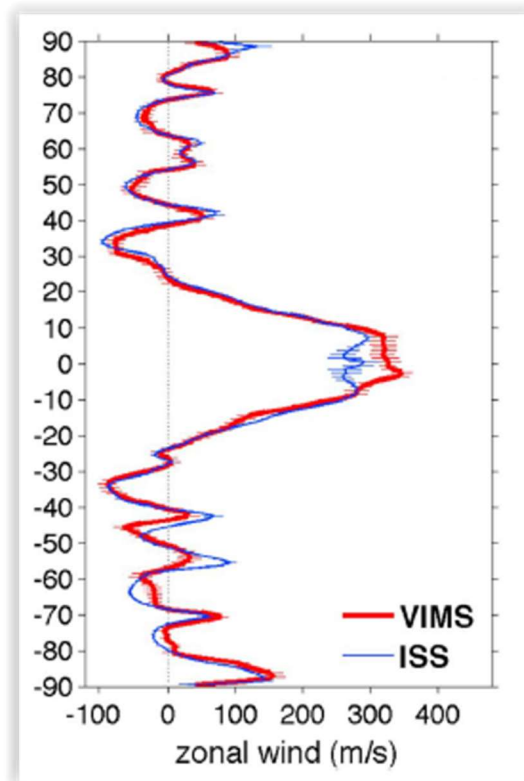


Figure 5.5. Global zonal wind data derived from both VIMS and ISS data. The horizontal lines represent error bars. The ISS data are representative of the upper troposphere, ~300 to 500 mbar, while the VIMS data are from the deep troposphere, ~2,000 mbar (Studwell et al., 2018).

Based on the earlier analysis, this allows for the investigation of the atmospheric stability of the Saturn's troposphere. For a barotropic atmosphere where the zonal winds are the dominant pattern, the total vorticity can be defined as the sum of the planetary vorticity, i.e., Coriolis parameter f , and the relative vorticity of the zonal winds, $-U_y = -\partial U/\partial y$. The barotropic stability is then expressed as the gradient of the total vorticity, $\beta - U_{yy}$, where $\beta = \partial f/\partial y$ and $-U_{yy} = -\partial^2 U/\partial y^2$. The barotropic stability criterion states that flows are stable when $\beta - U_{yy} > 0$. Conversely, when $\beta - U_{yy} < 0$ and violates the criterion, perturbations, e.g., waves, vortices, eddies, and subsequent turbulence, may develop.

Delving deeper into this thought process, the meridional gradient of the planetary vorticity is positive in all locations. The term U_{yy} represents the gradient of the relative vorticity, $-U_y$, and characterizes the curvature of the zonal jets. By mathematical definition, only easterly jets can have positive curvature, i.e., $U_{yy} > 0$, so only in those flow regimes can the barotropic stability criterion possibly be violated ($\beta - U_{yy} < 0$). Figure 5.6 shows parabolas with curvature β and are centered on the easterly jets. (The methodology was first used for a similar analysis of Jupiter's zonal winds in Li et al.,

2004.) In the visualization, when the easterly jets are sharper than the parabolas, i.e., where $U_{yy} > \beta$, the jets violate the barotropic stability criterion.

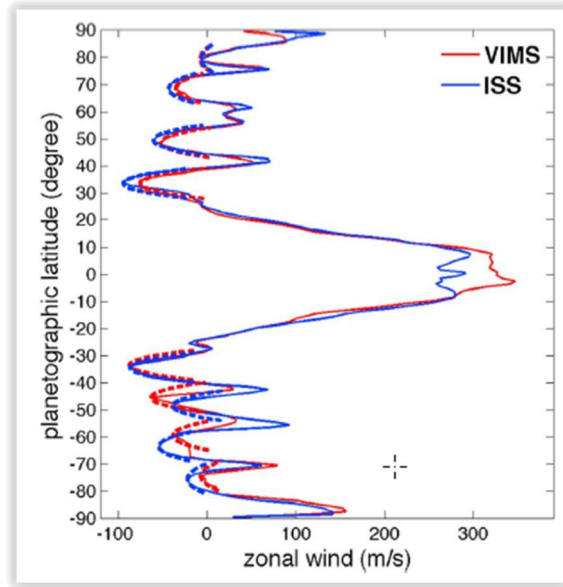


Figure 5.6. Curvature, U_{yy} , of the zonal wind profiles, compared to β . The parabolic curves are defined by $U_{yy} = \beta$ and are centered along the maxima of the westward jet. The blue and red dashed parabolas are for the ISS and VIMS wind profiles, respectively. The zonal wind flow violates the barotropic stability criterion at the latitudes where the measured wind profiles lies into the red parabolas (Studwell et al., 2018).

Using this methodology to examine the ISS zonal wind data in Figure 5.6, the easterly jets identified near 64°S , 33°S , 34°N , 50°N , and 69°N are slightly sharper than corresponding parabolas, which have a curvature, β . This analysis implies that these five jets are marginally unstable. Additionally, there are three other easterly jets noted at the 300- to 500-mbar level, which are centered at 77°S , 48°S , and 79°N and are much sharper than the

corresponding parabolas. By virtue of the difference in sharpness to the parabolas, these three jets are very unstable.

Through the extent of Saturn's troposphere that was just examined, all of the easterly jets are barotropically unstable. This detail helps to elucidate why Saturn's vortices are situated around the easterly jets (Trammel et al., 2014, 2016). Figure 5.6 shows that a majority of the deeper tropospheric easterly jets have a similar sharpness compared to those noted near the visible cloud layer. The notable exceptions are located around 46°S and 59°S, which have a higher sharpness, i.e., more unstable, at the 2,000-mbar level than they are at the 300- to 500-mbar level.

At most latitudes, it is possible that Saturn's zonal winds are stable over time, even though they are in exceedance of the barotropic criterion near the peaks of the easterly jets. This likelihood implies that these zonal winds are baroclinic (Li et al., 2004). The baroclinicity is related to the VWS; therefore, the vertical wind profiles from the two different pressure levels (Figure 5.6) can be used to estimate the VWS and baroclinic stability (Holton, 2004). The value of VWS found within the zonal winds will be used to

evaluate the Richardson number, which is related to baroclinic instability, atmospheric stratification, and the development of turbulence (e.g., Allison et al., 1995; Holton, 2004).

The Richardson number can be shown in (23) as

$$Ri = \frac{N^2}{(dU/dz)^2} \quad (23)$$

where N is the Brunt–Väisälä (or buoyancy) frequency and dU/dz is the vertical shear of the zonal winds.

The static stability, N^2 , can be calculated from the Saturn's temperatures retrieved from the Cassini CIRS (Figure 5.7, Panel A). The CIRS data that was analyzed in this research topic from 2008 and also used in a study by Fletcher et al. (2010). This temperature data is thorough above the 500-mbar pressure level (Flasar et al., 2004; Fletcher et al., 2010), so N^2 can be computed at the 500-mbar level, which will represent the static stability in the pressure range between the 300- to 500-mbar and the 2,000-mbar pressure levels.

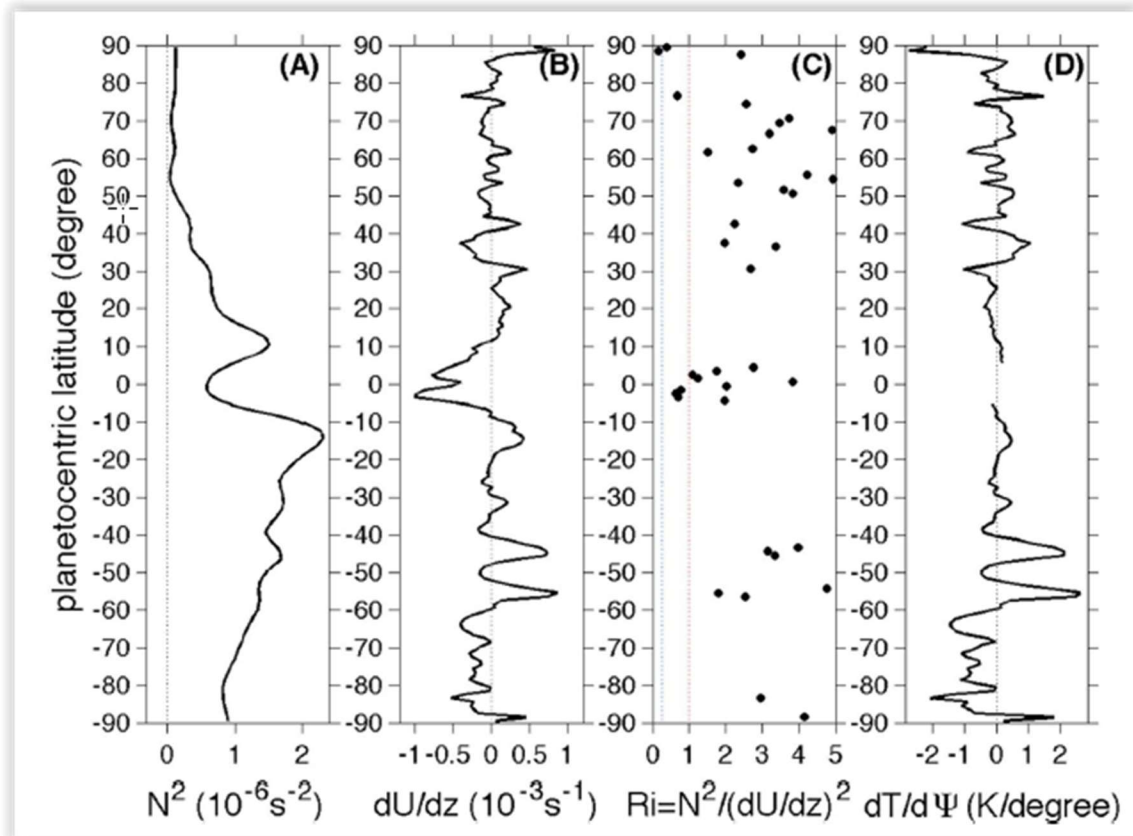


Figure 5.7. Atmospheric parameters calculated from ISS and VIMS winds, primarily from 2015 through 2017. Frame A is static stability, N^2 ; Frame B shows the vertical shear of the zonal winds, dU/dz ; Frame C portrays the Richardson number, Ri , where the blue and red vertical lines represent $Ri = 0.25$ and $Ri = 1$, respectively; and Frame D depicts the meridional temperature gradient, $dT/d\Psi$. Only values of the Richardson number of less than 5 are plotted in Frame C. At some latitudes where the VWS is very small, the resulting value of Ri are extremely large, i.e., $> 1,000$. In Frame D, there is a narrow band of latitude in the equatorial zone, 5°N to 5°S , in which the standard form of the thermal wind equation does not apply and subsequently, these values of $dT/d\Psi$ are not resolvable (Studwell et al., 2018).

In order to calculate the 500-mbar static stability, a central difference scheme will be applied to 470- and 550-mbar temperature data since they are the two levels closest to the 500-mbar pressure level. From Figure 5.6, the difference between the VIMS and ISS-level

zonal winds can be used to estimate the VWS, dU/dz (Figure 5.7, Frame B). Based on these two variables, the 500-mbar static stability and the VWS through this region of the troposphere, the Richardson number can be calculated (Figure 5.7, Frame C).

The thermal wind relationship, which was derived, validated and applied in Chapters 3 and 4, can also be used to determine the meridional temperature gradient, $dT/d\Psi$ between the 300- to 500-mbar and 2,000 mbar pressure levels. For this application, the thermal wind relationship can be shown as

$$\frac{dU}{dz} = \left(\frac{-\rho Rg}{fP} \right) \left(\frac{dT}{r d\Psi} \right) \quad (24)$$

where ρ is density, P is pressure, R is Saturn's gas constant, r is Saturn's radius, and Ψ is latitude. Through the algebraic manipulation of (24), the $dT/d\Psi$ term can be shown as

$$\frac{dT}{d\Psi} = \left(\frac{-rfP}{\rho Rg} \right) \left(\frac{dU}{d\Psi dz} \right). \quad (25)$$

At the 1,000-mbar level, the density is estimated to 0.19 kg m^{-3} , which was obtained from the NASA Space Science Data Coordinated Archive, and represents the average density between the two pressure levels of interest. Through the application of (25), the estimated meridional temperature gradient $dT/d\Psi$ is presented in Figure 5.7, Frame D. It must be noted that the calculation of the vertical wind shear and the other associated parameters shown in Figure 5.7 are rough estimates because the initial assumption that the zonal

winds between the 300- to 500-mbar and the 2,000-mbar pressure levels change in a linear manner.

Reviewing Figure 5.7, Frame A, it is noted that on a global basis, the static stability is positive everywhere, suggesting that this region of the troposphere is convectively stable. Additionally, this figure shows that the static stability is greater in the SH than it is in the NH. Since the temperatures for computing N^2 was collected in 2008 (Fletcher et al., 2010) when it was summer in the SH. During the summer, the higher level of solar insolation yields a warmer upper atmosphere, thereby producing a larger value of static stability. Conversely, the minimum of static stability located near the equator implies that this region would be favorable for convection.

With regards to the VWS, it is shown in Figure 5.7, Frame B that the equatorial region primarily experiences a negative vertical shear of the zonal winds, specifically, the zonal winds increases as one proceeds deeper into the troposphere. Poleward of the equator, a mix of positive and negative VWS is noted, particularly in the mid-latitudes, along with near the North and South Poles. Additionally, Figure 5.7, Frame C shows values for the Richardson number, R_r , of less than 1 in the equatorial region and generally poleward of 80°N, which is one of the needed conditions for baroclinic instability (Allison et al., 1995;

Holton, 2004). With values of R_i of less than 0.25 near the North Pole, leading to the supposition that the VWS of the zonal winds in the region are probably strong enough to sustain turbulence.

Figure 5.7, Frame D presents the estimated meridional temperature gradient, $dT/d\Psi$, through the troposphere, which is proportional to the VWS of the zonal winds, through the thermal wind equation, specifically (25). Based on this, the implication is that regions with strong VWS, either positive or negative, also have strong temperature gradients. In several locations (e.g., 56°S, 45°S, and 89°N) across Saturn, $dT/d\Psi$ can reach 2 K per degree of latitude. However, an exception to this relationship is in the equatorial region, where the temperature gradients are small, despite the predominantly negative VWS persisting. The primary reason for this atmospheric structure is because the Coriolis force is diminishingly small as one approaches the equator, so the meridional temperature gradient must be small to keep its balance through the thermal wind relationship.

Finally, this analysis gave an initial opportunity to examine the temporal variations of the VIMS zonal winds, specifically poleward of 60° latitude in both the Northern and Southern Hemispheres. Figure 5.8 shows the 2,000-mbar zonal winds in both polar regions, based on Cassini observations from 2016 and 2017. These more recent

measurements were compared with similar data from 2006 and 2008 (Baines et al., 2009, Dyudina et al., 2009). This figure illustrates that the differences observed in the zonal winds between these periods of study are smaller than the measurement uncertainty for most latitudes; the exception is noted in the NH, poleward of 85°N. Between 2008 and 2017, the zonal jet centered about ~88°N weakened significantly from $135 \pm 7 \text{ m s}^{-1}$ to $91 \pm 12 \text{ m s}^{-1}$, a reduction of $33 \pm 12\%$ in that ten-year period.

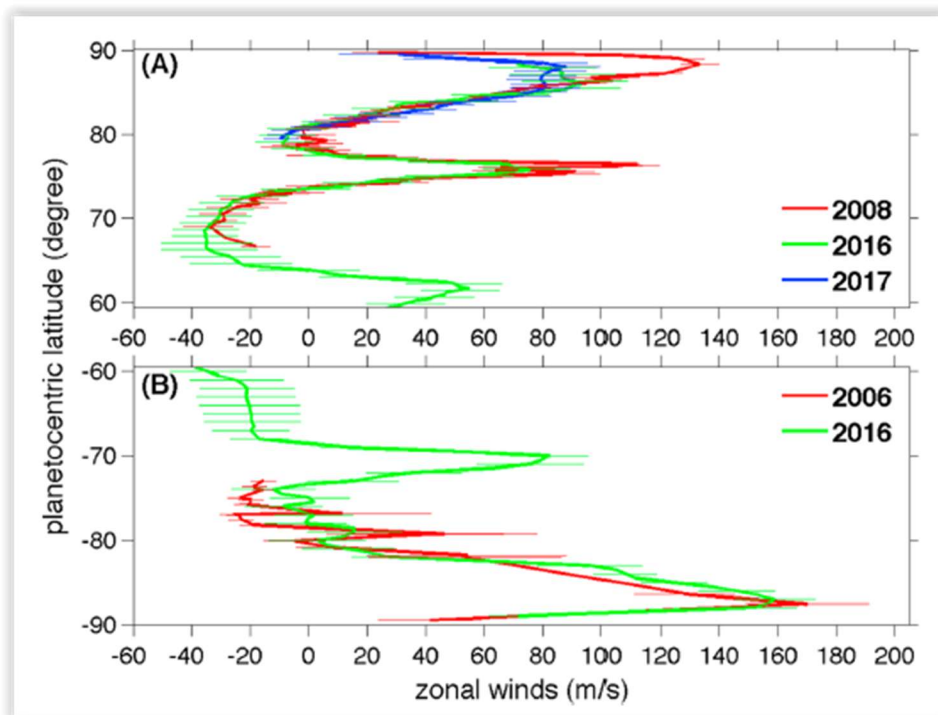


Figure 5.8. Comparison of the VIMS 5- μm zonal winds across Saturn's polar regions, ranging from 2008 through 2017. Panel A shows the results from the North Pole, while Panel B is from the South Pole. The 2006 SH zonal wind data was from Dyudina et al. (2009) and the 2008 NH data was from Baines et al. (2009). The horizontal lines are error bars. (Studwell et al., 2018)

5.4 Conclusions

This Chapter reviewed the technical specifications and applications of the VIMS from the Cassini mission. Additionally, an overview of previous research and the advances of the planetary studies and specifically, our understanding of Saturn's deep tropospheric zonal winds was offered.

This task presented the first global profile of the 2,000-mbar zonal winds; the comparison of the VIMS and 300- to 500-mbar level zonal winds from the ISS suggest a general consistency of structure on a global scale. However, the differences between the wind profiles are also notable, also on a global basis. In the equatorial region, $\sim 5^{\circ}\text{S}$ to $\sim 5^{\circ}\text{N}$, the zonal winds show an increase of at least 50 m s^{-1} as one descends from the 300- to 500-mbar level downward to the 2,000-mbar level in the deeper troposphere. Conversely, the analysis showed a decrease in the zonal wind speeds as one moves deeper in the atmosphere in most of the zonal jets in the mid- and high latitudes in both hemispheres.

The zonal winds at the VIMS and ISS pressure levels were also applied to an examination of Saturn's atmospheric stability. This analysis suggested that most of the zonal jets located at these two pressure levels are barotropically unstable. Through an investigation of the Richardson number, it is proposed that the one necessary condition, significant

vertical shear of the zonal winds, for the baroclinic instability is satisfied in some locations. Finally, a version of thermal wind equation was applied to zonal winds between the 300 to 500-mbar and the 2,000-mbar pressure levels to show that the meridional temperature gradient can exceed 2K per degree of latitude at a few locations at the mid- and high latitudes.

The VIMS observations from an over decade-long period in Saturn's polar regions were used to examine their temporal variations. This research showed that 2,000-mbar zonal winds were fairly consistent from 2006 to 2017 in both polar regions; the exception was poleward of 85°N, where a westerly jet decreased $\sim 44 \pm 14 \text{ m s}^{-1}$ from 2008 through 2017.

Finally, this chapter provide an initial systemic analysis that characterized the spatiotemporal variations with Saturn's atmosphere, specifically the zonal winds, with long-term (2004-2017) multi-instrument observations, i.e., CIMS, ISS, and VIMS. While the global zonal wind profile using the 2,000-mbar zonal winds from 2015 through 2017, other time periods were examined. Based on the existing VIMS data set, additional global profiles can be developed and applied to the research of the troposphere, especially the temporal variations of these deep zonal winds. Combining this insight with the long-term investigations of the CIRS and ISS data, it will lead to a more complete picture of the

atmosphere's vertical structure, from the deep troposphere, across the tropopause, and out into the stratosphere. This achievement would aid to further the advancement of the planetary sciences.

Chapter 6 (Task 4): Analysis of Saturn's Great White Storm of 2010

Convective activity plays an important role in energy transport and balance on a regional and global scale across all atmospheres. Earth experiences millions of storms annually with a vast majority being mesoscale phenomena. Synoptic storms, such as tropical cyclones, are less frequent but more impactful, both on the Earth's atmosphere and its population. Similarly, small-scale convective storms occur on an occasional basis on Saturn, while synoptic-scale events, termed "great white storms", have gaps in their development measured in decades. These GWS are the largest convective cumulus storms in the Solar System, can generate bright clouds, which will cover a large fraction of the longitudinal circle, or as one did in 2010 and 2011, encircle the entire planet. From north to south, this storm extended across ~10,000 km within the first month and ~21,000 km at the largest point (Fischer et al., 2011; Sánchez-Lavega et al., 2011). Its full zonal length was estimated to be ~280,000 km (Sánchez-Lavega et al., 2012)

While these storms are rare, common traits are noted among them, including rapid growth from a single outburst point, along with expansion in the zonal direction. Additionally, the visual appearance is manifested as a complex pattern of the bright white clouds in a large latitudinal band and spread over top of Saturn's typical banded

appearance. Based on our current historical record, the GWS have only occurred in the NH, alternating between the equatorial region and mid-latitudes (Sánchez-Lavega, 1994). Atmospheric modeling has been conducted with regards to these synoptic-scale storms found on the gas giants are due to moist convection induced by water (Hueso & Sánchez-Lavega, 2004). Prior to the 2010 GWS, analysis of these events was limited to remote observations, either from Earth or Earth's orbit. With the Cassini mission on station, this allowed for observations to be made and results gathered to verify previous and on-going modeling efforts.

Prior to the development of the GWS in December 2010, it was theorized that these storms developed approximately once per Kronian year, ~30 Earth years. There had been six GWS observed on Saturn since 1876 with the last one observed prior to the 2010 GWS occurring in 1990, all of which occurred in the Northern Hemisphere (Li & Ingersoll, 2015; Sánchez-Lavega et al., 2012). It was also noted in Sánchez-Lavega et al. (2012) that there have been three other events, which were similar to the GWS phenomenology, which have occurred either in the SH or along the equatorial zone. However, these three systems did not completely match other descriptions of the GWS and have been classified as "minor", most likely, less energetic versions of a GWS.

With regards to the historical record, the 2010 GWS is considered to have been “early”; this GWS has also been well-analyzed with observations from Terrestrial-based telescopes, along with the Cassini spacecraft. These previous studies, along with the analysis conducted with this dissertation task, have enriched our knowledge of Saturn’s giant storms.

For several other reasons, the 2010 GWS was notable. Historically, these episodes have a duration of 25 to 55 days, while the 2010 storm persisted for ~195-200 days (Sánchez-Lavega et al., 2012, Sayanagi et al., 2013). Additionally, the associated bright cloud tops of the 2010 GWS expanded to the equator (southerly), but their poleward (northerly) expansion was limited. With this poleward restriction, as the storm’s trailing anvil circumnavigated the planet, its northern edge passed over the southern side of the actual storm (García-Melendo et al., 2013; Sánchez-Lavega et al., 2011; Sayanagi et al., 2013). This task will examine this phenomenon, along with the potential reason for this asymmetric expansion.

This storm’s occurrence near 35°N places it in a region of more frequent storm development, both on the meso- and synoptic scale and is collocated with westerly jet flow. Previous mesoscale storm development was noted in this region during the

Voyager flybys in 1980 and 1981. Additionally, smaller, though still synoptic-scale, development was noted near 35°S, in a region that had been dubbed “Storm Alley.” These storms were also presumed to be convective in nature with lightning detected by the Radio and Plasma Wave Science (RPWS) sensor. These storms also developed an associated AV but an analysis of the areal extent of these systems, along with the frequency and intensity of the lightning, showed these SH storms to be an order of magnitude smaller than the GWS (Sayanagi et al., 2013).

6.1 Previous Research – Great White Storms

With improvements in instrumentation and the good fortune of having Cassini in orbit around Saturn during the most recent GWS, the 2010 event is the best analyzed occurrence of the Great White Storms. Coupled with analysis of the previous events, the scientific community has had the opportunity to further our understanding of these storms, along with their interactions with the surrounding environment (e.g., Achterberg et al., 2012; Fischer et al., 2011; García-Melendo et al., 2013; Hall, 1877; Li & Ingersoll, 2015; McKim, 2011; Sánchez-Lavega, 1994; Sánchez-Lavega et al., 2011, 2012, Sayanagi et al., 2013).

In Chapter 2 of this dissertation, it was noted that Asaph Hall made the first recorded observations of the GWS; Hall (1877) documented that the bright spot was located, "...north of the Ring, nearly midway of the disk in the direction of the circle of declination." This description locates this storm in the equatorial zone as does a drawing (Figure 6.1) by D.W. Edgecomb from December 10, 1876 (McKim, 2011); Edgecomb's observational data was factored in Hall's determination of the Saturn's rotational period.

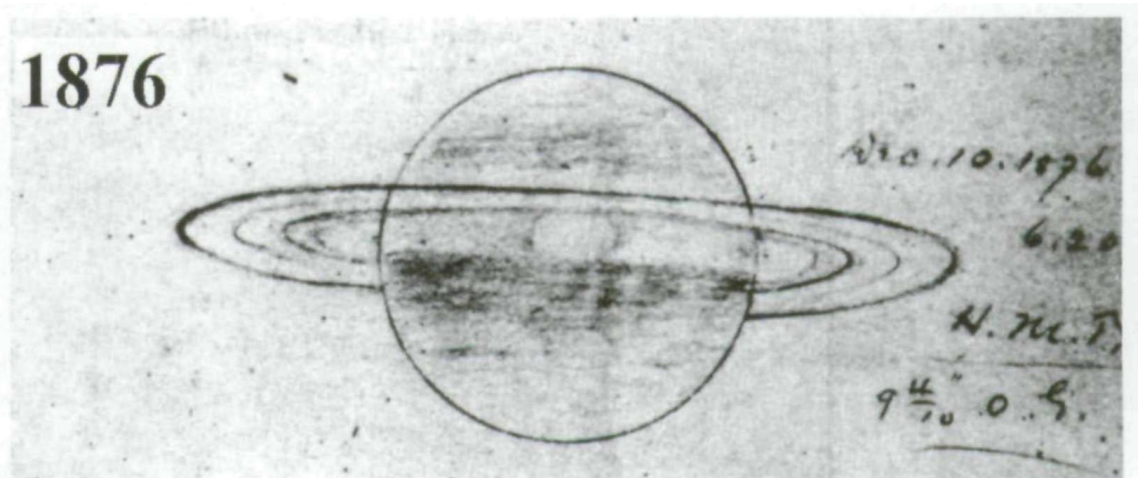


Figure 6.1. First known drawing of 1876 Great White Storm by D.W. Edgecomb, Connecticut, USA on December 10, 1876, 6:30 PM local time. Edgecomb was using a 9.4-inch (249 mm) Alvan Clark refractor (McKim, 2011).

The 1903 GWS was first observed by E.E. Barnard of the Yerkes Observatory in Williams Bay, Wisconsin on June 24 ("Scientific Notes and News", 1933) using a 40-inch refracting telescope, which is still in use at this facility. It was independently confirmed by British astronomer W.F. Denning a few days later. This storm was unique, compared to 1876 and 1933 GWS, in that it was located in the mid-latitudes, $\sim 36^{\circ}\text{N}$, versus these other two being

in the equatorial zone. Over ten years later, Denning used his observational data to follow in Hall's footsteps in an attempt to establish the rotation period of Saturn (McKim, 2011). These calculations yielded a mean period of 10h 37m 56.4s (Our Astronomical Column, 1918), which was substantially closer to modern estimates than achieved by either Herschel or Hall.

On August 3, 1933, Will Hay, a London music hall comedian and amateur astronomer, made the first recorded observation of the 1933 GWS with a six-inch refracting telescope in Norbury, England. Approximately 27 hours later, it was independently noted by John Willis of the USNO on the morning of August 5; Willis' notes reported that a white spot had suddenly appeared on the equator of Saturn. By the evening of August 5, he estimated it to be large enough to engulf an object that was twice the diameter of Earth, larger than the Great White Storm of 1876. It is notable that Willis made his observations of the 1933 GWS through the same 26-inch lens that Hall used in 1876. Willis also tracked the GWS over the next several evenings in order to verify the rotation period estimate derived by Hall 57 years prior; he found that GWS revolved around Saturn in about the expected time ("Scientific Notes and News", 1933).

Prior to the 2010 GWS, the most recent storm was in 1990 and the spatiotemporal trends in its development were examined in Sánchez-Lavega (1994). The images used in this analysis were captured by both ground-based telescopes and the HST. As noted previously, historically, the GWS have developed in the NH, though at different latitudes and in regions with dissimilar zonal wind velocities and ambient vorticity. Despite these differences, all five of the previous GWS have shared a common characteristic cloud and evolution patterns. Conversely, regardless of the region of their development, whether, equatorial, mid-latitude, or subpolar, there are variance in the storm's growth, which were theorized to be related to differences in subjacent wind fields in which they were embedded.

The timeline of the typical GWS evolution presented in Sánchez-Lavega (1994) focused on equatorial storms, primarily the 1933 GWS, which was well-documented in photographs, along with the 1990 storm. The first stage was termed "onset", which manifests with the rapid development of a very bright spot in or near a high albedo zone. The initial horizontal growth noted in the first few days, points to an intrinsic growth originating from the source region with expanding velocities $V \sim 30$ to 40 m s^{-1} . A typical horizontal scale achieved by this initial outburst is $L \sim 20,000 \text{ km}$, which was theorized to

be a maximum attainable value without the storm being influenced by the surrounding zonal winds.

Within two weeks of its development, a GWS will have expanded zonally as its bright clouds move away from its outburst region and was categorized as a “planetary disturbance” in Sánchez-Lavega (1994). This research noted in the 1990 storm that this expansion occurred in both a westerly direction along its northern side and towards the east on the southern edge. These two counterdirectional fronts wrapped around the planet in about twenty days, as it occulted the Northern Equatorial Belt (NEB). The southerly expansion crossed the equator, stopping just short of the region occulted by the rings.

After the storm’s upper-level expansion encircles the planet, Sánchez-Lavega (1994) defined it as the GWS had reached its “mature phase”. Once the 1990 GWS reached this stage, the images showed alternating light and dark spots, spaced out as a quasiregular structure, every ~10,000 to 15,000 km. Additionally, HST images presented a wavy structure to the east of the outburst region, constituted of smaller-scale bright spots every ~5,000 km, representing a morphology of complex turbulence, which were posited to be

localized convective outbreaks. The mature phase was believed to persist over a period of two to three months.

Finally, Sánchez-Lavega (1994) offered the final two stages of the GWS life cycle as “evolution” and “decay”. Once the mature phase was completed, the associated clouds away from the outburst region gradually faded, so that the NEB darkened and became more uniform, though it was broader than it had been prior to the storm. However, some smaller-scale phenomena remained visible with a few storms intensifying, likely showing that convection remained active in some areas.

In the longer-term, there were remnant traces of the 1990 GWS with some swirling light areas, along with tiny spots in the equatorial zone. By 1993, the equatorial zone was still broader than previously observed and continued to contain small areas with enhanced brightness. Additionally, the NEB was reduced to a narrow band located $\sim 21.5^\circ\text{N}$; similar impacts to the belt structure was reports with the 1903 and 1933 events. Given this observational record, a characteristic time for these two phases was proposed to be two to five years by Sánchez-Lavega (1994).

On December 5, 2010, Australian amateur astronomer Anthony Wesley and Japanese amateur astronomer Toshihiro Ikemura recorded the first images of the most recent GWS (Fischer et al., 2011; Sánchez-Lavega et al., 2012). At its initiation, the outburst was ~1,300 km along its north-south axis and ~2,500 km from east to west. Previous GWS development pointed to a periodicity of ~30 years, approximately the length of a Kronian year; however, the 2010 GWS was “ten years early”. With the fortuitous timing of the Cassini mission being in orbit, this offered planetary scientists the opportunity to study up close a meteorological phenomenon that had previously only been observed from Earth.

By July 2011, two letters providing different information about the 2010 GWS, which persisted through the first half of 2011, Sánchez-Lavega et al. (2011) and Fischer et al. (2011), were published in that month’s issue of *Nature*. While Sánchez-Lavega et al. (2011) examined the deep tropospheric winds associated with this storm and an analysis of its deep convective structure, while Fischer et al. (2011) focused on lightning and its development cycle.

Both Fischer et al. (2011) and Sánchez-Lavega et al. (2011) presented timelines of the storm’s onset – on the same day as Wesley and Ikemura’s observations from Earth – the

RPWS instrument aboard Cassini detected radio emissions, which were associated a developing lightning storm. This observation was later confirmed by the ISS as it observed a bright cloud at 32°N , 245°W planetocentric ($37.7^{\circ}\text{N} \pm 0.8^{\circ}$ planetographic). For the first several days, the core of the GWS remained $\sim 32^{\circ}\text{N}$, an area where the mean wind speeds were estimated to be close to zero, and showed no drift, as it maintained a nearly constant longitude. However, after December 8, the center of the storm had moved to $\sim 34^{\circ}\text{N}$ planetocentric ($41.1^{\circ}\text{N} \pm 1.1^{\circ}$ planetographic); it is estimated that there is westerly jet with a velocity of $\sim 22 \text{ m s}^{-1}$ in this location, which corresponds to a westerly drift of $\sim 2.3^{\circ}$ per Earth day. By the latter part of December and into early January 2011, Earth-based images showed a drift of $2.4^{\circ} \pm 0.1^{\circ}$ per day, while the Cassini images showed an even higher rate of drift, $2.8^{\circ} \pm 0.1^{\circ}$ per day ($\sim 28.7 \pm 0.2 \text{ m s}^{-1}$) (Fischer et al., 2011; Sánchez-Lavega et al., 2012). A mean westward zonal velocity of 27.9 m s^{-1} was calculated with maximum speed fluctuations ranging from -5.3 to 2.7 m s^{-1} (Sánchez-Lavega et al., 2012).

While the head of the storm moved to the west along the jet flow, the relative flow at lower latitudes was eastward, which was accounted for the easterly extension of the storm's tail, as it extended equatorward. By late December, it extended across 90° of longitude; by February, the tail had wrapped itself around Saturn and extending across the southern portion of the head. It was noted that the shape of the head and its drift rate

did not change, even after its encounter with the tail (Fletcher et al., 2011; Sánchez-Lavega et al., 2011). This behavior was consistent with the drag of the tail clouds by the ambient zonal winds, which was also consistent with observations of the 1990 GWS. It was also observed that the tail moved along zonal axis, from west to east, with speeds approximating the ambient winds. From this, it was noted that winds at the upper cloud level were not impacted by the onset of the GWS and also essentially remained constant through the duration of this event (Sánchez-Lavega et al., 2011).

Research was also presented in Sánchez-Lavega et al. (2011) that examined this system's three-dimensional structure through imagery using a wide range of filters, ranging from the ultraviolet (375 nm) to the near-infrared (954 nm), along with a standard three-layer Kronian radiative transfer model. The combination of these methodologies led to their finding that the cloud tops of the GWS were at ~150 mbar, approximately 3 km below the top of the tropospheric haze and ~20 km below the tropopause.

The frequent electrical activity that was detected by the Radio Plasma Wave Science (RPWS) instrument, coupled with the rapid growth and brightness of the core, are consistent with previous theories that these storms are moist convective storms, which are fueled by the condensation of ammonia and water, at the 1,000- to 2,000-mbar and

10,000- to 12,000-mbar levels, respectively. At the storm's top, areal growth was driven by the mass transported by the ascending motion of the updraft. Calculations presented in Sánchez-Lavega et al. (2011), which were based on areal expansion rate at the cloud tops, estimated the vertical velocity at the storm top to be 2.5 m s^{-1} , where the storm's total height was estimated to be 260 km, which is the estimated distance from the water level, ~10,000 mbar, to the tropopause. This analysis also took a different approach and calculated a maximum updraft velocity, which was based upon an estimation of the convective available potential energy (CAPE) within the system. This first-order approximation yielded a value of $\sim 150 \text{ m s}^{-1}$, which may occasionally be experienced through its columnar extent.

With regards to the storm's vertical structure, Sánchez-Lavega et al. (2011) noted that the GWSs had previously been observed once per Kronian year during the NH summer. However, this 2010 GWS developed in the early Kronian spring and also developed in the same westerly jet as the 1903 GWS. It was theorized that solar insolation may act as the triggering mechanism. However, contrary to this theory, seasonal temperature changes only occur at levels above ~500 mbar, which has been demonstrated by the modeling of Saturn's atmosphere, along with thermal infrared measurements. Below this level, the zonal wind profile through the 500- to 1,000-mbar level does not change over

one Kronian year, which eliminated a seasonal dynamical instability. It was proposed that the seasonal changes in the upper levels of the troposphere's temperature gradient may impact either the deep vertical motions or indirectly modify meridional cell circulation, which has been proposed to exist between opposing jets within the weather layer.

While Sánchez-Lavega et al. (2011) examined the onset and initial development of the 2010 GWS, Sánchez-Lavega et al. (2012) review the evolution of the storm from February through September 2011, including the dissipation of the storm's head, changes in local wind patterns, and finally the ultimate demise of the GWS. Additionally, comparisons to previous GWSs were made and related to the large-scale impacts on the Saturn's atmosphere.

Sánchez-Lavega et al. (2012) noted that the head of the storm lasted about 195 days with the head of the storm dissipating between June 15 and 19, 2011. During this five-day time frame, the GWS head encountered the Dark Spot (DS) causing for both systems to disappear at optical wavelengths. (The DS was an anticyclonic vortex, i.e., a ridge, that developed on December 21, 2010, in the wake of the GWS head, about 7° longitude to its east.)

The zonal wind analysis presented in Sánchez-Lavega et al. (2012) showed that the GWS head had its onset in the peak of a westerly jet whose velocity was greater than the peak speeds measured in either the Voyager era ($14 \pm 7 \text{ m s}^{-1}$) or the early portion of the Cassini mission ($18 \pm 3 \text{ m s}^{-1}$). In line with earlier research (Hueso & Sánchez-Lavega, 2004; Sánchez-Lavega et al., 2011), it was presumed that the base of the GWS resided within the water clouds, $\sim 10,000$ -mbar level. This analysis associated the higher westerly velocity of the storm's head as a result of stronger jet flow within the deep troposphere.

The cloud features noted in the tail of the GWS were advected at velocities in line with the undisturbed ambient winds, though some differences were observed, particularly along its northern edge. Specifically, in the northern branch, ranging from $\sim 43^\circ$ to 45°N , where there is anticyclonic shear, differences between mean zonal velocities and those measured after the GWS onset ranged from $\Delta u = -30$ to -60 m s^{-1} . In the central branch, which was collocated with the peak of a westerly jet, the difference between the measured and the mean velocity was $\Delta u = \pm 20 \text{ m s}^{-1}$. Along the southern branch, which is in a cyclonic flow regime, the velocity of most of the cloud features within $\pm 10 \text{ m s}^{-1}$ of the mean flow (Sánchez-Lavega et al., 2012). This research posited that the differences between the undisturbed winds and the velocity at which the cloud features in the tail

were advected may have been due to either turbulent motion or through wave propagation, relative to the mean flow.

The GWS development cycle led to the onset of an anticyclonic vortex (AV), which has also been referred to as the “Dark Spot” (DS). The AV formed between December 5 and 24, 2010; by December 24, it had a roughly circular core that was bright in the MT3 band. The blue coloration of the AV is indicative that the clouds are at a higher altitude than the surrounding clouds, which appear white. Sánchez-Lavega et al. (2012) estimated that the top of the GWS’ head reached to ~150 mbar. Therefore, this analysis of the AV would imply that it extended to a higher altitude.

The core was estimated to have a diameter of 4,250 km in late December, centered at 33°N. By January 11, the AV measured 11,000 km in the meridional direction and 12,000 km in the zonal direction. The examination of the wind flow within the AV showed that it indeed had anticyclonic flow with winds in excess of 120 m s^{-1} in its outer annular region. Sayanagi et al. (2013) reviewed the wind shear structure around this feature with the cyclonic shear on the equatorward side of the AV being strong than the poleward side’s anticyclonic shear.

While the demise of the 2010 GWS was documented in Sánchez-Lavega et al. (2012), Sayanagi et al. (2013) extended this research to examine the aftereffects of the AV (referred to as the “DS” in Sánchez-Lavega et al. (2012)) collision with the head. After this interaction, the ISS was not directed to examine this region until July 12, 2011. From these images, it was noted that the head was no longer visible; however, it is believed that AV remained intact. It was noted that due to the gap in observations that this assertion cannot be verified, but the post-collision location of the AV was consistent with to where the pre-collision vortex would have transited. Therefore, the conclusion was made these were the same phenomena.

Sayanagi et al. (2013) compared NH zonal wind profiles consisting of data collected during the Voyager missions (1980 and 1981), along with ISS CB2 filter observations, i.e., 300- to 500-mbar level, from May 2008 through August 2011. The analysis showed that away from the location of the 2010 GWS that the zonal wind profiles were generally the same over the four-year period. It was also noted that the propagation speed of the storm’s head, $u = -26.9 \text{ m s}^{-1}$, was significantly larger than the mean zonal wind speed, $u \approx -6 \pm 1.7 \text{ m s}^{-1}$, during the at latitude 32.6°N in January 2011. By August 2011, after the GWS’ dissipation, the zonal wind speed had increased to $-22 \pm 4.2 \text{ m s}^{-1}$.

As referenced earlier in review of Sayanagi et al. (2013), analysis of the August 2011 zonal winds showed changes in their speeds when comparing before and after the GWS, which lead to variations to the localized wind shear. Comparing the August 2011 zonal wind speed to those of May 2008 and using 34°N as a delimiter, south of this axis, the zonal winds exhibited a deceleration of $\sim 30 \text{ m s}^{-1}$, while poleward of it, there was an acceleration of $\sim 35 \text{ m s}^{-1}$. The magnitude of these changes is greater than the associated uncertainty, indicating they are significant.

Additionally, results presented in Achterberg et al. (2012) indicated that these changes in zonal winds were supported by tropospheric warming, which is consistent with an associated latent heat release. While Sayanagi et al. (2013) acknowledges the cloud motion could be explained by variations in cloud altitude and VWS, the results presented are in line with the conclusions from Achterberg et al. (2012) that tropospheric warming yielded the wind speed changes.

Sayanagi et al. (2013) proposed two potential sources of the changes to zonal wind speeds. In one case, the GWS may have generated the anticyclonic vorticity – a main difference between the pre- and post-GWS zonal wind patterns is the addition of anticyclonic shear around the storm. The notable and rapid growth pattern of the head

demonstrates there were horizontal divergence, which directly leads to anticyclonic vorticity on a rotating planet. Additionally, because of the convective nature of the GWS, a significant amount of latent heat would have been released into the deep troposphere. Therefore, the storm would have impacted the latitudinal temperature gradient, dT/dy , around the storm's center, increasing it equatorward, while it decreased in the poleward direction. Based on the standard form of the TWE, these changes would also yield changes in the vertical wind shear. With the assumption that the zonal wind speeds at the cloud condensation layer are steady through the storm's lifecycle, their velocity at the cloud tops would increase to the north, while it decreased to the south. This conclusion is consistent with the observed wind speed changes, along with the tropospheric warming that was documented in Achterberg et al. (2012).

With the development of the 2010 GWS in the middle latitudes, this was consistent with an established pattern of alternating storm development between the equatorial and mid-latitude regions. Some comparisons can be made to the 1903 GWS, which also struck the mid-latitudes, $\sim 30 \pm 2^\circ\text{N}$. The 1903 and 2010 GWS also had the longest lifespans, ~ 150 and ~ 200 days, respectively. Their longevity may represent a lack of the vertical wind shear at these latitudes through the columnar growth of these storms, and therefore, this region of the troposphere.

Given the infrequent nature of the GWS development, a mechanism is believed to exist which would allow for a buildup of CAPE between onsets. Within the deep troposphere, ~10,000 mbar, it is theorized that there is a layer of water clouds. Due to the condensation within this layer, the latent heat release is believed to enhance the static stability by essentially capping the region. This effect would inhibit any convective development and allow for the region underneath to “store” CAPE (Sayanagi et al., 2013).

GWS development may result from a confluence of events, once the CAPE is sufficient to develop into the convective cumulus storm. Such instability may occur due to seasonal effects with an increase in insolation. Additionally, Rossby wave development and intensification in the water condensation layer may have led to the SoPs formation. Such Rossby development has been shown to impact cloud-top levels at the 10,000-mbar level (Sayanagi & Showman, 2007). The linkage between the SoPs and Rossby waves through the troposphere was discussed in Sayanagi et al. (2013) and initial investigation of VIMS and ISS images show some connection, though it remains a subject for further investigation.

This dissertation research focused on February 26, 2011 where the GWS was in a mature phase and had fully encircled Saturn. A goal of this research was to work with this

highest resolution images available, which included the CB2 and MT2 filters with a maximum resolution of 14 km pixel^{-1} , while additional images from the BL1 (blue, 463 nm) and MT3 filters provide a resolution of 28 km pixel^{-1} (García-Melendo et al., 2013).

Due to the shorter time scale of observations and subsequent measurements, localized wind speeds were higher than noted in previous research. The well-developed AV dominates the pattern at this time and drives mean flow along the frontal boundary with the velocities of $120 \pm 30 \text{ m s}^{-1}$. Figure 6.2 shows that along the northern boundary, $\sim 37.5^\circ\text{N}$, the jet flow combined with the GWS outflow yielded peak velocities of $160 \pm 30 \text{ m s}^{-1}$, while on the equatorward side, wind speeds with $-110 \pm 30 \text{ m s}^{-1}$ (García-Melendo et al., 2013).

A representation of the instantaneous wind field after it had been spatially averaged through the interpolation of the wind vectors into a regular grid is shown in Figure 6.2. By implementing this, it smooths the measurement noise, along with the turbulence; this data was applied in the calculation of the mean vorticity of the GWS, $-9 \pm 3 \times 10^{-5} \text{ s}^{-1}$, which is about six times larger than the ambient meridional wind shear, $\partial u / \partial y \approx 1.5 \pm \times 10^{-5} \text{ s}^{-1}$ and half the planetary vorticity, $f = 2\Omega \sin\phi \approx 2 \pm \times 10^{-4} \text{ s}^{-1}$. The derivation of these terms

was applied to the approximation of the pressure gradient between the arc-front and the center of the GWS head, $\partial P/\partial r \approx -40$ mbar/1,000 km. This pressure gradient is two to three times the level observed through Terran mid-latitude baroclinic anticyclones and twice as large as noted in the Jovian Great Red Spot (García-Melendo et al., 2013).

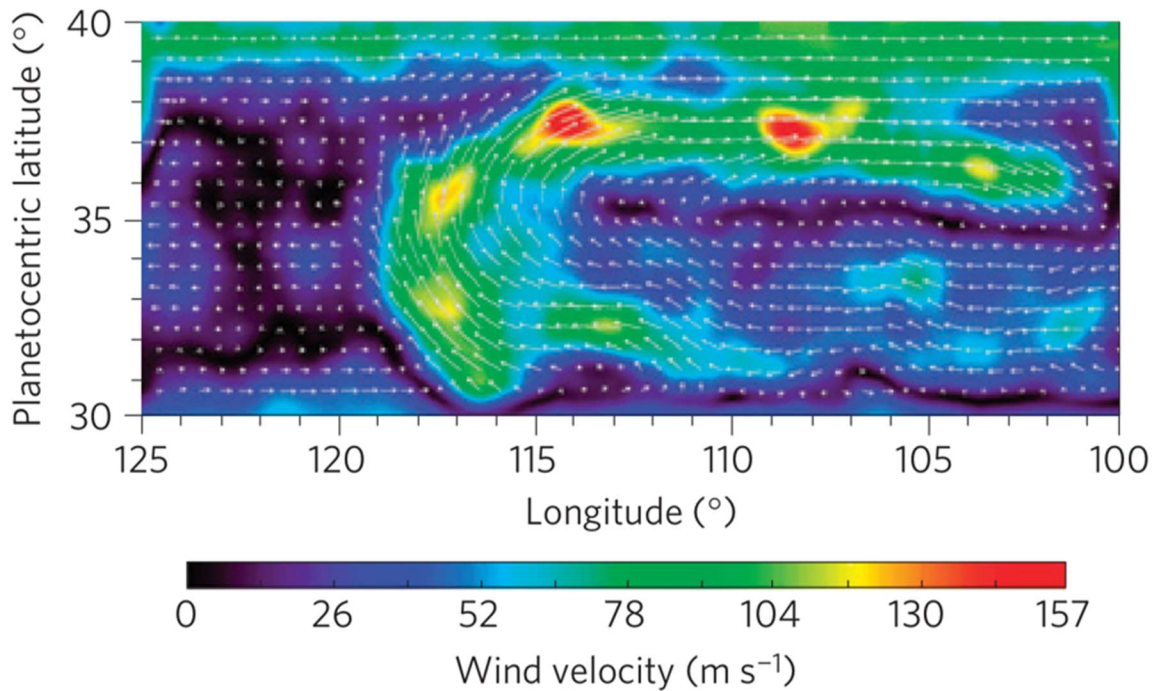


Figure 6.2. Mean wind velocity at the head of the 2010 GWS. Data has been spatial averaged through an interpolation of the wind vectors (García-Melendo et al., 2013).

When comparing moist convection on Earth to that of the gas giants, there are three principle differences.

- 1) The density of dry air is less than moist air on the gas giants. Specifically, on Saturn, the molecular weight of dry hydrogen-helium atmosphere is 2.2 g mol^{-1} ,

while the condensates, i.e., ammonia and water, have molecular weights of 17 and 18 g mol⁻¹, respectively;

- 2) Convection on a gas giant is primarily controlled by cooler in the upper atmosphere, i.e., the stratosphere, tropopause, and upper troposphere, rather than being heated in the deep troposphere, ~10,000-mbar level; and
- 3) The radiative timescale is on the order of decades.

Specific to Item 1 above, the molecular weight of the relatively dense condensates, particularly, water and ammonia, was shown through both calculations and modeling associated with Li and Ingersoll (2015) to inhibit the upward motion of the moist parcels, thereby reducing the intensity of the convection. However, the semi-regular occurrence of the Kronian GWS shows that some mechanism is strong enough to overcome this imposing atmospheric structure.

Li and Ingersoll (2015) used a three-step approach to study the GWS trigger and subsequent onset, the post-dissipation phase of the GWS region re-achieving geostrophic balance, and finally, the slow cooling of the atmosphere as it related to understand why a decades-long gap between storm occurrences. This review will focus on the first and third portions of their research.

This first step of this research examined the convective inhibition phase and how it is achieved in the deep tropospheric layer. As noted previously, a moist parcel has a higher molecular weight than a dry parcel. Li and Ingersoll (2015) demonstrated if a parcel (layer) has a water mixing ratio that is supercritical, is experiencing radiative cooling, and in a specific temperature range, its virtual temperature is greater than the layer beneath it. (This is because the radiative cooling is experienced from the top down.) In this case, the density is lower for cooler layer, which means it is floating atop of the deep dense atmosphere, imposing stable stratification at the cloud base. This structure not only suppresses convection, but it also decouples the interior from the troposphere, so that the interior temperature remains fixed. The inhibition of the convection yields an increase in CAPE as it accumulates.

For convection to be initiated, a series of atmospheric conditions must fall into place. If the cooling at the top of the atmosphere is great than the radiative heat transfer, the stable layer will persist as the tropospheric cools. With this cooling pattern, the density just above the cloud base will decrease through precipitation processes, which will yield a stable interface with the fluid just below the cloud base. However, this cooling rate is relatively slow because the radiating temperature, while the specific heat of the atmospheric column is high. The stable stratification will dissipate once the virtual

temperature above and below the cloud base is equal. Once the convective inhibition reaches zero, the warm moist parcel rises from the deep troposphere, releasing the stored CAPE. The buoyancy difference through the column will accelerate the parcel upward, freeing latent heat as it condenses. With the emission of the latent heat, the surrounding atmosphere warms through subsidence, allowing the cycle to repeat. A tenuous balance between radiative cooling and convective heating causes the system to oscillate between these two states (Li & Ingersoll, 2015).

In order to establish this cyclical behavior, the water vapor mixing ratio had to be in excess of 1.0%, which is ten times the solar value, where the solar O/H ratio is 4.90×10^{-4} (Li & Ingersoll, 2015). This enrichment factor is consistent with those found for carbon and phosphorus on Saturn. In this case, this would demonstrate that water levels would be high enough to support the deep and vigorous convection. Comparatively, the Galileo probe has demonstrated that the enrichment factors of the heavier elements, carbon, nitrogen, and phosphorus, in Jupiter range to two to five. If water on Jupiter has a similar enrichment factor, then this would be insufficient to support the water-loading mechanism and subsequent deep convection. This may indicate why storms with as energetic a structure as the Saturn's GWSs have not been observed on Jupiter.

6.2 Asymmetric Expansion in 2010 Great White Storm

As noted earlier in this Chapter, a notable development in the lifecycle of the 2010 GWS was that the storm-related bright clouds expanded to the south, but their growth to the north was limited. This resulted in a pattern where as the “anvil” clouds encircled Saturn, the northern edge of the tail passed over the southern extent of the head (García-Melendo et al., 2010; Sánchez-Lavega et al., 2012; Sayanagi et al., 2013).

Figure 6.3 shows a Hovmöller diagram shows a time series of the images of the 2010 GWS, captured by the CB2 filter on the ISS. Panel A of Figure 6.3 shows a strong divergence within the head region from December 23 and 24, 2010, which generated bright clouds extending from $\sim 27^{\circ}\text{N}$ to $\sim 40^{\circ}\text{N}$ around the onset site, $\sim 34^{\circ}\text{N}$. The zonal winds advected the bright clouds to the east, as well as them spreading longitudinally, causing them to extend across a portion of the mid-latitudes and yielding a bright cloud zone (BCZ).

In the early part of 2011, the meridional spread continued across the tail of the storm, though in an uneven fashion. From December 2010 to January 2011, the northern edge of the BCZ slowly moved from $\sim 40^{\circ}\text{N}$ to $\sim 42^{\circ}\text{N}$ and then kept stable over time. Contemporaneously, the southern boundary of the BCZ rapidly moving to $\sim 27^{\circ}\text{N}$ in

December 2010 to $\sim 20^{\circ}\text{N}$ by February 2011, thereafter it maintained this extent through the remainder of the GWS' lifecycle. This lopsided expansion of the BCZ is potentially due to an existing north-south-oriented asymmetry in the cloud mixing (Dowling, 2014; McIntyre, 2014; Polvani et al., 1995), which will be addressed in this Chapter.

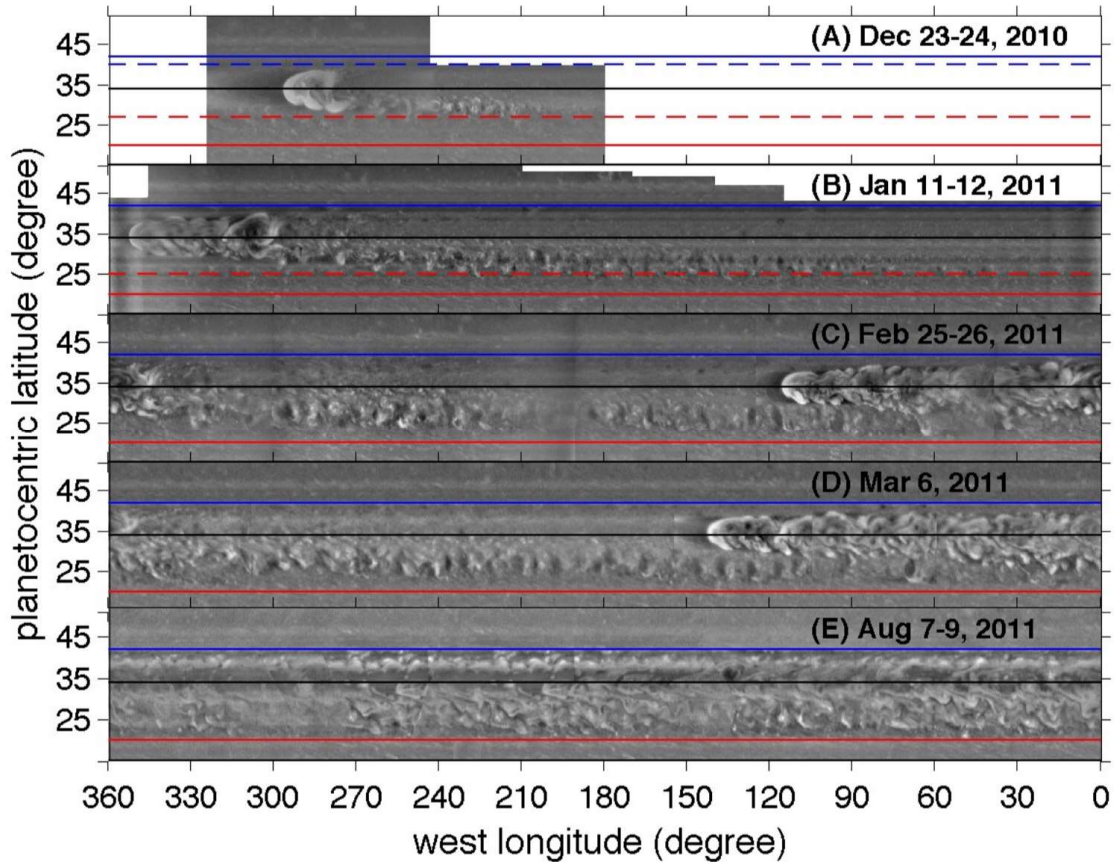


Figure 6.3. Hovmöller diagram of the 2010 Great White Storm from December 2010 through August 2011. The raw ISS images were captured by the WAC in the CB2 (752 nm) with the spatial resolution changing from $\sim 50 \text{ km pixel}^{-1}$ to $150 \text{ km pixel}^{-1}$. The blank areas in Panels A and B are observational gaps. The horizontal blue and blue solid lines are the final northern and southern boundaries of the BCZ at 42°N and 20°N , respectively. The dark horizontal lines represent the center latitude, $\sim 34^{\circ}\text{N}$, of the storm's head.

6.2.1 Methodology – Asymmetric Expansion in 2010 GWS

The horizontal mixing of clouds is impacted by the meridional gradient of the zonal-mean quasi-geostrophic potential vorticity, \bar{Q}_y (e.g., Andrews et al., 1987; Holton, 2004; Pedlosky, 1987; and Salby, 1996). In certain cases, large magnitudes of \bar{Q}_y can act as a transport barrier, which will inhibit such mixing (Dowling 2004; McIntyre, 2014; and Polvani et al., 1995).

The parameter \bar{Q}_y , defined in (26) (e.g., Andrews et al., 1987; Salby, 1996) has been measured and studied in Cassini-era studies of Saturn (e.g., Read, Conrath, et al., 2009; Read, Dowling, et al., 2009).

$$\bar{Q}_y = \beta - \bar{u}_{yy} - \frac{1}{\bar{\rho}} \frac{\partial}{\partial z} \left(\frac{f_o^2 \bar{\rho}}{N^2} \frac{\partial \bar{u}}{\partial z} \right) \quad (26)$$

The term \bar{Q}_y consists of three terms, the first being β , the meridional gradient of the planetary vorticity, $\beta = df/dy$. The planetary vorticity f is defined as $f = 2\Omega \sin\phi$, where Ω is the planet's rotational rate and ϕ is latitude. Therefore, the first term can be expressed as (27)

$$\beta = \frac{df}{dy} = \frac{d(2\Omega \sin\phi)}{r_c d\phi} = \left(\frac{2\Omega}{r_c} \right) \cos\phi, \quad (27)$$

where r_c is the planet's effective radius. A planet's effective radius, which varies with latitude on Saturn, due to its oblateness, can be calculated through (28)

$$r_c = r_{eq}r_{po}/\left[\left(r_{eq}\sin\phi\right)^2 + \left(r_{po}\cos\phi\right)^2\right]^{\frac{1}{2}}, \quad (28)$$

where r_{eq} and r_{po} are the equatorial and polar radii, respectively.

The second term of \bar{Q}_y is $-\bar{u}_{yy}$, the meridional gradient of the relative vorticity, $-\bar{u}_y$. For a planetary atmosphere where the zonal wind, \bar{u} is dominant, such as Saturn's, the relative vorticity can be estimated by the meridional derivative of the zonal winds, $-\bar{u}_y = -\partial\bar{u}/\partial y$.

The third and final term is \bar{Q}_y (29) is referred to as the "stretching term" and is mainly determined by the vertical shear of the zonal winds, $\partial\bar{u}/dz$,

$$-\frac{1}{\bar{\rho}}\frac{\partial}{\partial z}\left(\frac{f_0^2\bar{\rho}}{N^2}\frac{\partial\bar{u}}{\partial z}\right). \quad (29)$$

For this term, a log-pressure coordinate (e.g., Andrews et al., 1987; Holton, 2004; and Salby, 1996) so that the atmosphere depth, z , is defined $-H\ln(p/p_s)$, where H is the scale height, p is the pressure, and p_s is the surface pressure, which will also be used the reference pressure. Since there is no visible surface on Saturn, p_s is defined to be the 1,000-mbar level. The additional terms in (29) are: $\bar{\rho}$, the mean atmospheric density, N , the buoyancy frequency, and the planetary vorticity at the reference latitude, f_0 . Specific to

the 2010 GWS, the reference latitude was established based on the center of the storm's onset, which was 34°N.

The mean atmospheric density, $\bar{\rho}$, at each pressure level is calculated through the Ideal Gas Law, $\bar{\rho} = p/R_s\bar{T}$, where \bar{T} is the mean temperature at each pressure level. Based on Cassini observations, the composition of Saturn's atmosphere which approximated to be ~93% H₂ and ~7% He, yielding a molecular weight of 2.14×10^{-3} kg/mol. The specific gas constant R_s for Saturn is calculated to be $R^*/MW = 8.314/0.00214 = 3885 \text{ J kg}^{-1} \text{ K}^{-1}$ (Achterberg et al., 2016). The scale height $H = R\bar{T}/g$, where g is the gravity of Saturn; however, due to its oblateness, Saturn's gravity varies with latitude (Helled & Guillot, 2013).

Continuing through the "stretching term", the buoyancy frequency, N , also has a temperature dependency, $N^2 = g (d \ln \Theta/dz^*)$, where Θ is the potential temperature and z^* is the height. The term potential temperature, Θ , which is the temperature that an atmospheric parcel would attain if it were moved adiabatically to a reference pressure level and is defined as $\Theta = T(p_s/p)^{R/C_p}$, where C_p is the heat capacity of Saturn's atmosphere, $\sim 13,125 \text{ J kg}^{-1} \text{ K}^{-1}$ (Achterberg et al., 2016). Based on the following, $p_s = 1,000$ mbar, $R = 3,885 \text{ J kg}^{-1} \text{ K}^{-1}$, and $C_p = 13,125 \text{ J kg}^{-1} \text{ K}^{-1}$, the potential temperature, Θ , and

subsequently, the buoyancy frequency N from the temperature T at each pressure level, p (Figure 6.4).

For the “stretching term”, there were not good measurements of the vertical shear of the zonal winds, $\partial\bar{u}/dz$, through the use of Cassini ISS imagery. However, radiance data was captured by the CIRS around the ~150-mbar level, which was the estimated height of the bright clouds in the 2010 GWS. Atmospheric temperature fields were then constructed, based on the radiance data, which were then applied to standard form of the thermal wind equation. The application of the standard TWE to the meridional temperature gradient yielded the vertical shear of the zonal winds.

As reviewed in Chapter 3 of this dissertation, the thermal wind equation can be expressed as Equation (30), using log-pressure coordinates

$$\frac{\partial\bar{u}}{\partial \ln p} = \left(\frac{R}{f}\right) \left(\frac{\partial T}{\partial y}\right), \quad (30)$$

where R is the gas constant and T is local temperature. Based on the standard TWE, the vertical wind shear can be expressed as Equation (31)

$$\frac{\partial\bar{u}}{\partial z} = \left(-\frac{1}{H}\right) \left(\frac{\partial\bar{u}}{\partial \ln p}\right) = \left(-\frac{R}{Hf}\right) \left(\frac{\partial\bar{T}}{\partial y}\right). \quad (31)$$

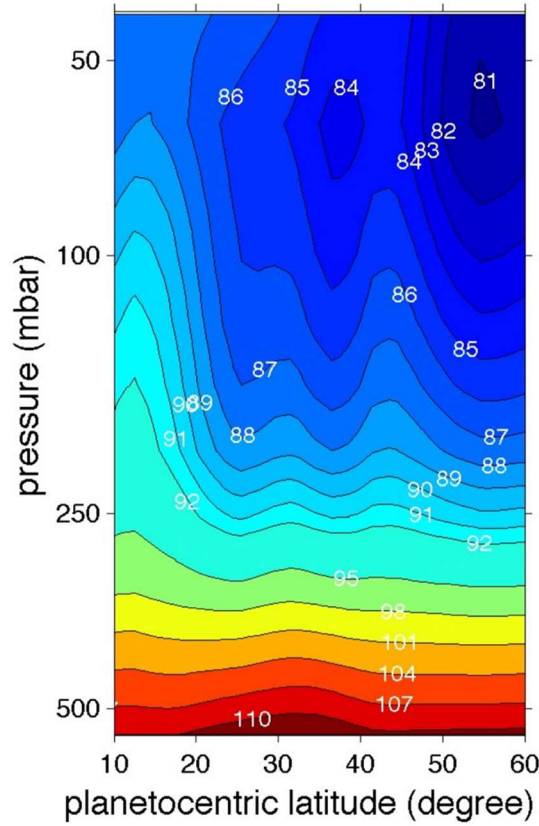


Figure 6.4. Cassini measurements of the Northern Hemisphere temperature field of Saturn in 2011. The original atmospheric temperature data comes from a previous study (Achterberg et al., 2014), which was retrieved from CIRS observations in 2011. The derived temperature data has a spatial resolution of $\sim 1^\circ$ latitude and $\sim 0.1 \times$ scale height, H , in the vertical direction. The numbers along the contour lines are temperature in Kelvin.

Converting from $\partial u / \partial z$ to $\partial T / \partial y$, the stretching term can be rewritten as Equation (32)

$$-\frac{1}{\rho} \frac{\partial}{\partial z} \left(\frac{f_0^2 \bar{\rho}}{N^2} \frac{\partial \bar{u}}{\partial z} \right) = \frac{f_0^2 R}{f \bar{\rho}} \frac{\partial}{\partial z} \left(\frac{\bar{\rho}}{N^2 H} \frac{\partial \bar{T}}{\partial y} \right). \quad (32)$$

Equation (32) is used to compute the stretching term, allowing for the determination of the meridional gradient of the zonal-mean quasi-geostrophic potential vorticity, \bar{Q}_y . The

parameter will be a key factor in the investigation of the asymmetric expansion of the bright clouds in the 2010 GWS.

6.2.2 Results – Asymmetric Expansion in 2010 GWS

During its thirteen-year mission, the Cassini spacecraft observed all phases of the 2010 GWS. Of particular note, the onset and subsequent expansion of this event’s bright clouds was observed by the ISS and CIRS. Measurements from these two platforms were used to estimate the meridional gradient of the zonal-mean quasi-geostrophic potential vorticity, \bar{Q}_y .

$$\bar{Q}_y = \beta - \bar{u}_{yy} - \frac{1}{\bar{\rho}} \frac{\partial}{\partial z} \left(\frac{f_o^2 \bar{\rho}}{N^2} \frac{\partial \bar{u}}{\partial z} \right) \quad (33)$$

The first term, β , the meridional gradient of planetary vorticity can be estimated with the rotation period provided in Studwell et al. (2018), i.e., 10h 33m 24s, the equivalent rotation rate is $\Omega = 1.653 \times 10^{-4} \text{ s}^{-1}$. With regards to the second term, in order to estimate the meridional gradient of the relative vorticity, $-\bar{u}_{yy}$, the zonal winds at the pressure level of the bright clouds were needed. Based on analysis presented in both Sánchez-Lavega et al. (2011) and García-Melendo et al. (2013), the base of the bright clouds was at the ~400-mbar level. Images from the ISS CB2 filter were initially used to observe the storm’s development and expansion, then to measure the local winds (Sayanagi et al., 2013).

Fortuitously, these data were captured at both the appropriate time and pressure levels to yield a characterization of the cloud expansion and capture the needed zonal wind speeds. Figure 6.5 shows the zonal wind profile across the Northern Hemisphere, based on data from January and August 2011 (Sayanagi et al., 2013); this data includes both the spatial range and temporal period of the 2010 GWS. Based on this profile, a central difference scheme was used to calculate the meridional gradient of the relative vorticity, $-\bar{u}_{yy}$, shown in Figure 6.6.

In order to calculate the third term, the “stretching term” of \bar{Q}_y , CIRS radiance data is used to determine the atmospheric temperature profile through vicinity of the GWS. Figure 6.4 shows the 2011 temperature profile (Achterberg et al., 2014), which is generally contemporaneous with development, mature phase, and dissipation of the 2010 GWS. This graphic shows the temperatures through the upper troposphere (~50 to 500 mbar), which includes the pressure levels of the bright clouds, ranging from 150 to 400 mbar (Sánchez-Lavega et al., 2011).

Three atmosphere layers, 373, 403, and 435 mbar, around the bright clouds were selected from Figure 6.4 to estimate the stretching term in (26). From this data, the meridional temperature gradient, $\partial T/\partial y$, along with the potential temperature and buoyancy

frequency, can be calculated from this data set. Based on these derived atmospheric parameters, the stretching term, and subsequently, \bar{Q}_y , can be estimated.

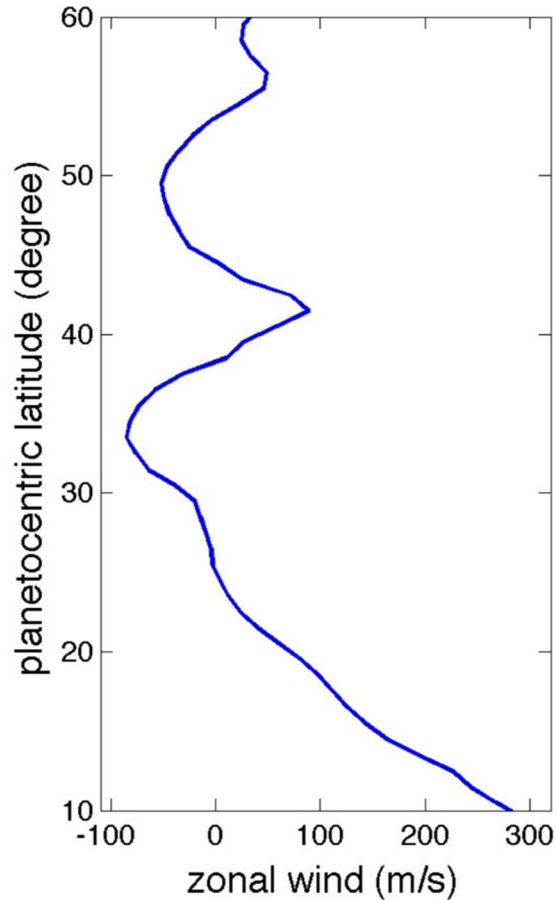


Figure 6.5. Cassini measurements of the Northern Hemisphere zonal wind field of Saturn in 2011. The zonal winds were obtained from a previous study (Sayanagi et al., 2013) and were based up on Cassini ISS observations from January and August 2011. The original data of zonal winds have a spatial resolution of $\sim 0.1^\circ$ in latitude. The data were averaged with a latitude bin of 1° , in order to filter variations at very small spatial scales. The original zonal wind data was calculated with the rotation rate based upon Voyager observations of $\Omega = 1.638 \times 10^{-4} \text{ s}^{-1}$. However, to be consistent with the analysis, this zonal wind profile was derived using the Cassini-era rotation rate of $\Omega = 1.651 \times 10^{-4} \text{ s}^{-1}$.

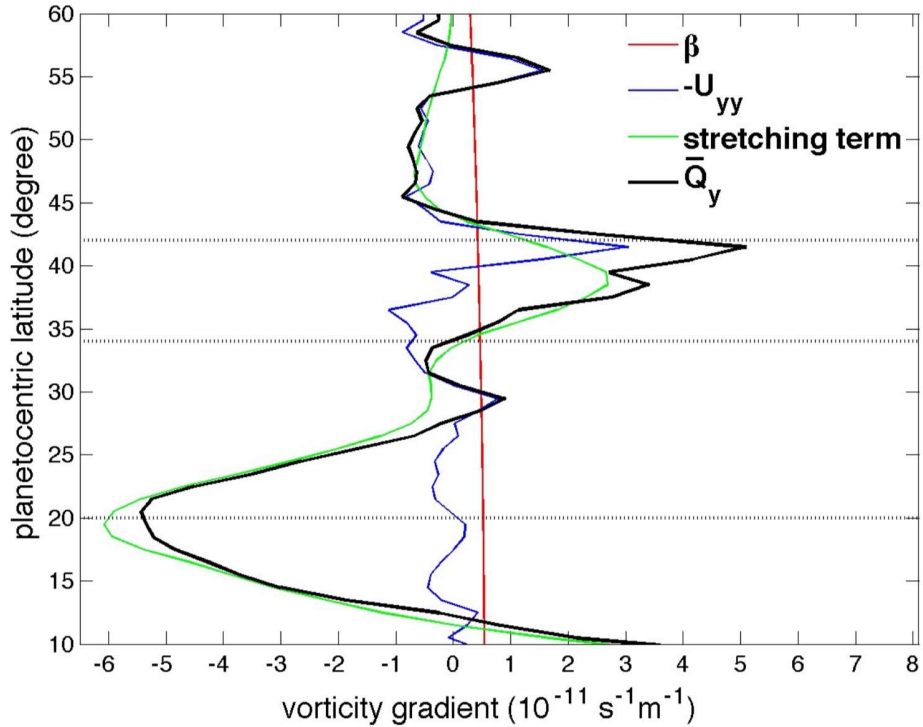


Figure 6.6. Zonal-mean meridional gradient of the quasi-geostrophic potential vorticity, \bar{Q}_y . The three components on the QGPV are plotted: meridional gradient of planetary vorticity, β (red); meridional gradient of the relative vorticity, $-\bar{u}_{yy}$ (blue); and the “stretching term” (green).

Figure 6.6 shows that the zonal-mean quasi-geostrophic potential vorticity, \bar{Q}_y , has its two strongest NH peaks near $\sim 20.5^\circ\text{N}$ and $\sim 41.5^\circ\text{N}$. The position of these high \bar{Q}_y values are collocated with the equatorward and poleward boundaries of the 2010 GWS’ bright clouds at $\sim 21^\circ\text{N}$ and $\sim 42^\circ\text{N}$, respectively. Previous research has demonstrated that the large gradients of \bar{Q}_y does not favor cloud mixing (e.g., Beron-Vera et al., 2008; Dowling, 2014; Jukes & McIntyre, 1987; McIntyre, 2014; and Polvant et al., 1995).

Juckes and McIntyre (1987) presented research on the austral stratospheric polar vortex, where ozone-depleted air was trapped inside the vortex. It was argued that the large gradients of \bar{Q}_y were associated with a large Rossby wave restoring force, which inhibits the meridional transport at a larger scale. Additionally, the research presented a case where the meridional zonal wind shear, $\partial u/\partial y$, would restrict transport as a smaller scale.

The meridional gradient of \bar{Q}_y bracketing the northern and southern extents over the bright clouds are likely strong enough to inhibit meridional cloud mixing. This would explain the asymmetric expansion of the bright clouds with the cloud mixing stopped at these two boundaries. Figure 6.6 demonstrates the contribution of individual terms to the total value of \bar{Q}_y . For the NH, the largest value of \bar{Q}_y , which is along the northern boundary of the bright clouds, $\sim 42^\circ\text{N}$, mainly come from the largest meridional gradient of the relative vorticity, $-u_{yy}$. A comparison of Figures 6.5 and 6.6 also visualizes the relationship between strong vorticity gradient and the eastward jet located in that region. In addition, the stretching term provides a large contribution along the northern extent. With regards to the southern boundary of the bright clouds of the 2010 GWS, this strong level of \bar{Q}_y is primarily due to the stretching term, which is aligned with the strong vertical variation of the zonal winds.

6.3 Conclusions

In this Chapter, an overview of previous research on Saturn's Great White Storm was presented, dating back to 1876. During the onset of the 2010 GWS, the scientific community was fortunate to have the Cassini mission on location to observe and provide data, which would be used in the study of this rare event. During the mature phase of this event, the dynamics of this growth and the surrounding atmosphere yielded an asymmetric storm, limiting in its poleward growth.

Through the analysis conducted for this Chapter, the meridional gradient of the zonal-mean quasi-geostrophic potential vorticity, \bar{Q}_y , was calculated, based on the temperature and wind fields observed by Cassini. The resulting data suggests that the strongest gradient of \bar{Q}_y acted a transport barrier, which inhibited the meridional mixing of the bright clouds that were generated and advected downwind of the 2010 GWS. These atmospheric conditions can help explain the lopsided expansion of these upper tropospheric clouds.

The mechanism by which a large meridional gradient of QGPV as a barrier to transport barrier has already been discovered in Earth's stratosphere (Polvani et al., 1995). However, it should be noted that such a mechanism has not been noted within Earth's

troposphere, most likely due to its more complicated atmospheric dynamics, particularly because of the boundary layer. By contrast, Saturn's troposphere has a comparatively simple dynamical environment since it has no solid surface and therefore, no resultant atmosphere-surface interaction.

This quasi-idealized dynamic environment means that particular atmospheric processes, i.e., giant storms, can be explored and examined. This analysis suggests that the QGPV plays an important role in the maturation of storms in the atmospheres of gas giants on both a synoptic and planetary scale.

Chapter 7: Conclusions

This dissertation and its associated research were conducted to provide insight into the spatiotemporal variations with Saturn's atmosphere during the thirteen-year Cassini mission. From the deep troposphere out to the stratosphere, topics such as long-term patterns of the zonal jets on a global scale, atmospheric stability conditions in the vicinity of deep jets, the evolution of the polar jet over time, and the Great White Storms of Saturn, with particular focus on the evolution of the 2010 GWS were examined. Our examinations provide a better insight into jet structure, the large-scale atmospheric circulation, and the seasonal variations of Saturn's atmosphere. In addition, the analyses of the atmospheric winds and vorticity fields aid in our understanding of the 2010 Great White Storm, the largest such event ever observed on Saturn. Through this scientific endeavor, our understanding of planetary atmospheres, particularly with regards to the gas giants of our Solar System has improved.

Chapter 3 reviewed the derivation of the standard form of the thermal wind equation. In addition, a more general form of the equation was presented with an emphasis on the underlying physics, though it is still an approximation with limitations due to the use of the simplified momentum equations. However, the general form did not apply any approximations of geostrophic or hydrostatic balance. The general TWE also offers a

constraint on the connection between the thermal and dynamical fields, along the cylindrical direction.

Both forms of the TWE were applied to NCEP2 reanalysis data with the results examined for verification of their accuracy on a regional basis. This analysis proposed that the general TWE yielded improved results versus the standard TWE in the equatorial region, while for the mid- and polar latitudes showed little difference in the results. These results occurred because the assumption of geostrophic and hydrostatic balance does hold in these regions. These results would allow for the combined use of the general form in the equatorial region, while the standard TWE can be used across the rest of the planet. This combination would increase our capacity for the exploration and understanding of planetary atmosphere within our Solar System and beyond.

Chapter 4 applied the new general form of the thermal wind equation, which was derived in Chapter 3, to data collected during the Cassini mission. Specifically, time-averaged CIRS radiance data, which ranged from the stratosphere to the upper troposphere, along with 500-mbar winds that were collected by the ISS was examined in order to study the upper-level zonal winds.

This analysis showed that the weakening of the low-latitude jets with altitude was observed in the NH, which aligns with previous research conducted on similar atmospheric structures in the SH. In addition, the application of the general form of the TWE to independently-derived temperature data from different time periods showed very strong stratospheric jets, $\sim 800 \text{ m s}^{-1}$, within the equatorial zone. These jets were also estimated to be stronger than previous research had indicated and were, at least in the short-term, stable features.

Chapter 5 yielded the first global profile of the 2,000-mbar zonal winds. The comparison between the deep tropospheric winds observed through the VIMS with the 300- to 500-mbar level winds from the ISS implied a general constancy of atmospheric structure on a global scale. However, there are also notable differences, again on a global scale.

Across the equatorial region, analysis indicated that the zonal winds increase $\sim 50 \text{ m s}^{-1}$ as one moves from the upper troposphere, the 300- to 500-mbar level, down to the deeper troposphere, $\sim 2,000$ -mbar level. On the other hand, the investigation showed a reduction in the zonal wind velocities through the mid- to high latitudes in both hemispheres, as one moves deeper in the atmosphere.

The tropospheric zonal winds are also examined to assess Saturn's atmospheric stability. The analysis indicated that most of the zonal jets located across the 300- to 500-mbar and 2,000-mbar pressure levels were barotropically unstable. Additionally, by means of an examination of the Richardson number, it was proposed that a necessary condition for the baroclinic instability, i.e., significant vertical wind shear, was met in some locations. Finally, the TWE was applied to the zonal winds between the VIMS and ISS observation levels, indicating that the meridional temperature gradient can be in excess of 2K per degree of latitude at the mid- and high latitudes.

Deep tropospheric zonal winds observed within Saturn's polar regions were studied to note their temporal variations. At the 2,000-mbar level, the zonal winds were fairly consistent between 2006 and 2017 across the both the NH and SH. However, poleward of 85°N, the westerly jet as noted to have decreased from 2008 to 2017 by $\sim 44 \pm 14 \text{ m s}^{-1}$.

Chapter 6 offered an analysis and overview of the Great White Storms of Saturn, ranging from a historical perspective of the GWS' observations to their typical life cycle. Specifically, the 2010 GWS was reviewed with particular attention to its asymmetric growth during the mature and dissipation phases, which was limited in the poleward direction.

In order to understand the restrictions of the northerly expansion of the 2010 GWS, the meridional gradient of the zonal-mean quasi-geostrophic potential vorticity, \bar{Q}_y , was evaluated, based on observed temperature and wind fields. Consistent with previous research, this analysis suggested that the strongest gradient of the \bar{Q}_y inhibited the meridional mixing of the bright clouds associated with the mature phase of the 2010 GWS.

The quasi-idealized atmospheric environment allows for dynamic processes, including giant storms, can be explored and examined. The analysis showed that the quasi-geostrophic potential vorticity plays a key role in the maturation of storms on both a synoptic and planetary scale. Moreover, this research reinforces that the atmospheric wind and vorticity fields play critical roles in cloud advection and associated convective development on both synoptic and planetary scales.

BIBLIOGRAPHY

- Achterberg, R. K., & Flasar, F. M. (1996). Planetary-scale thermal waves in Saturn's upper troposphere. *Icarus*, 119(2), 350-369.
- Achterberg, R.K., Gierasch, P.J., Conrath, B.J., Hesman, B.E., Bjoraker, G.L., Flasar, F.M., (2012). Changes in Saturn's zonal-mean tropospheric structure after the 2010 great white spot. *AAS/Division for Planetary Sciences Meeting Abstracts*, vol. 44, p. 412.11.
- Achterberg, R. K., Schinder, P.J., and Flasar, F. M. (2016). Saturn's Helium Abundance from Cassini CIRS and RSS Data. *AAS/Division for Planetary Sciences Meeting Abstracts*, vol. 48, p. 508.01.
- Acton Jr, C. H. (1996). Ancillary data services of NASA's navigation and ancillary information facility. *Planetary and Space Science*, 44(1), 65-70.
- Allen, R. J., & Sherwood, S. C. (2007). Utility of radiosonde wind data in representing climatological variations of tropospheric temperature and baroclinicity in the western tropical Pacific. *Journal of Climate*, 20(21), 5229-5243.
- Allison, M., Del Genio, A. D., & Zhou, W. (1995). Richardson number constraints for the Jupiter and outer planet wind regime. *Geophysical research letters*, 22(21), 2957-2960.
- Anderson, J. D., & Schubert, G. (2007). Saturn's gravitational field, internal rotation, and interior structure. *Science*, 317(5843), 1384-1387.
- Andrews, D. G., Leovy, C. B., & Holton, J. R. (1987). *Middle atmosphere dynamics*. Academic press.
- Antuñano, A., del Río-Gaztelurrutia, T., Sánchez-Lavega, A., & Hueso, R. (2015). Dynamics of Saturn's polar regions. *Journal of Geophysical Research: Planets*, 120(2), 155-176.
- Antuñano, A., del Río-Gaztelurrutia, T., Sánchez-Lavega, A., & Rodríguez-Aseguinolaza, J. (2018). Cloud morphology and dynamics in Saturn's northern polar region. *Icarus*, 299, 117-132.

Atkinson, D. H. (2001). The Galileo Jupiter Probe Doppler Wind Experiment. *Solar System Research*, 35(5), 354-375.

Atkinson, D. H., Ingersoll, A. P., & Seiff, A. (1997). Deep winds on Jupiter as measured by the Galileo probe. *Nature*, 388(6643), 649-650.

Atkinson, D. H., Pollack, J. B., & Seiff, A. (1996). Galileo Doppler measurements of the deep zonal winds at Jupiter. *Science*, 272(5263), 842-843.

Atkinson, D. H., Pollack, J. B., & Seiff, A. (1998). The Galileo probe Doppler wind experiment: Measurement of the deep zonal winds on Jupiter. *Journal of Geophysical Research: Planets*, 103(E10), 22911-22928.

Baines, K. H., Drossart, P., Momary, T. W., Formisano, V., Griffith, C., Bellucci, G., Bibring, J.P., Brown, R.H., Buratti, B.J., Capaccioni, F., Cerroni, P., Clark, R.N., Coradini, A., Combes, M., Cruikshank, D.P., Jaumann, R., Langevin, Y., Matson, D.L., McCord, T.B., ..., & Sotin, C. (2005). The atmospheres of Saturn and Titan in the near-infrared: First results of Cassini/VIMS. *Earth, Moon, and Planets*, 96(3-4), 119-147.

Baines, K. H., Momary, T. W., Fletcher, L. N., Showman, A. P., Roos-Serote, M., Brown, R. H., Buratti, B.J., Clark, R.N., & Nicholson, P. D. (2009). Saturn's north polar cyclone and hexagon at depth revealed by Cassini/VIMS. *Planetary and Space Science*, 57(14-15), 1671-1681.

Baines, K. H., Sromovsky, L. A., Fry, P. M., Momary, T. W., Brown, R. H., Buratti, B. J., Clark, R.N., Nicholson, P.D. & Sotin, C. (2018). The eye of Saturn's north polar vortex: unexpected cloud structures observed at high spatial resolution by Cassini/VIMS. *Geophysical Research Letters*, 45(12), 5867-5875.

Barnes, J. W., Brown, R. H., Soderblom, L., Buratti, B. J., Sotin, C., Rodriguez, S., Le Mouèlic, S, Baines, K., Clark, R. & Nicholson, P. (2007). Global-scale surface spectral variations on Titan seen from Cassini/VIMS. *Icarus*, 186(1), 242-258.

Batchelor, G. K. (1967). *An Introduction to Fluid Dynamics*. Cambridge University Press.

Beron-Vera, F. J., Brown, M. G., Olascoaga, M. J., Rypina, I. I., Kocak, H., & Udovydchenkov, I. A. (2008). Zonal jets as transport barriers in planetary atmospheres. *Journal of the atmospheric sciences*, 65(10), 3316-3326.

- Bjoraker, G. L., N. J. Chanover, D. A. Glenar, and T. Hewagama (2007), Saturn's deep cloud structure derived from 5-micron spectra, *Eos Trans. AGU*, 88(52), Fall Meet. Suppl., Abstract P31A-0184.
- Brown, R. H., Baines, K. H., Bellucci, G., Bibring, J. P., Buratti, B. J., Capaccioni, F., Coradini, A., Cruikshank, D.P., Drossart, P., Formisano, V., Jaumann, R., Langevin, Y., Matson, D.L., McCord, T.B., Mennella, V., Miller, E., Nelson, R.M., Nicholson, P.D., ..., & Sotin, C. (2004). The Cassini visual and infrared mapping spectrometer (VIMS) investigation. *Space Science Reviews*, 115(1-4), 111-168.
- Capaccioni, F., Coradini, A., Cerroni, P., & Amici, S. (1998). Imaging spectroscopy of Saturn and its satellites: VIMS-V onboard Cassini. *Planetary and space science*, 46(9-10), 1263-1276.
- Cheng, A. F., & Domingue, D. L. (2000). Radiative transfer models for light scattering from planetary surfaces. *Journal of Geophysical Research: Planets*, 105(E4), 9477-9482.
- Choi, D. S., Showman, A. P., & Brown, R. H. (2009). Cloud features and zonal wind measurements of Saturn's atmosphere as observed by Cassini/VIMS. *Journal of Geophysical Research: Planets*, 114(E4).
- Conrath, B. J., & Gautier, D. (1980). Thermal structure of Jupiter's atmosphere obtained by inversion of Voyager 1 infrared measurements. In *Remote sensing of atmospheres and oceans* (pp. 611-628).
- Conrath, B. J., Gierasch, P. J., & Ustinov, E. A. (1998). Thermal structure and para hydrogen fraction on the outer planets from Voyager IRIS measurements. *Icarus*, 135(2), 501-517.
- de Latorre Juárez, M., Fisher, B. M., & Orton, G. S. (2002). Large scale geostrophic winds with a full representation of the Coriolis force: Application to IR observations of the upper Jovian troposphere. *Geophysical & Astrophysical Fluid Dynamics*, 96(2), 87-114.
- De Verdier, A. C., & Schopp, R. (1994). Flows in a rotating spherical shell: the equatorial case. *Journal of Fluid Mechanics*, 276, 233-260.
- Del Genio, A. D., & Barbara, J. M. (2012). Constraints on Saturn's tropospheric general circulation from Cassini ISS images. *Icarus*, 219(2), 689-700.

Del Genio, A. D., Barbara, J. M., Ferrier, J., Ingersoll, A. P., West, R. A., Vasavada, A. R., Spitale, J., & Porco, C. C. (2007). Saturn eddy momentum fluxes and convection: First estimates from Cassini images. *Icarus*, 189(2), 479-492.

Desch, M. D., & Kaiser, M. L. (1981). Voyager measurement of the rotation period of Saturn's magnetic field. *Geophysical Research Letters*, 8(3), 253-256.

Dowling, T. E. (2014). Saturn's Longitude: Rise of the Second Branch of Shear-Stability Theory and Fall of the First. *International Journal of Modern Physics D*, 23(04), 1430006.

Dunford, B., Piazza, E. & Thompson, J.R., *Cassini: 1991-2017 Legacy: Science Overview*, National Aeronautical and Space Administration, Goddard Space Flight Center, <https://saturn.jpl.nasa.gov/science/overview/>.

Dyudina, U. A., Ingersoll, A. P., Ewald, S. P., Vasavada, A. R., West, R. A., Del Genio, A. D., Barbara, J.M., Porco, C.C., Achterberg, R.A., Flasar, F.M., & Simon-Miller, A. A., Fletcher, L.N. (2008). Dynamics of Saturn's south polar vortex. *Science*, 319(5871), 1801-1801.

Dyudina, U. A., Ingersoll, A. P., Ewald, S. P., Vasavada, A. R., West, R. A., Baines, K. H., Momary, T.W., Del Genio, A.D., Barbara, J.M., Porco, C.C., Achterberg, R.K., Flasar, F.M., Simon-Miller, A.A., & Fletcher, L.N. (2009). Saturn's south polar vortex compared to other large vortices in the Solar System. *Icarus*, 202(1), 240-248.

Fischer, G., Kurth, W. S., Gurnett, D. A., Zarka, P., Dyudina, U. A., Ingersoll, A. P., Ewald, S.P., Porco, C.C., Wesley, A., Go, C. & Delcroix, M. (2011). A giant thunderstorm on Saturn. *Nature*, 475(7354), 75-77.

Flasar, F. M., Achterberg, R. K., Conrath, B. J., Pearl, J. C., Bjoraker, G. L., Jennings, D. E., Romani, P.N., Simon-Miller, A.A., Kunde, V.G., Nixon, C.A., Bézard, B., Orton, G.S., Spilker, L.J., Spencer, J.R., Irwin, P.G. J., Teanby, N.A., Owen, T.C., Brasunas, J., Segura, M.E., ... & Bézard, B. (2005). Temperatures, winds, and composition in the Saturnian system. *science*, 307(5713), 1247-1251.

Flasar, F. M., Kunde, V. G., Abbas, M. M., Achterberg, R. K., Ade, P., Barucci, A., Bézard, B., Bjoraker, G.L., Brasunas, J.C., Calcutt, S., Carlson, R., Cesarsky, C.J., Conrath, B.J., Coradini, A., Courtin, R., Coustenis, A., Edberg, S, Edington, S, Ferrari, C.,..., Taylor, F.W. (2004). Exploring the Saturn system in the thermal infrared: The composite infrared spectrometer. In *The Cassini-Huygens Mission* (pp. 169-297). Springer.

Fletcher, L. N., Achterberg, R. K., Greathouse, T. K., Orton, G. S., Conrath, B. J., Simon-Miller, A. A., Teanby, N., Guerlet, S., Irwin, P.G.J., & Flasar, F. M. (2010). Seasonal change on Saturn from Cassini/CIRS observations, 2004–2009. *Icarus*, 208(1), 337-352.

Fletcher, L. N., Baines, K. H., Momary, T. W., Showman, A. P., Irwin, P. G., Orton, G. S., Roos-Serote, M., & Merlet, C. (2011). Saturn's tropospheric composition and clouds from Cassini/VIMS 4.6–5.1 μm nightside spectroscopy. *Icarus*, 214(2), 510-533.

Fletcher, L. N., Irwin, P. G., Achterberg, R. K., Orton, G. S., & Flasar, F. M. (2016). Seasonal variability of Saturn's tropospheric temperatures, winds and para-H₂ from Cassini far-IR spectroscopy. *Icarus*, 264, 137-159.

Fletcher, L. N., Irwin, P. G. J., Sinclair, J. A., Orton, G. S., Giles, R. S., Hurley, J., Gorius, N., Achterberg, R.K., Hesman, G.L., & Bjoraker, G. L. (2015). Seasonal evolution of Saturn's polar temperatures and composition. *Icarus*, 250, 131-153.

Fletcher, L. N., Irwin, P. G. J., Teanby, N. A., Orton, G. S., Parrish, P. D., de Kok, R., Howett, C, Calcutt, S.B., Bowles, N. & Taylor, F. W. (2007). Characterising Saturn's vertical temperature structure from Cassini/CIRS. *Icarus*, 189(2), 457-478.

Fouchet, T., Guerlet, S., Strobel, D. F., Simon-Miller, A. A., Bézard, B., & Flasar, F. M. (2008). An equatorial oscillation in Saturn's middle atmosphere. *Nature*, 453(7192), 200-202.

Gaddis, L., Anderson, J., Becker, K., Becker, T., Cook, D., Edwards, K., Eliason, E., Hare, T., Kieffer, H., Lee, E.M., Mathews, J., Soderblom, L, Sucharski, T., & Torson, J. (1997, March). An overview of the integrated software for imaging spectrometers (ISIS). In *Lunar and Planetary Science Conference* (Vol. 28, p. 387).

García-Melendo, E., Arregi, J., Rojas, J. F., Hueso, R., Barrado-Izagirre, N., Gómez-Forellad, J. M., Pérez-Hoyos, S., Sanz-Requena, J.F. & Sánchez-Lavega, A. (2011). Dynamics of Jupiter's equatorial region at cloud top level from Cassini and HST images. *Icarus*, 211(2), 1242-1257.

García-Melendo, E., Hueso, R., Sánchez-Lavega, A., Legarreta, J., del Río-Gaztelurrutia, T., Pérez-Hoyos, S., & Sanz-Requena, J. F. (2013). Atmospheric dynamics of Saturn's 2010 giant storm. *Nature Geoscience*, 6(7), 525-529.

García-Melendo, E., Sánchez-Lavega, A., & Hueso, R. (2007). Numerical models of Saturn's long-lived anticyclones. *Icarus*, 191(2), 665-677.

García-Melendo, E., Sánchez-Lavega, A., Legarreta, J., Perez-Hoyos, S., & Hueso, R. (2010). A strong high altitude narrow jet detected at Saturn's equator. *Geophysical research letters*, 37(22).

Gierasch, P. J. (1996). Atmospheric dynamics on the outer planets. *Science*, 273(5273), 320-321.

Godfrey, D. A. (1988). A hexagonal feature around Saturn's north pole. *Icarus*, 76(2), 335-356.

Grand Finale - Cassini Bids Farewell. (2017, September 17). Retrieved August 12, 2019 from <https://cassini-huygens.cnes.fr/en/grand-finale-les-adieux-de-cassini>.

Guerlet, S., Fouchet, T., Bézard, B., Flasar, F. M., & Simon-Miller, A. A. (2011). Evolution of the equatorial oscillation in Saturn's stratosphere between 2005 and 2010 from Cassini/CIRS limb data analysis. *Geophysical research letters*, 38(9).

Guerlet, S., Fouchet, T., Spiga, A., Flasar, F. M., Fletcher, L. N., Hesman, B. E., & Gorius, N. (2018). Equatorial oscillation and planetary wave activity in Saturn's stratosphere through the Cassini epoch. *Journal of Geophysical Research: Planets*, 123(1), 246-261.

Hall, A. (1877). On the Rotation of Saturn. *The Analyst*, 4(2), 36-42.

Helled, R., & Guillot, T. (2013). Interior models of Saturn: including the uncertainties in shape and rotation. *The Astrophysical Journal*, 767(2), 113.

Herschel, W. (1794). VIII. On the rotation of the planet Saturn upon its axis. *Philosophical Transactions of the Royal Society of London*, (84), 48-66.

Holton, J. R. (1979) *An Introduction to Dynamic Meteorology* (2nd edition), Academic Press.

Holton, J. R. (2004) *An Introduction to Dynamic Meteorology* (4th edition), Academic Press.

Holton, J. R. and Hakim, G.R. (2013) *An Introduction to Dynamic Meteorology* (5th edition), Academic Press.

Hubbard, W.B., Buratti, B., and Marley, M, (2020), Saturn, Encyclopædia Britannica. Retrieved from <https://www.britannica.com/place/Saturn-planet>

Hueso, R., & Sánchez-Lavega, A. (2004). A three-dimensional model of moist convection for the giant planets II: Saturn's water and ammonia moist convective storms. *Icarus*, 172(1), 255-271.

Ingersoll, A. P. (1990). Atmospheric dynamics of the outer planets. *Science*, 248(4953), 308-315.

Ingersoll, A. P., Beebe, R. F. Conrath, B. J., and Hunt, G. E. (1984) *Structure and dynamics of Saturn's atmosphere*, University of Arizona Press.

Irwin, P. G. J., Parrish, P., Fouchet, T., Calcutt, S. B., Taylor, F. W., Simon-Miller, A. A., & Nixon, C. A. (2004). Retrievals of jovian tropospheric phosphine from Cassini/CIRS. *Icarus*, 172(1), 37-49.

Jukes, M. N., & McIntyre, M. E. (1987). A high-resolution one-layer model of breaking planetary waves in the stratosphere. *Nature*, 328(6131), 590-596.

Kaiser, M. L., Desch, M. D., Warwick, J. W., & Pearce, J. B. (1980). Voyager detection of nonthermal radio emission from Saturn. *Science*, 209(4462), 1238-1240.

Kalnay, E., Kanamitsu, M., Kistler, R., Collins, W., Deaven, D., Gandin, L., Iredell, M., Saha, S., White, G., Woollen, J., Zhu, Y., Chelliah, M., Ebisuzaki, W., Higgins, W., Janowiak, J., Mo, K.C., Ropelewski, C., Wang, J., Leetmaa, A, ..., Joseph, D. (1996). The NCEP/NCAR 40-year reanalysis project. *Bulletin of the American meteorological Society*, 77(3), 437-472.

Kanamitsu, M., Ebisuzaki, W., Woollen, J., Yang, S. K., Hnilo, J. J., Fiorino, M., & Potter, G. L. (2002). NCEP–DOE AMIP-II Reanalysis (R-2). *Bulletin of the American Meteorological Society*, 83(11), 1631-1644.

Li, C., & Ingersoll, A. P. (2015). Moist convection in hydrogen atmospheres and the frequency of Saturn's giant storms. *Nature Geoscience*, 8(5), 398-403.

Li, L., Gierasch, P. J., Achterberg, R. K., Conrath, B. J., Flasar, F. M., Vasavada, A. R., Ingersoll, A.P., Banfield, D., Simon-Miller, A.A., & Fletcher, L. N. (2008). Strong jet and a new thermal wave in Saturn's equatorial stratosphere. *Geophysical research letters*, 35(23).

Li, L., Ingersoll, A. P., Vasavada, A. R., Porco, C. C., Del Genio, A. D., & Ewald, S. P. (2004). Life cycles of spots on Jupiter from Cassini images. *Icarus*, 172(1), 9-23.

Li, L., Ingersoll, A. P., Vasavada, A. R., Simon-Miller, A. A., Del Genio, A. D., Ewald, S. P., Porco, C.C., & West, R. A. (2006). Vertical wind shear on Jupiter from Cassini images. *Journal of Geophysical Research: Planets*, 111(E4).

Li, L., Jiang, X., Ingersoll, A. P., Del Genio, A. D., Porco, C. C., West, R. A., Vasavada, A.R., Ewald, S.P., Conrath, B.J., Gierasch, P.J., Simon-Miller, A. A., Nixon, C.A., Achterberg, R.K., Orton, G.S., Fletcher, L.N., & Baines, K.H. (2011). Equatorial winds on Saturn and the stratospheric oscillation. *Nature Geoscience*, 4(11), 750-752.

Li, L., Studwell, A., Jiang, X., Kao, A., Baines, K. H., Momary, T., Fry, P.M., Ingersoll, A.P., Janssen, M.A., Sánchez-Lavega, A., Achterberg, R. K., Flasar, F. M., Simon, A.A, Dyudina, U. A. & West, R. (2016). Spatiotemporal Variability of Saturn's Zonal Winds from Cassini Multi-Instrument Observations. AGUFM, P31D-05.

Limaye, S. S. (1986). Jupiter: New estimates of mean zonal flow at the cloud level. *Icarus*. 6(5). 335-352.

McCord, T. B., Coradini, A., Hibbitts, C. A., Capaccioni, F., Hansen, G. B., Filacchione, G., Clark, R.N., Cerroni, P., Brown, R.H., Baines, K.H., Bellucci, G., Bibring, J.-P., Buratti, B.J., Bussoletti, E., Combes, M., Cruikshank, D.P., Drossant, P., Formisano, V, Jaumann, ..., Sotin, C. (2004). Cassini VIMS observations of the Galilean satellites including the VIMS calibration procedure. *Icarus*, 172(1), 104-126.

McIntyre, M. E. (2014). *Potential Vorticity*. In *Encyclopedia of Atmospheric Science* (2nd edition) (G. North, J. Pyle, and F. Zhang, Eds.), Academic Press.

McKim, R. J. (2011). Great White Spots on Saturn: current and historical observations. *Journal of the British Astronomical Association*, 121, 270-273.

Marcus, P. S., Tollefson, J., Wong, M. H., & de Pater, I. (2019). An equatorial thermal wind equation: Applications to Jupiter. *Icarus*, 324, 198-223.

Merlet, C. (2012, March 8). *Clouds and Haze in Saturn's Troposphere*. Department of Physics, University of Oxford,
https://www2.physics.ox.ac.uk/sites/default/files/2012-03-08/2_merlet_pdf_17256.pdf

Minnaert, M. (1941). The reciprocity principle in lunar photometry. *The Astrophysical Journal*, 93, 403-410.

Mishchenko, M. I. (1993). On the nature of the polarization opposition effect exhibited by Saturn's rings. *The Astrophysical Journal*, 411, 351-361.

Momary, T. W., & Baines, K. H. (2006). The zoology of Saturn: The bizarre features unveiled by the 5 micron eyes of Cassini/VIMS. In *Bulletin of the American Astronomical Society* (Vol. 38, p. 499).

Our Astronomical Column. *Nature* 102, 233 (1918).

Pedlosky, J. (1987). *Geophysical Fluid Dynamics*. Springer-Verlag Press.

Phillips, N. A. (1963). Geostrophic motion. *Reviews of Geophysics*, 1(2), 123-176.

Polvani, L. M., Waugh, D. W., & Plumb, R. A. (1995). On the subtropical edge of the stratospheric surf zone. *Journal of the atmospheric sciences*, 52(9), 1288-1309.

Porco, C. C., West, R. A., Squyres, S., McEwen, A., Thomas, P., Murray, C. D., Del Genio, A., Ingersoll, A.P., Johnson, T.V., Neukum, G., Veverka, J., Dones, L., Brahic, A., Burns, J.A., Haemmerle, V., Knowles, B., Dawson, D, Roatsch, T., Beurle, K. & Owen, W. (2004). Cassini imaging science: Instrument characteristics and anticipated scientific investigations at Saturn. In *The Cassini-Huygens Mission* (pp. 363-497). Springer.

Porco, C. C., Baker, E., Barbara, J., Beurle, K., Brahic, A., Burns, J. A., Charnoz, S., Cooper, N., Dawson, D.D., Del Genio, A.D., Denk, T., Dones, L., Dyudina, U., Evans, M.W., Giese, B., Grazier, K., Helfenstein, P., Ingersoll, A.P., Jacobson, R.A., ... & West, R. (2005). Cassini imaging science: Initial results on Saturn's atmosphere. *Science*, 307(5713), 1243-1247.

Read, P. L., Conrath, B. J., Fletcher, L. N., Gierasch, P. J., Simon-Miller, A. A., & Zuchowski, L. C. (2009). Mapping potential vorticity dynamics on Saturn: Zonal mean circulation from Cassini and Voyager data. *Planetary and Space Science*, 57(14-15), 1682-1698.

Read, P. L., Dowling, T. E., & Schubert, G. (2009). Saturn's rotation period from its atmospheric planetary-wave configuration. *Nature*, 460(7255), 608-610.

Salby, M. L. (1996). *Fundamentals of atmospheric physics*. Elsevier.

Salyk, C., Ingersoll, A. P., Lorre, J., Vasavada, A., & Del Genio, A. D. (2006). Interaction between eddies and mean flow in Jupiter's atmosphere: Analysis of Cassini imaging data. *Icarus*, 185(2), 430-442.

Sánchez-Lavega, A. (1994). Saturn's great white spots. *Chaos: An Interdisciplinary Journal of Nonlinear Science*, 4(2), 341-353.

Sánchez-Lavega, A., del Río-Gaztelurrutia, T., Delcroix, M., Legarreta, J. J., Gómez-Forrellad, J. M., Hueso, R., García-Melendo, E., Pérez-Hoyos, S., Barrado-Navascués, D., Lillo, J., & The International Outer Planet Watch (IOPW) Team. (2012). Ground-based observations of the long-term evolution and death of Saturn's 2010 Great White Spot. *Icarus*, 220(2), 561-576.

Sánchez-Lavega, A., del Río-Gaztelurrutia, T., Hueso, R., Gómez-Forrellad, J. M., Sanz-Requena, J. F., Legarreta, J., García-Melendo, E., Colas, F., Lecacheux, J., Fletcher, L.N., Barrado-Navascués, D., Parker, D., & The International Outer Planet Watch (IOPW) Team. (2011). Deep winds beneath Saturn's upper clouds from a seasonal long-lived planetary-scale storm. *Nature*, 475(7354), 71-74.

Sánchez-Lavega, A., Hueso, R., & Pérez-Hoyos, S. (2007). The three-dimensional structure of Saturn's equatorial jet at cloud level. *Icarus*, 187(2), 510-519.

Sánchez-Lavega, A., del Río-Gaztelurrutia, T., Hueso, R., Pérez-Hoyos, S., García-Melendo, E., Antuñano, A., Mendikoa, I., Rojas, J.F., Lillo, J., Barrado-Navascués, D., Gomez-Forrellad, J.M., Go, C., Peach, D., Barry, T., Milika, D.P., Nicholas, P., & Wesley, A. (2014). The long-term steady motion of Saturn's hexagon and the stability of its enclosed jet stream under seasonal changes. *Geophysical Research Letters*, 41(5), 1425-1431.

Sánchez-Lavega, A., García-Melendo, E., Pérez-Hoyos, S., Hueso, R., Wong, M.H., Simon, A., Sanz-Requena, J.F., Antuñano, A., Barrado-Izagirre, N., Garate-Lopez, I., Rojas, J.F., del Río-Gaztelurrutia, T., Gomez-Forrellad, J.M., de Pater, I., Li, L., & Barry, T. (2016). An enduring rapidly moving storm as a guide to Saturn's Equatorial jet's complex structure. *Nature communications*, 7(1), 1-10.

Sánchez-Lavega, A., Hueso, R., Pérez-Hoyos, S., Rojas, J. F., & French, R. G. (2004). Saturn's cloud morphology and zonal winds before the Cassini encounter. *Icarus*, 170(2), 519-523.

Sánchez-Lavega, A., Lecacheux, J., Colas, F., Rojas, J. F., & Gomez, J. M. (1999). Discrete cloud activity in Saturn's equator during 1995, 1996 and 1997. *Planetary and space science*, 47(10-11), 1277-1283.

Sánchez-Lavega, A., Pérez-Hoyos, S., Rojas, J. F., Hueso, R., & French, R. G. (2003). A strong decrease in Saturn's equatorial jet at cloud level. *Nature*, 423(6940), 623-625.

Sanz-Requena, J. F., Pérez-Hoyos, S., Sánchez-Lavega, A., Antuñano, A., & Irwin, P. G. (2018). Haze and cloud structure of Saturn's north pole and hexagon wave from Cassini/ISS imaging. *Icarus*, 305, 284-300.

Sayanagi, K. M., Blalock, J. J., Dyudina, U. A., Ewald, S. P., & Ingersoll, A. P. (2017). Cassini ISS observation of Saturn's north polar vortex and comparison to the south polar vortex. *Icarus*, 285, 68-82.

Sayanagi, K. M., Dyudina, U. A., Ewald, S. P., Fischer, G., Ingersoll, A. P., Kurth, W. S., Muro, G.D., Porco, C.C., & West, R. A. (2013). Dynamics of Saturn's great storm of 2010-2011 from Cassini ISS and RPWS. *Icarus*, 223(1), 460-478.

Scientific Notes and News (1933). *Journal of the Washington Academy of Sciences*, 23(9), 446-448.

Simon, A. A., Li, L., & Reuter, D. C. (2015). Small-scale waves on Jupiter: A reanalysis of New Horizons, Voyager, and Galileo data. *Geophysical Research Letters*, 42(8), 2612-2618.

Simon-Miller, A. A., Conrath, B. J., Gierasch, P. J., Orton, G. S., Achterberg, R. K., Flasar, F. M., & Fisher, B. M. (2006). Jupiter's atmospheric temperatures: From Voyager IRIS to Cassini CIRS. *Icarus*, 180(1), 98-112.

Smith, B. A., Soderblom, L., Beebe, R., Boyce, J., Briggs, G., Bunker, A., Collins, S.A., Hansen, C.J., Johnson, Johnson, T.V., Mitchell, J.L., Terrile, R.J., Carr, M., Cook II, A.F., Cuzzi, J., Pollack, J.B., Danielson, G.E., Ingersoll, A., Davies, M.E., Hunt, G.E., ..., & Suomi, V.E., (1981). Encounter with Saturn: Voyager 1 imaging science results. *Science*, 212(4491), 163-191.

Sromovsky, L. A., Baines, K. H., & Fry, P. M. (2018). Models of bright storm clouds and related dark ovals in Saturn's Storm Alley as constrained by 2008 Cassini/VIMS spectra. *Icarus*, 302, 360-385.

Studwell, A., Li, L., Jiang, X., Baines, K. H., Fry, P. M., Momary, T. W., & Dyudina, U. A. (2018). Saturn's Global Zonal Winds Explored by Cassini/VIMS 5- μ m Images. *Geophysical research letters*, 45(14), 6823-6831.

Vasavada, A. R., Hörst, S. M., Kennedy, M. R., Ingersoll, A. P., Porco, C. C., Del Genio, A. D., & West, R. A. (2006). Cassini imaging of Saturn: Southern hemisphere winds and vortices. *Journal of Geophysical Research: Planets*, 111(E5).

Vernon, E. M., & Ashburn, E. V. (1938). a Practical Method for Computing Winds Aloft from Pressure and Temperature Fields. *Monthly Weather Review*, 66(9), 267-274.

Williams, David (2015, October 13). "Saturnian Rings Fact Sheet", National Aeronautical and Space Administration, Goddard Space Flight Center, <https://nssdc.gsfc.nasa.gov/planetary/factsheet/satringfact.html>.